Design of Hybrid Composite Coexisted Multilayer and Nano Structure

(積層構造とナノ構造が共存するハイブリッド複合材料の設計)

2003

Tomohiko ADACHI

Department of Materials Chemistry
Faculty of Engineering
Osaka University

Preface

The studies presented in this thesis were carried out under the guidance of Professor Koichi Niihara at Department of Materials Chemistry of Faculty of Engineering at Osaka University during 1998-2003.

The objective in this thesis is to design novel composite materials, in which multilayer and nano structure are coexisting, as named hybrid composite, and then to fabricate and investigate the various properties. From the investigation of the hybrid composites, the potential of the design concept was revealed via this study.

The author hopes that the concepts and finding obtained in this study will contribute to the application for the progress and development in many fields of science and engineering.

Tomohiko ADACHI

Department of Materials Chemistry
Faculty of Engineering
Osaka University
2-1, Yamada-oka, Suita, Osaka 565-0871
Japan

December 2002

Design of Hybrid Composite Coexisted Multilayer and Nano Structure

Contents

1. Introduction 01

1-1. Ceramic-based Composites 01
1-2. Microcomposites 01
1-3. Multilayered Composites 02
1-4. Nanocomposites 03
1-4-1. Structure 03
1-4-2. Mechanisms of Reinforcement 04
1-5. Hybrid Composites 05
1-6. Objectives 06

2. Design of Hybrid Composites 10

2-1. Introduction 10
2-2. Al_2O_3/3Y-TZP Multilayered Composites 11
2-2-1. Directional Residual Stress 11
2-2-2. Mechanisms of Reinforcement 12
(1) Improvement of Apparent Strength
(2) Depression of Crack Propagation
(3) Crack Deflection
2-2-3. Control of Residual Stress 14
2-3. Multilayered Nanocomposites 15
2-3-1. Design Concepts 15
(1) Effects of Nano-particles
(2) Effects of Control of Residual Stress
2-3-2. Structure 16

2-4. 2-dimensional Dispersed Nanocomposites 18
2-4-1. Design Concepts 18
(1) Induction of Residual Stress
(2) Bonding of Layers
(3) Control of Residual Stress
2-4-2. Structure 19
2-5. Summary 20

3. Fabrication and Evaluation of Hybrid Composites . . . 22

3-1. Introduction 22
3-2. Fabrication of Hybrid Composites 23
3-3. Evaluation of Hybrid Composites 28
3-3-1. Density 28
3-3-2. Identification of Crystalline Phase 29
3-3-3. Microstructural Observation 29
3-3-4. Residual Stress Measurement 29
3-3-5. Mechanical Properties 30
3-3-6. Thermal Properties 30
3-4. Summary 31

4. Al_2O_3/3Y-TZP Multilayered Composites 33

4-1. Introduction 33
4-2. Experimental Procedure 33
4-3. Microstructure 34
4-4. Calculation of Macroscopic Residual Stress 36
4-5. Mechanism of Channel Crack Formation 37
4-5-1. Effect of Average Tensile Stress (A1Z1, A2Z1, and A3Z1) . . 37
4-5-2. Effect of Stress Distribution (A1Z1, A2Z2, A4Z4, and A8Z8) . 38
4-5-3. Effect of Stress Difference (Debonding in A1Z3) 40
4-6. Summary 40

5. Al_2O_3/3Y-TZP Multilayered Nanocomposites 42

5-1. Introduction 42
5-2. Experimental Procedure 42
5-3. Microstructure 43
5-3-1. Identification of Crystalline Phase 43
5-3-2. Microstructural Observation 43
5-3-3. Layer Thickness and Density 46
5-4. Macroscopic Residual Stress 47
5-4-1. Calculation of Macroscopic Residual Stress 47
5-4-2. Measurement of Macroscopic Residual Stress 49
5-5. Crack Propagation Behavior 54
5-5-1. Mechanism of Crack Deflection 54
5-5-2. Crack Propagation Behavior 56
5-5-3. Fracture Surface 58
5-6. Microscopic Stress Distribution 59
5-6-1. Evaluated Composites 59
5-6-2. Measurement of Microscopic Stress Distribution 60
5-6-3. Microscopic Stress Distribution 61
5-7. Summary 64

6. 2-dimensional Dispersed Nanocomposites 66

6-1. Introduction 66
6-2. Experimental Procedure 66
6-3. Microstructure 68
6-3-1. Microstructural Observation 68
6-3-2. Thickness Ratio 69
6-3-3. Density 69
6-4. Surface Stress 70
6-4-1. Surface Stress Measurement 70
6-4-2. Calculation of Residual Stress 73
(1) Residual Stress due to Multilayered Structure

(2) Residual Stress due to Particle Dispersion

(3) Total Residual Stress (Multilayer & Dispersion)

6-4-3. Stress Analysis 77

(1) Machining Stress

(2) Optimization of Measurement and Calculation

6-5. Surface Reinforcement 79

6-5-1. Hardness 79

6-5-2. IF Toughness 81

6-6. Thermal Properties 84

6-7. Summary 86

7. Summary and Conclusions 89

List of Publications 92

Acknowledgement 95

CHAPTER 1

Introduction

1-1. Ceramic-based Composites

Ceramic materials are used in many engineering fields due to their superior mechanical properties, thermal properties, electric properties and so on. However, monolithic ceramic materials are usually brittle as compared with metallic and polymeric materials. Thus, ceramic materials are recognized as low reliability materials, and themn the applications are limited mainly by this disadvantage. In order to improve the brittleness and low reliability, various methods have been developed by efforts of many predecessors. Composite concept in ceramic materials is known as a suitable method to improve this disadvantage. The ceramic-based composites, which consisted of ceramic matrix and second phase, can be classified into two types depending on a scale of size of the second phase: microcomposites and nanocomposites.

1-2. Microcomposites

When the scale of the second phase is micrometer-order, the composite materials are classified as a microcomposites. The microcomposites have a typical microstructure, in which micro-sized second phase such as particulate, platelet, whisker and fiber are dispersed at the grain boundaries of the matrix. The improvement in fracture toughness by bridging, pulling-out and crack deflection toughening mechanisms is expected in the microcomposites case. However, strength and high temperature properties are sometimes degradated while toughness has been increased.

1-3. Multilayered Composites

Multilayered composites are classified as one of the microcomposites, although the microstructure is significantly different from the second-phase dispersed microcomposite. The microstructure of multilayered composite is comprised by stacking of different layer materials.

Multilayered composites are also classified into two categories. One is the Soft/Hard system, which consisted of hard material (i.e., structural ceramics with high strength) and soft material (i.e., inorganic material involving ceramics: graphite, porous ceramics, and so on) [1-8]. The other system is Hard/Hard system, which consisted of pure structural ceramics [9-21].

In Fig. 1-1, schematic drawings of the structure and typical crack path are illustrated for both multilayered composites. Soft/Hard system is investigated for many system as SiC/C [1,2], Si_3N_4/porous-Si_3N_4 [3-5], and so on [6-8]. In this system, the cracks are propagated in the soft layer, as shown in Fig. 1-1(a). Therefore, the fracture toughness is significantly increased due to the increase of fracture energy. However, the strength is significantly decreased due to the soft layer with much lower fracture strength.

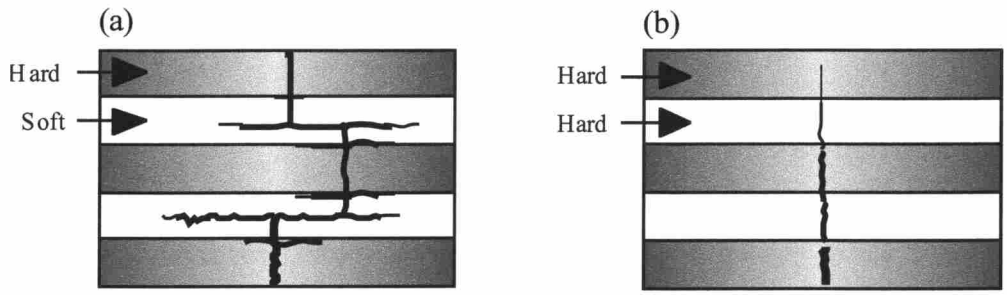

Fig. 1-1 Schematic drawings of two types of multilayered comosites: (a) Hard/Soft type and (b) Hard/Hard type.

On the other hand, Hard/Hard system is examined for Al_2O_3/ZrO_2 [9-19], Al_2O_3/Al_2TiO_5 [20], Si_3N_4/SiC [21] and et cetera. Because this system is consisted of layer materials with high fracture strength, the fracture strength of this type of multilayered composites indicates high strength. However, the fracture toughness of this system is not so much improved like the

toughness of Soft/Hard system, because cracks propagate in straight as shown in Fig. 1-1(b). Mechanism of improvement of mechanical properties in Hard/Hard system is caused by residual stress within the composites. This fact indicates that the toughness can be improved by the residual stress control. The details of the mechanisms will be discussed in Chapter 2.

1-4. Nanocomposites

1-4-1. Structure

Nanocomposites materials are defined as composites which contain second phase dispersoid of nano-meter scale [22]. The concept of ceramic nanocomposites was proposed in 1991 by Niihara [23]. According to the Niihara's concept, the particle-reinforced nanoceramics, in which nano-sized particles were dispersed within matrix grain and /or at the grain boundaries, were categorized into four types: intra-granular, inter-granular, intra/inter-granular, and nano/nano composites (see Fig. 1-2). In the intra- and inter-granular nanocomposites, the nano-sized particles are dispersed mainly within the matrix grains or at the grain boundaries of the matrix, respectively. These nanocomposites possess superior mechanical properties in hardness, fracture strength and toughness as well as reliability at room temperature [23-26]. Moreover, their high-temperature mechanical properties (i.e., hardness, strength, creep resistance, and fatigue fracture resistances) were also improved strongly. The intergranular nano-dispersoids play an important role in the grain boundary structure-control of oxide and non-oxide ceramics, in which results are in the improvement of high-temperature mechanical properties. The nano/nano composites are composed of the dispersoids and matrix grains with the nanometer-size.

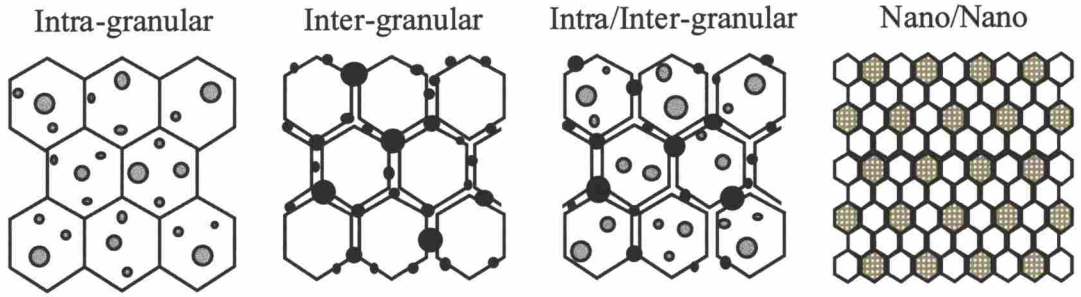

Fig. 1-2 Schematic illustrations of typical nanocomposites.

It is believed that the concept of nanocomposites are applicable to various ceramic systems. Several kinds of ceramic based nanocomposites have been studied, e.g., ceramic/ceramic [27-31], ceramic/metal [22-35], intermetallic/ceramic [36], and polymer/ceramic [37] systems.

One notable system of nanocomposites is Al_2O_3/SiC nanocomposite because of the distinguishably improved the mechanical properties. It has been reported by Niihara and coworkers that the dispersion of 5 vol% SiC nano-particles into Al_2O_3 could remarkably increase the room temperature strength from 350 MPa to over 1.0 GPa [29-32]. In addition to this high fracture strength, the fracture toughness and creep resistance were also improved by the in-grain toughening associated with the intragranular SiC particles and the grain boundary strengthening by the intergranular SiC dispersion, respectively [33-35].

1-4-2. Mechanisms of Reinforcement

It was found that the nanocomposites structure would result in the in-grain toughening, which results in better R-curve behavior. The reliability increase of ceramic components is caused by higher crack-growth resistance during crack start to propagate. In nanocomposite materials, the improvement of the mechanical properties is associated with the specific structure. Figure 1-3 indicates the schematic microstructure drawings of monolithic material and nanocomposite materials. The grain size of the nanocomposite material is smaller than that of the monolithic material, because of the dispersoids which inhibit the grain-growth involving an abnormal grain-growth. The finer microstructure of nanocomposite material brings the decrease of the size of the defect, which acts as the origin of fracture and causes decrease of the strength. Therefore, the strength of nanocomposite materials is significantly improved by the finer grain size. In addition, the grain-growth of the matrix of nanocomposite material can be effectively controlled in a small quantity of nano-sized despersion such as 5 vol% [24]. Moreover, the dispersoid within the matrix which causes the crack deflection and repression when the crack propagates. These effects bring the improvement of fracture toughness of nanocomposite materials. Intragranular fracture, which is oftenly observed in nanocomposites, is resulted from the crack propagation into the inside of grains. On the other hand, monolithic materials have a fracture mode of intergranular fracture (i.e., cracks propagate through the grain boundaries). Thus, fracture strength of the nanocomposite materials are strongly improved due to the intragranular fracture, because the strength of the in-grains is normally higher than the grain boundary.

These improvements of the mechanical properties of nanocomposite materials are caused by the nano-sized dispersoids.

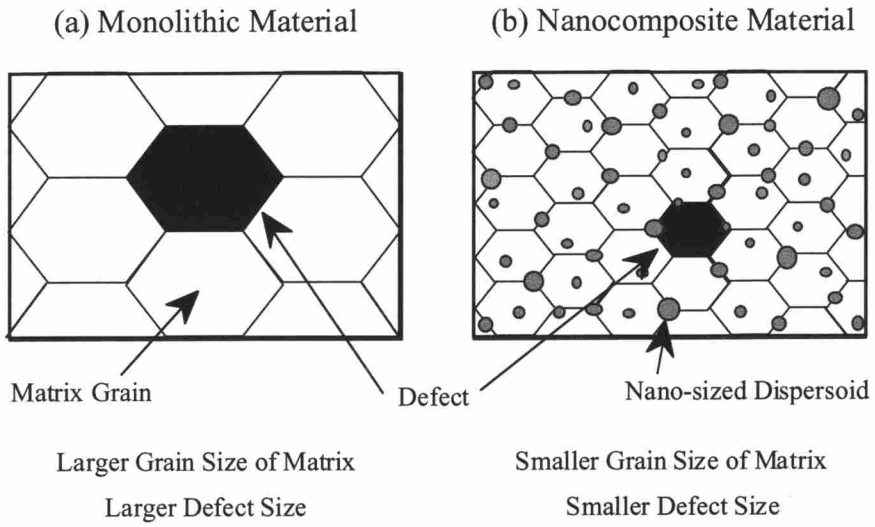

Fig. 1-3 Schematic drawings of (a) monolithic material and (b) nanocomposite material. The size of the grains of nanocomposite is smaller than that of monolith. Thus, the defect size of nanocomposite is smaller than that of monolith. This fact indicates that nanocomposite has higher fracture strength.

1-5. Hybrid Composites

To obtain a compatibility of the fracture toughness and strength, hybrid composites were designed by the combination of the microcomposite and nanocomposites.

The mechanisms of improvement of the mechanical properties for multilayered composites and nanocomposites are originated from residual stress and nano-sized dispersoid, respectively. Therefore, by the combination of multilayered composite and nanocomposite, it was expected that both mechanisms coexist in one composite. Then, hybrid composites combined both multilayer and nano structure were designed in this study.

Two kinds of hybrid composites were designed in order to improve mechanical properties by residual stress and nano-sized dispersion. In Fig. 1-4, the schematic drawings of two types of the hybrid composites are illustrated.

Multilayered nanocomposite, in which nano-sized particles were dispersed into each

layer, was designed as shown in Fig. 1-4(a). In this composite, each layer material was strengthened by nano-sized dispersion. In addition, direct control of residual stress within the multilayered nanocomposite was tried by dispersion of the nano-particles with different characteristic values.

The other hybrid composite is 2-dimensional dispersed nanocomposite (see Fig. 1-4(b)). In order to introduce directional residual stresses like a popular multilayered composites, multilayered structure was constructed by 2-dimensional dispersion of nano-sized particles. In other word, this hybrid composite is comprised of nanocomposite and monolithic layers.

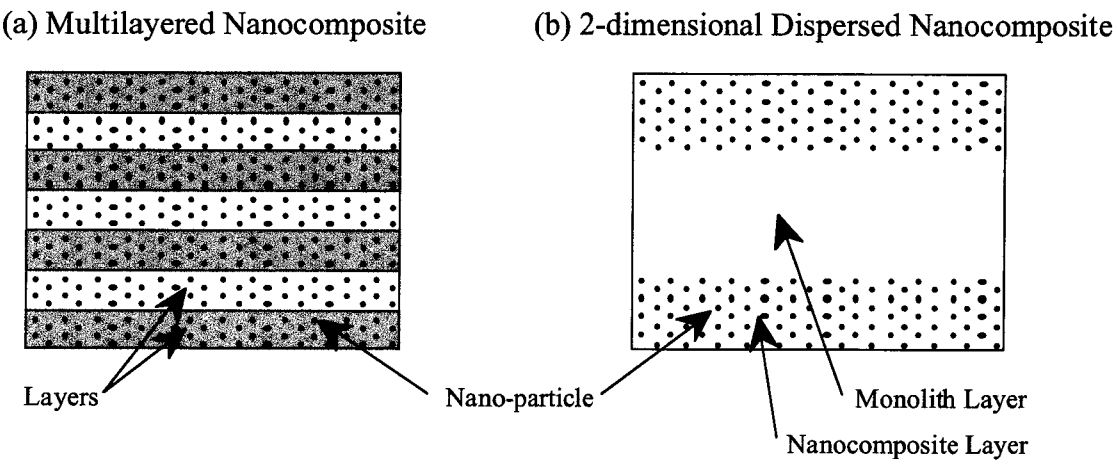

Fig. 1-4 Schematic illustrations of two types of hybrid composites. (a) Multilayered composite, in which nano-sized particles are dispersed into each layer. (b) 2-dimensional dispersed nanocomposite, in which nano-sized particles are dispersed in the surface or inside of the matrix.

1-6. Objectives

The main objective of the present thesis is to design, fabricate and evaluate the hybrid composites, in which multilayer and nano structure coexist. As mentioned above, it is inferred that the hybrid composites have superior mechanical properties as compared with traditional multilayered composites and nanocomposites. Because the hybrid composites have both multilayer and nano structure, various investigations are necessary to evaluate the both effects of multilayer and nano structure. Then, in this study, the effects of each structure in

the hybrid composites were evaluated by measurement of mechanical properties and residual stress.

This thesis consists of seven chapters.

Chapter 1 - The feature of multilayered composites and nanocomposite is reviewed, and the design concept of hybrid composites is described as the objective of this study.

Chapter 2 - Two kinds of hybrid composite (i.e., multilayered nanocomposite and 2-dimensional dispersed nanocomposite) are defined and designed in order to achieve the improvement of mechanical properties.

Chapter 3 - Fabrication and evaluation methods of the hybrid composites are described.

Chapter 4 - To control the residual stress within multilayered composites, Al_2O_3/3Y-TZP multilayered composites with various layer thickness are fabricated. Then, relationship between the residual stress and channel crack formation is investigated, and the mechanisms of the formation are revealed.

Chapter 5 - Al_2O_3/3Y-TZP multilayered nanocomposites, in which nano-sized SiC dispersed, are designed and fabricated. Residual stress measurement and evaluations of mechanical properties is carried out.

Chapter 6 - 3Y-TZP/SiC 2-dimensional dispersed nanocomposites, in which nano-sized SiC dispersed, is designed and fabricated. The mechanical properties and the thermal properties are investigated in order to confirm the effect of induced residual stress.

Finally, in Chapter 7 summary of the thesis is given.

References

[1] W.J. Clegg, K. Kendall, N.M. Alford, T.W. Button, and J.D. Birchall, *Nature*, **347**, 455 (1990).

[2] W.J. Clegg, *Acta. Metall. Mater.*, **40**, 3085 (1992).

[3] Y. Shigegaki, M.E. Brito, K. Hirao, M. Toriyama, and S. Kanzaki, *J. Am. Ceram. Soc.*, **79**, 2197 (1996).

[4] Y. Shigegaki, M.E. Brito, K. Hirao, M. Toriyama, and S. Kanzaki, *J. Ceram. Soc. Jpn.*, **105**, 824 (1997).

[5] T. Ohji, Y. Shigegaki, T. Miyajima, and S. Kanzaki, *J. Am. Ceram. Soc.*, **80**, 991 (1997).

[6] H. Liu, and S.M. Hsu, *J. Am. Ceram. Soc.*, **79**, 2452 (1996).

[7] P.E.D. Morgan, and D.B. Marshall, *J. Am. Ceram. Soc.*, **78**, 1553 (1995).

[8] H. Katsuki, and Y. Hirata, *J. Ceram. Soc. Jpn.*, **98**, 1114 (1990).

[9] D.B. Marshall, *"Layered Materials for Stuctural Applications"* Edited by J.J. Lewandowski, C.H. Ward, M.R. Jackson, and W.H. Hunt Jr., pp.195-203, Materials Research Society, 1996.

[10] T. Cartier, D. Merle, and J.L. Besson, *J. Eur. Ceram. Soc.*, **15**, 101 (1995).

[11] E. Lucchini, and O. Sbaizero, *J. Eur. Ceram. Soc.*, **15**, 975 (1995).

[12] P. Sarkar, X. Haung, and P.S. Nicholson, *J. Am. Ceram. Soc.*, **75**, 2907 (1992).

[13] J. Requena, R. Moreno, and J.S. Moya, *J. Am. Ceram. Soc.*, **72**, 2511 (1989).

[14] M. Jimenez-Melendo, F. Gutierrez-Mora, and A. Dominguez-Rodriguez, *Acta mater.*, **48**, 4715 (2000).

[15] D.R. Mumm, D.B. Marshall, A. Griffin, C.W. Griffin, and C.S. Turner, *J. Am. Ceram. Soc.*, **79**, 1416 (1996).

[16] D.B. Marshall, J.J. Ratto, and F.F. Lange, *J. Am. Ceram. Soc.*, **74**, 2979 (1991).

[17] M.P. Rao, and F.F. Lange, *J. Am. Ceram. Soc.*, **85**, 1222 (2002).

[18] M. Oechsner, C. Hillman, and F.F. Lange, *J. Am. Ceram. Soc.*, **79**, 1834 (1996).

[19] V. Sergo, D.M. Lipkin, G.D. Portu, and D.R. Clarke, *J. Am. Ceram. Soc.*, **80**, 1633 (1997).

[20] C.J. Russo, M.P. Harmer, H.M. Chan, and G.A. Miller, *J. Am. Ceram. Soc.*, **75**, 3396 (1992).

[21] P. Sajgalik, Z. Lences, and J. Dusza, *J. Mater. Sci.*, **31**, 4837 (1996).

[22] R. Roy, R.A. Roy, and D.M. Roy, *Mater. Lett.*, **4**, 323 (1986).

[23] K. Niihara, *J. Ceram. Soc. Jpn.*, **99**, 974 (1991).

[24] T. Ohji, Y.K. Jeong, Y.H. Choa, and K. Niihara, *J. Am. Ceram. Soc.*, **81**, 1453 (1998).

[25] T. Ohji, T. Kusunose, and K. Niihara, *J. Am. Ceram. Soc.*, **81**, 2713 (1998).

[26] N. Bamba, Y.H. Choa, T. Sekino, and K. Niihara, *J. Eur. Ceram. Soc.*, in press.

[27] K. Niihara, A. Nakahira, T. Uchiyama, and T. Hirano, in Fracture Mechanics of Ceramics, 7, Edited by R.C. Bradt, A.G. Evans, D.P.H. Hasselman, and F.F. Lange, pp.103-116, Plenum Press, 1986.

[28] A. Nakahira, and K. Niihara, in Fracture Mechanics of Ceramics, 7, Editied by M. Sasaki, R.C. Bradt, D.P.H. Hasselman, and D. Munz, pp. 165-178, Plenum Press, 1992.

[29] T. Ohji, A. Nakahira, T. Hirano, and K. Niihara, *J. Am. Ceram. Soc.*, **77**, 3259 (1994).

[30] E. Yasuda, Q. Bao, and K. Niihara, *J. Ceram. Soc. Jpn.*, **100**, 514 (1992).

[31] G. Sasaki, H. Nakase, K. Suganuma, T. Fujita, and K. Niihara, *J. Ceram. Soc. Jpn.*, **100**, 536 (1992).

[32] T. Sekino, A. Nakahira, M. Nawa, and K. Niihara, *J. Jpn. Soc. Powder Powder Metall.* **38**, 326 (1991).

[33] M. Nawa, T. Sekino, and K. Niihara, *J. Mater. Sci.*, **29**, 3185 (1995).

[34] T. Sekino, and K. Niihara, *Nanostruct. Mater.*, **6**, 663 (1995).

[35] M. Nawa, K. Yamazaki, T. Sekino, and K. Niihara, *J. Mater. Sci.*, **31**, 2848 (1997).

[36] A. Nakahira, H. Tamada, and K. Niihara, *J. Jpn. Powder Powder Metall.*, **41**, 514 (1994).

[37] K. Niihara, Y.H. Choa, M. Hussain, Y. Hamahashi, H. Kawahara, Y. Okamoto, and H. Nishida, *Materials Integration*, **12** (5), 47 (1999).

CHAPTER 2

Design of Hybrid Composites

2-1. Introduction

Ceramic-based materials are brittle. This fact limits their use in numerous systems even though they have many superior mechanical properties including high strength, hardness, thermostability, and so on. Hence, improvements of toughness of ceramic materials are necessary to widen the application fields of ceramic materials. In general, catastrophic fracture of ceramic materials is caused by the microcrack formed near the surface of the material. Therefore, it is believed that surface reinforcement by several techniques must be very effective in order to prevent the fracture of ceramic materials.

It is known that ceramic-based multilayered composites can improve fracture strength and toughness due to the residual stress within the composite. The residual stress has directivity; compressive and tensile stresses are produced in the layers depending on the mismatch of coefficient of thermal expansion (CTE) between layers. In the case of the multilayered Al_2O_3/3Y-TZP composite, CTE mismatch between Al_2O_3 and 3Y-TZP layers brings compressive and tensile stresses along the layer direction in Al_2O_3 and 3Y-TZP layers, respectively. Since these residual stresses improve the mechanical properties of multilayered composites, it is inferred that control of the residual stress is very important to achieve the improvement of the composites.

On the other hand, nanocomposite technique is known as a method to improve mechanical properties such as strength and toughness [1-8]. Nanocomposite materials have been applied in many fields as structural materials due to their superior mechanical properties. According to the study of nanocomposite materials, the maximum improvement of mechanical properties is achieved by a dispersion of 5 vol% in the matrix [4].

By considering the multilayered composite and nanocomposite posses the different strengthening and toughening mechanisms, it seems that hybrid composites composed of both multilayer-structure and nano-structure give superior mechanical properties as

compared with traditional multilayered composite and traditional nanocomposites. In this study, thus, two types of hybrid composite named as a multilayered nanocomposite and 2-dimensional Dispersed Nanocomposites were attempted to design and develop.

2-2. Al_2O_3/3Y-TZP Multilayered Composites

Al_2O_3/3mol%-Y_2O_3-doped-ZrO_2 (hereafter, 3Y-TZP) multilayered composites, which is consisted of stacking of pure Al_2O_3 and 3Y-TZP layers, have been widely studied in terms of fabrication methods [9-11], mechanical properties [12-14], fracture mechanism [15,16] and residual stress [17].

2-2-1. Directional Residual Stress

Multilayered composites comprising two kinds of layers have both compressive and tensile residual stress. These residual stresses are generated through cooling from sintering temperature by differences of physical properties such as a coefficient of thermal expansion (CTE), Young s modulus, and Poisson s ratio between two layers. Figure 2-1 indicates the mechanism of the generation of the residual stresses. Under high temperature environment such as a sintering process (Fig. 2-1(a)), any stress is released due to a creep behavior (i.e., slide of ceramic grains) and a replacement of the grains. In the cooling process from the high temperature, each layer material is shrunk according to the CTE. When each layer is not bonding rigidly, the degree of the shrinkage is different between each layer (see Fig. 2-1(b)). In reality, however, the layer boundaries have rigid bonding, and then the shrinkage of each layer was restricted and unified to the same shrinkage by induction of strain. By the induced stain, layers with higher CTE are expanded, and layers with lower one are compressed (see Fig. 2-1(c)). Then, tensile and compressive stresses are generated as the residual stress in these layers when cooled to room temperature (Fig. 2-1(d)).

Therefore, in a layer with higher CTE, tensile stress exists in a parallel direction to the layer. On the other hand, in a layer with lower CTE, compressive stress exists in the same direction [18,19].

The CTE values of Al_2O_3 and 3Y-TZP are $8.10\times10^{-6}K^{-1}$ and $10.6\times10^{-6}K^{-1}$, respectively. Therefore, in the Al_2O_3/3Y-TZP multilayered composites, compressive and tensile residual stresses are generated in Al_2O_3 and 3Y-TZP layers in parallel direction to the layer, respectively.

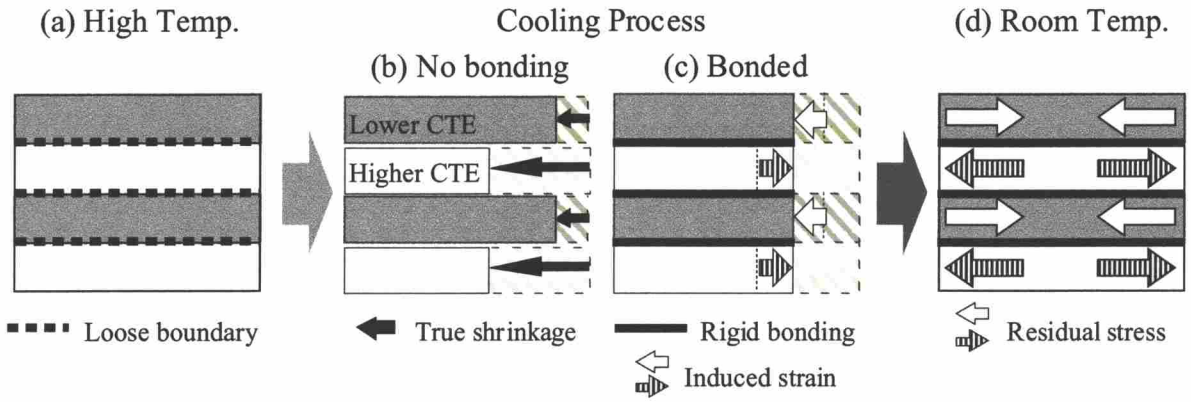

Fig. 2-1 Mechanism of residual stress generation in multilayered composites. (a) At high temperature, any stress is released by creep and replacement of grains. (b,c) In cooling process, strains are induced into layers to reduce the shrinkage difference. (d) At room temperature, residual stresses are generated in each layer.

2-2-2. Mechanisms of Reinforcement

Improvement of the mechanical properties of Al_2O_3/3Y-TZP multilayered composites is achieved by the following three mechanisms indicated in Fig. 2-2.

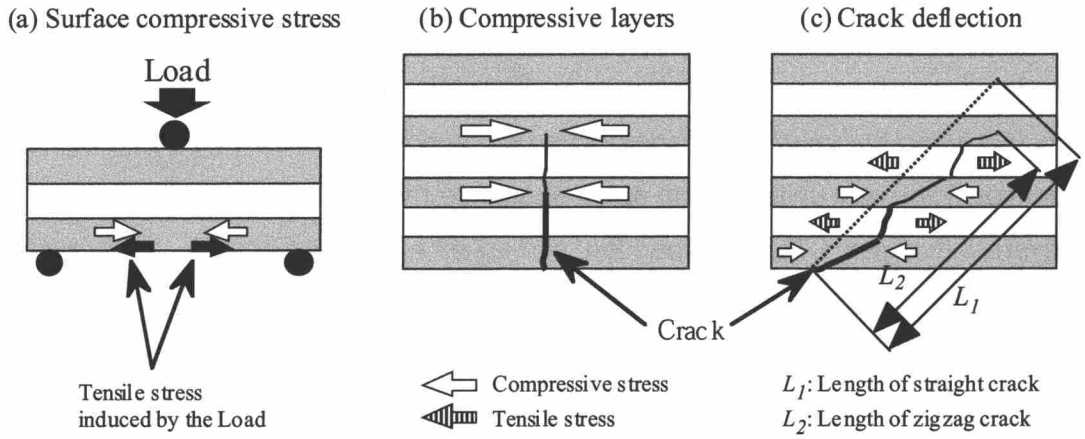

Fig. 2-2 Mechanisms of improvement of mechanical properties. (a) Improvement of apparent strength by surface compressive stress. (b) Crack depression by local compressive stress. (c) Crack deflection at layer boundaries by residual stresses. Dark and white layers correspond to Al_2O_3 and 3Y-TZP layers, respectively.

(1) Improvement of Apparent Strength

When the surface of multilayered composite has compressive residual stress (i.e., Al_2O_3/3Y-TZP multilayered composite with surface Al_2O_3 layers), the surface is reinforced by the compressive stress. Load (*P*) required to cause fracture of material is decided by the intrinsic strength of the material. When the surface has compressive stress, excess load (*P*) is required to cancel the compressive stress of the surface layer. The schematic drawing is shown in Fig. 2-2(a). Therefore, the apparent strength (i.e., load required to cause fracture) is improved in this case.

It is expected that an increase of the surface compressive residual stress leads to the improvement of the apparent strength.

(2) Depression of Crack Propagation

In multilayered composites, each layer has directional residual stress, as mentioned above. Al_2O_3 layers in Al_2O_3/3Y-TZP multilayered composite have compressive residual stresses in parallel direction to the layer. The local compressive stresses repress crack propagation, as shown in Fig. 2-2(b). This fact indicates that the crack repression is effectively achieved when the magnitude of the compressive residual stress is high.

On the other hand, 3Y-TZP layer has tensile stress in the parallel direction. It is expected that the crack propagation in 3Y-TZP layer is promoted. From a study of Al_2O_3/Ce-doped ZrO_2 multilayered composites, it is reported that stress-induced transformation zones of tetragonal ZrO_2 layers are more spread than those of monolithic Ce-doped ZrO_2 ceramics [14]. Since stress-induced transformation in the monoclinic phase from the tetragonal phase of ZrO_2 is accompanied by volume expansion, it is believed that higher tensile stress might promote transformation. Because of the increase of the transformation which brings the improvement of toughness (i.e., repression of the crack propagation), it is not expected that the promotion of crack propagation in 3Y-TZP layers becomes so serious.

(3) Crack Deflection

When a crack propagates across a layer with compressive stress (i.e., Al_2O_3 layers), crack is bent to a parallel direction to the layer by the compressive residual stress. In 3Y-TZP layer with tensile stress, the crack propagates to a perpendicular direction to the layers. Consequently, crack deflections are caused at the layer boundaries [18]. The crack in multilayered composites propagates with zigzag shape as shown in Fig. 2-2(c). Such zigzag

propagation brings increase of fracture energy and decrease of crack length (i.e., the beeline between the starting point and crack tip), when the crack propagates in multilayered composites. The length of the crack in multilayered composite (L_1) is normally shortened than that of monolithic material (L_2).

These effects of *(1)~(3)*, which will be observed in Al_2O_3/3Y-TZP multilayered composites, must bring the improvement of mechanical properties such as fracture strength and toughness. Because these effects are caused by directional residual stress within Al_2O_3/3Y-TZP multilayered composites, it is inferred that the control of the residual stress is important to improve the mechanical properties of the multilayered composites.

2-2-3. Control of Residual Stress

Residual stress within multilayered composites can be divided into macroscopic and microscopic residual stresses. The schematic drawing of each stress is shown in Fig. 2-3. In this study, the macroscopic residual stress is defined as the direction and magnitude of the residual stress of each layer (see Fig. 2-3(a)). This macroscopic residual stress can be calculated from a relationship between elastic property and thermal expansion [19]. The magnitude of the macroscopic residual stress can be obtained as an average value within the layer by the following formulas [19].

$$\sigma_1^{para} = \left[\frac{n_2 E_1 E_2 d_2}{(1-\nu_1) n_2 E_2 d_2 + (1-\nu_2) n_1 E_1 d_1}\right] \Delta\alpha \times \Delta T \qquad \text{(Eq. 2-1)}$$

$$\sigma_2^{para} = -\left[\frac{n_1 E_1 E_2 d_1}{(1-\nu_1) n_2 E_2 d_2 + (1-\nu_2) n_1 E_1 d_1}\right] \Delta\alpha \times \Delta T, \qquad \text{(Eq. 2-2)}$$

where subscripts *1* and *2* correspond to the different layers consisted of multilayered composite, and σ_1^{para} and σ_2^{para} denote the residual stress of each layers in the parallel direction. The magnitude of the macroscopic residual stress (i.e., average value of each layer) is largely proportional to the CTE mismatch ($\Delta\alpha$) between Al_2O_3 and 3Y-TZP, and the temperature difference (ΔT). It is also influenced by Young s modulus (E), Poisson s ratio (ν), number of layers (n), and thickness (d).

These formulas imply that the magnitude of macroscopic residual stress can be controlled by change of the parameters such as Young's modulus, Poisson's ratio, layer thickness,

number of stacked layers, and CTE mismatch. In order to control of the macroscopic residual stress, the thickness of the layers (Chapter 4) and CTE mismatch (Chapters 5 and 6) were controlled in this study.

The microscopic residual stress is also defined as the stress distribution within one layer in this study (see Fig. 2-3(b)). The microscopic residual stress within one layer has parabolic distribution as shown in Fig. 2-3(b) [20]. This parabolic distribution brings a local concentration of residual stress. The stress concentration sometimes causes fracture such as debonding, delamination and channel cracks [21-23]. In this study, control of the microscopic stress distribution was tried by dispersion of nano-sized dispersoid (Chapter 5).

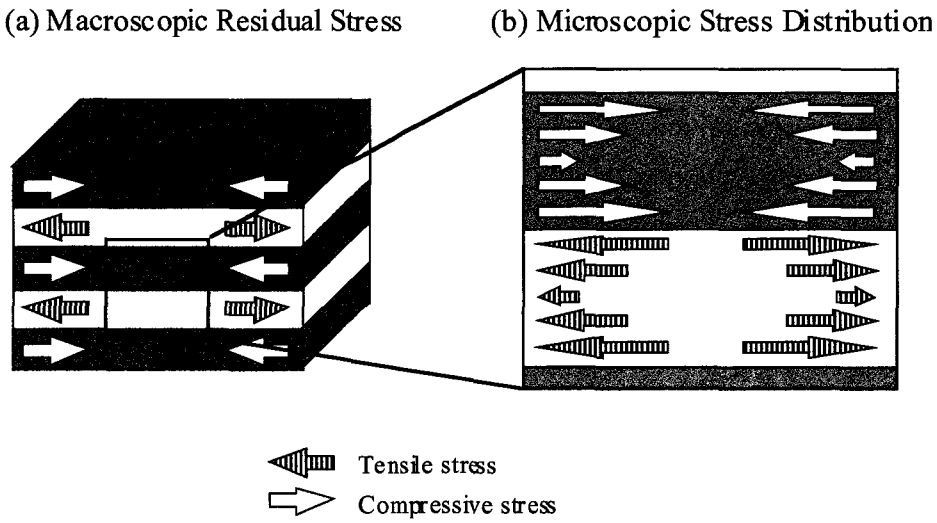

Fig. 2-3 Schematic drawings of (a) macroscopic and (b) microscopic residual stresses within multilayered composite. Dark and white layers correspond to Al_2O_3 and 3Y-TZP layers.

2-3. Multilayered Nanocomposites

2-3-1. Design Concepts

(1) Effects of Nano-particles

It is reported that mechanical properties of Al_2O_3/SiC nanocomposite [7,24-29] and

3Y-TZP/SiC nanocomposite [8] are strongly improved by nano-sized SiC dispersion. Therefore, nano-sized β-SiC particles were dispersed into each layers of the Al_2O_3/3Y-TZP multilayered composites to obtain improvement of mechanical properties of each layer. The schematic drawing is shown in Fig. 1-3(a). In addition, another advantage of SiC dispersion is the low-reactivity with these layer materials under an inactive atmosphere.

(2) Effects of Control of Residual Stress

In addition, nano-sized SiC particles were dispersed into the Al_2O_3/3Y-TZP multilayered composite to also control the residual stress.

Residual stress in multilayered composites depends on the CTE mismatch between each layer material as mentioned in previous part. This mean that residual stress of multilayered composite is controlled (refer Eq. 2-1 and 2-2), by dispersing the nano-sized second phases with different CTE into layers.

Considering the rule of mixture of composite materials, the CTE value of composite is estimated from material composition. In a particle-dispersed composite, for example, the CTE value is calculated from the CTE value of both matrix and dispersion and the volume fraction of dispersion [30]. As a result, the dispersion of nano-sized particles into layer materials yields control of residual stress of multilayered composites. These facts indicate that precise control of residual stress of layered composites can be achieved by choosing appropriate second phase dispersion and controlling their amount.

To control the CTE for this purpose, nano-sized β-SiC dispersoid was chosen, because it has much lower CTE ($4.45\times10^{-6}K^{-1}$) value than Al_2O_3 ($8.10\times10^{-6}K^{-1}$) and 3Y-TZP ($10.6\times10^{-6}K^{-1}$). Consequently, the residual stress can be controlled effectively by a small amount of SiC dispersion such as 5 vol%.

All these discussions imply that dispersion of nano-sized SiC into Al_2O_3 and/or 3Y-TZP layer offers the great advantages to enhance mechanical properties and to control residual stress in the multilayered composite.

2-3-2. Structure

As multilayered nanocomposite, four kinds of multilayered composite were designed as illustrated in Fig. 2-4.

In order to control the residual stress within the multilayered nanocomposites, two

multilayered nanocomposites was designed. One is SiC-dispersed Al_2O_3/3Y-TZP multilayered nanocomposite (hereafter AS/Z: Fig. 2-4(b)), it is expected this composite has highest residual stress due to the highest CTE mismatch. The other is Al_2O_3/SiC-dispersed 3Y-TZP (hereafter, A/ZS: Fig. 2-4(c)) composite with lowest residual stress. From the investigation of these composites, the effects of the residual stress must be estimated.

On the contrary, SiC-dispersed Al_2O_3/SiC-dispersed 3Y-TZP multilayered nanocomposite is designed to improve the mechanical properties by SiC dispersion (see Fig. 2-4(d)). In this structure, the strengthening by nano-sized SiC particles will be strongly demonstrated.

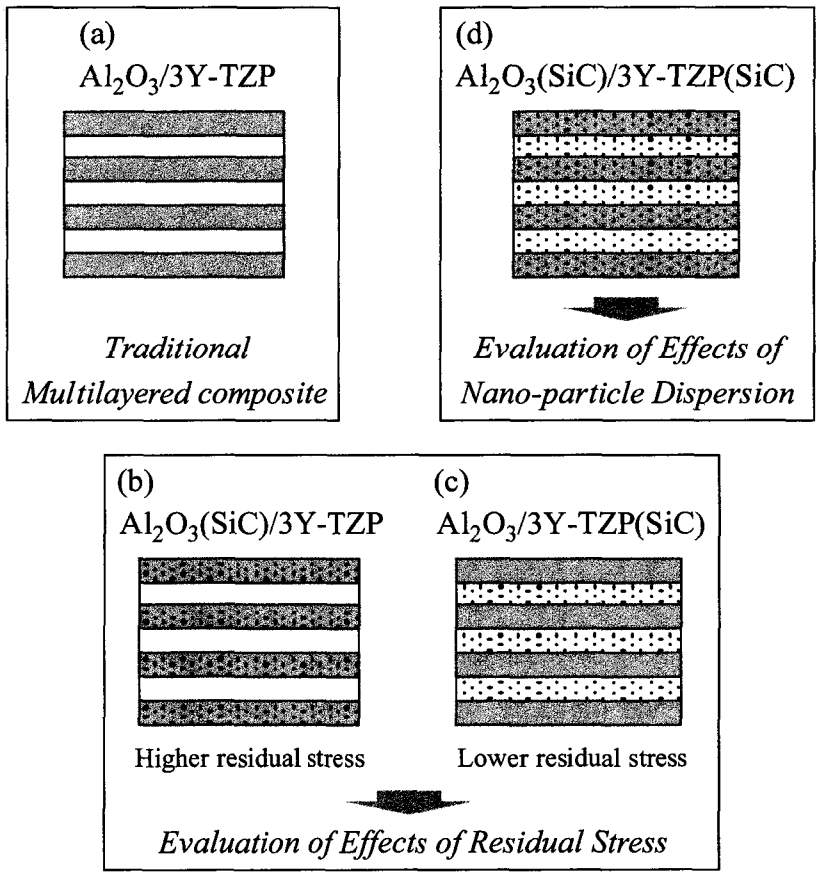

Fig. 2-4 Schematic drawings of (a) traditional multilayered composite and (b,c,d) multilayered nanocomposites designed in this study. In order to control the residual stress within multilayered composites, multilayered nanocomposites (b and c) are designed. These composites have higher and lower residual stress due to their CTE mismatch, respectively. (d) Nano-sized SiC particles are dispersed into both layers; this multilayered nanocomposite has largest effect of nano-particles. Dark and white layers correspond to Al_2O_3 and 3Y-TZP layers, and black dots indicate dispersed SiC nano-particles.

2-4. 2-dimensional Dispersed Nanocomposites

2-4-1. Design Concepts

(1) Induction of Residual Stress

Multilayered structure provides systematic stress field within the composites. The stress field is constituted of two-directional stress component (i.e., parallel and perpendicular directions to the layer direction), and it is produced by the CTE mismatch between each layer material [18-20]. When, nano-sized particle with lower CTE is dispersed into the matrix of a composite material (i.e., nanocomposite), the CTE value of the nanocomposite is decreased than that of matrix monolithic material. In the 2-dimensional dispersed nanocomposite consisted of nanocomposite and monolithic layers (see Fig. 1-4(b)), thus, nanocomposite layer with lower CTE and monolith layer with higher CTE have compressive and tensile stress within each layer, respectively. Also, because magnitude of the residual stress that depends on the layer thickness (refer Eq. 2-1 and 2-2), the magnitude of these residual stresses can be controlled systematically by changing the thickness of each layer.

(2) Bonding of Layers

Generally, when the difference of physical properties such as CTE and Young's modulus between layer materials is large, defects such as debonding, channel crack and microcrack are produced in the multilayered composites [21-23]. Therefore, the combination of the layer materials (i.e., their sinterability and chemical reaction) is important in order to fabricate multilayered composite without any defect. Especially, the difference in sinterability between layer materials increases the difficulty of fabricating multilayered composites without any defects.

In the 2-dimensional dispersed nanocomposites designed in this study, however, the difference of the sinterability between monolithic and nanocomposite layers is small (i.e., nanocomposites and monolith layers have similar sintering behavior through the sintering process). This fact indicates that the bonding of layer is strong, because these layer materials have same sinterability and same matrix.

(3) Control of Residual Stress

Equations 2-1 and 2-2 imply that the magnitude of the residual stress is controllable by

change of the thickness (*d*) of each layer. Therefore, when the thickness of each layer is changed arbitrarily, the magnitude of the residual stress is thought to be controlled.

2-4-2. Structure

In the 2-dimensional dispersed nanocomposites, studied in this work, 3Y-TZP and β-SiC are used as the matrix and dispersoid, because these materials have higher and lower CTE value.

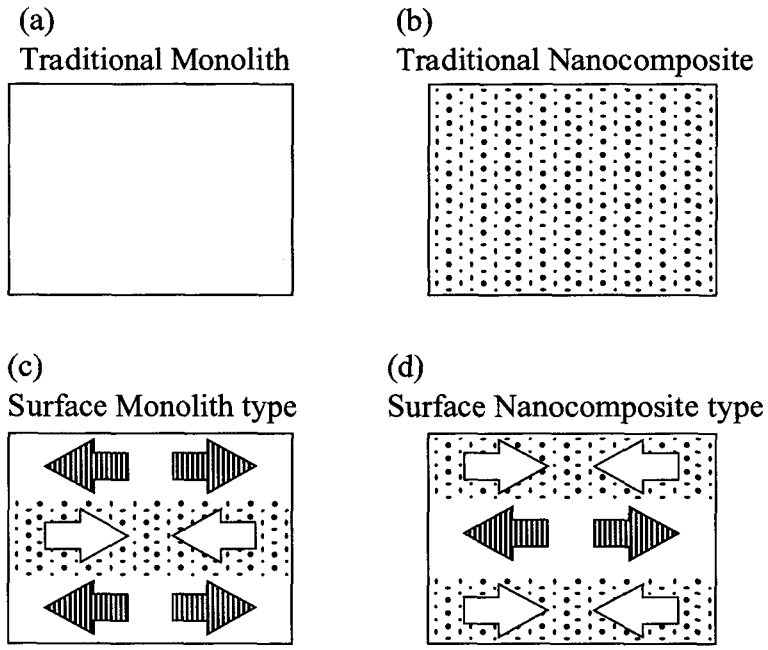

Fig. 2-5 Schematic drawings of (a) traditional monolithic materials, (b) traditional nanocomposite material, and (c,d) 2-dimensional dispersed nanocomposites designed in this study. These 2-dimensional dispersed nanocomposites has directional residual stresses within the composite as indicated as the arrows (dark and white arrows correspond to tensile and compressive stresses, respectively). (c) Surface monolith type has tensile stress in the surface layers. On the contrary, (d) as surface nanocomposite has compressive stress, the surface is strengthened by the compressive stress and nano-particles.

In order to control the residual stress in the 2-dimensional dispersed nanocomposite, two kinds of 2-dimensional dispersed nanocomposites were designed as illustrated in Fig. 2-5(c,d). The 2-dimensional dispersed nanocomposite consists of 3Y-TZP/SiC nanocomposite surface layer (as lower CTE) and 3Y-TZP monolithic inner layer (as higher CTE) has been

designed to obtain compressive stress in the surface layers (see Fig. 2-5(d)). This type of 2-dimensional dispersed nanocomposite has both surface compressive stress (i.e., same mechanism shown in Fig. 2-2(a)) and nano-sized dispersion on the surface. Therefore, it is inferred that the surface of this composite is significantly strengthened. On contrary, another type of 2-dimensional dispersed nanocomposite (see Fig. 2-5(c)), which has monolith surface layer and nanocomposite inner layer, was also designed to compare the properties.

2-5. Summary

In this chapter, the design concept of two types of hybrid composites, in which multilayer and nano structure coexist, is proposed from the strengthening mechanism of multilayered composites and nanocomposites.

The one is the multilayered nanocomposites, in which nano-sized SiC particles are dispersed into Al_2O_3 and/or 3Y-TZP layer of Al_2O_3/3Y-TZP multilayered composite. In this hybrid composite, it is expected that macroscopic residual stress of each layer is controllable by the combination of layer materials. In AS/ZS composite, in which SiC particles were dispersed into both layers, it is expected that the strong effects of nano-particle are observed.

The other hybrid composite is the 2-dimensional dispersed nanocomposites, in which nano-sized SiC particles are dispersed in the surface or inside of 3Y-TZP matrix. By designing this 2-dimensional dispersion, the effects of residual stress can be introduced to nanocomposite material. In this 2-dimensional dispersed nanocomposites, strengthening by both the residual stress and nano-particle, must be demonstrated.

References

[1] K. Niihara, *J. Ceram. Soc. Jpn*, **99**, 974 (1991).

[2] K. Niihara, and A. Nakahira, *Ann. Chim. Fr.*, **16**, 479 (1991).

[3] A. Nakahira, and K. Niihara, in *Fracture Mechanics of Ceramics*, 9. Edited by R. C. Bradt *et al.*, pp. 165-78, Plenum Press, 1992.

[4] T. Ohji, Y.K. Jeong, Y.H. Choa, and K. Niihara, *J. Am. Ceram. Soc.*, **81**, 1453 (1998).

[5] T. Ohji, T. Kusunose, and K. Niihara, *J. Am. Ceram. Soc.*, **81**, 2713 (1998).

[6] J. Zhao, L.C. Stearns, M.P. Harmer, H.M. Chan, G.A. Miller, and R.F. Cook, *J. Am. Ceram. Soc.*, **76**, 503 (1993).

[7] T. Ohji, A. Nakahira, T. Hirano, and K. Niihara, *J. Am. Ceram. Soc.*, **77**, 3259 (1994).

[8] N. Bamba, Y.H. Choa, T. Sekino, and K. Niihara, *J. Eur. Ceram. Soc.*, in press.

[9] E. Lucchini, and O. Sbaizero, *J. Eur. Ceram. Soc.*, **15**, 975 (1995).

[10] P. Sarkar, X. Haung, and P.S. Nicholson, *J. Am. Ceram. Soc.*, **75**, 2907 (1992).

[11] J. Requena, R. Moreno, and J.S. Moya, *J. Am. Ceram. Soc.*, **72**, 2511 (1989).

[12] M. Jimenez-Melendo, F. Gutierrez-Mora, and A. Dominguez-Rodriguez, *Acta mater.*, **48**, 4715 (2000).

[13] D.R. Mumm, D.B. Marshall, A. Griffin, C.W. Griffin, and C.S. Turner, *J. Am. Ceram. Soc.*, **79**, 1416 (1996).

[14] D.B. Marshall, J.J. Ratto, and F.F. Lange, *J. Am. Ceram. Soc.*, **74**, 2979 (1991).

[15] M.P. Rao, and F.F. Lange, *J. Am. Ceram. Soc.*, **85**, 1222 (2002).

[16] M. Oechsner, C. Hillman, and F.F. Lange, *J. Am. Ceram. Soc.*, **79**, 1834 (1996).

[17] V. Sergo, D.M. Lipkin, G.D. Portu, and D.R. Clarke, *J. Am. Ceram. Soc.*, **80**, 1633 (1997).

[18] P. Sajgalik, Z. Lences, and J. Dusza, *J. Mater. Sci.*, **31**, 4837 (1996).

[19] T. Chartier, D. Merle, and J.L. Besson, *J. Eur. Ceram. Soc.*, **15**, 101 (1995).

[20] H. Tomaszewski, J. Strzeszewski, and W. Gebicki, *J. Eur. Ceram. Soc.*, **19**, 255 (1999).

[21] P.Z. Cai, D.J. Green, and G.L. Messing, *J. Am. Ceram. Soc.*, **80**, 1929 (1997).

[22] C. Hillman, Z. Suo, and F.F. Lange, *J. Am. Ceram. Soc.*, **79**, 2127 (1996).

[23] S. Ho, C. Hillman, F.F. Lange, and Z. Suo, *J. Am. Ceram. Soc.*, **78**, 2353 (1995).

[24] E. Yasuda, Q. Bao, and K. Niihara, *J. Ceram. Soc. Jpn.*, **100**, 514 (1992).

[25] G. Sasaki, H. Nakase, K. Suganuma, T. Fujita, and K. Niihara, *J. Ceram. Soc. Jpn.*, **100**, 536 (1992).

[26] T. Sekino, A. Nakahira, M. Nawa, and K. Niihara, *J. Jpn. Soc. Powder Powder Metall.*, **38**, 326 (1991).

[27] M. Nawa, T. Sekino, and K. Niihara, *J. Mater. Sci.*, **29**, 3185 (1995).

[28] T. Sekino, and K. Niihara, *Nanostruct. Mater.*, **6**, 663 (1995).

[29] M. Nawa, K. Yamazaki, T. Sekino, and K. Niihara, *J. Mater. Sci.*, **31**, 2848 (1997).

[30] E. H. Kerner, *Proc. Phys. Soc.*, **B69**, 808 (1956).

CHAPTER 3

Fabrication and Evaluation of Hybrid Composites

3-1. Introduction

Two kinds of hybrid composites, which designed in this study, have both multilayered structure and nano structure. As the fabrication method of ceramic-based composites with multilayered structure, electrophoretic deposition [1], slip casting [2,3], and tape-casting [4-7] have been applied. The doctor blade method, a kind of tape-casting, has been applied to fabricate greensheets with uniform thickness and smooth surfaces as compared with other methods. Multilayered composites constructed by these greensheets have sharp layer boundaries between layer materials. In this study, smooth layer boundaries and uniform thickness were necessary to obtain accurate measurement of residual stress of fabricated composites. Then, all composites were fabricated by stacking greensheets in order to obtain smooth layer boundaries and uniform thickness. In addition, this method enables to control of the thickness of each layer. Therefore, by changing of number of stacked greensheet, it is easy to obtain multilayered composites with various layer thickness.

Multilayered composites with various layer thickness (chapter 4) were prepared by Al_2O_3 and 3Y-TZP greensheets. Multilayered nanocomposites (chapter 5) were fabricated by the combination of four kinds of greensheets (Al_2O_3, 3Y-TZP, SiC-dispersed Al_2O_3, and SiC-dispersed 3Y-TZP). In addition, 2-dimensional dispersed nanocomposites were obtained from 3Y-TZP and SiC-dispersed 3Y-TZP greensheets.

For these composites with both multilayered structure and nano structure, prepared in this study, physical properties, microstructure, mechanical properties, and thermal properties were evaluated.

3-2. Fabrication of Hybrid Composites

The flow chart of experimental procedure is shown in Fig. 3-1. Powders used in the greensheets were α-Al_2O_3 (TM-DAR, Taimei Chemicals Co., Ltd., Japan: average grain size, 0.21 μm), 3Y-TZP (OZC-3YB, Sumitomo Osaka Cement Co., Ltd., Japan: average grain size, <0.1 μm) and β-SiC (Betarundum, Ultrafine grade, Ibiden Co., Ltd., Japan: average grain size, 0.27 μm). Greensheets were obtained from a mixture of Al_2O_3 or 3Y-TZP powder with SiC powder. Each mixture was prepared by ball-milling. The quantity of SiC dispersion in Al_2O_3 or 3Y-TZP was fixed to be 5 vol% in this experiment. Hereafter, Al_2O_3, 3Y-TZP, SiC-dispersed Al_2O_3, and SiC-dispersed 3Y-TZP are denoted as A, Z, AS, and ZS, respectively.

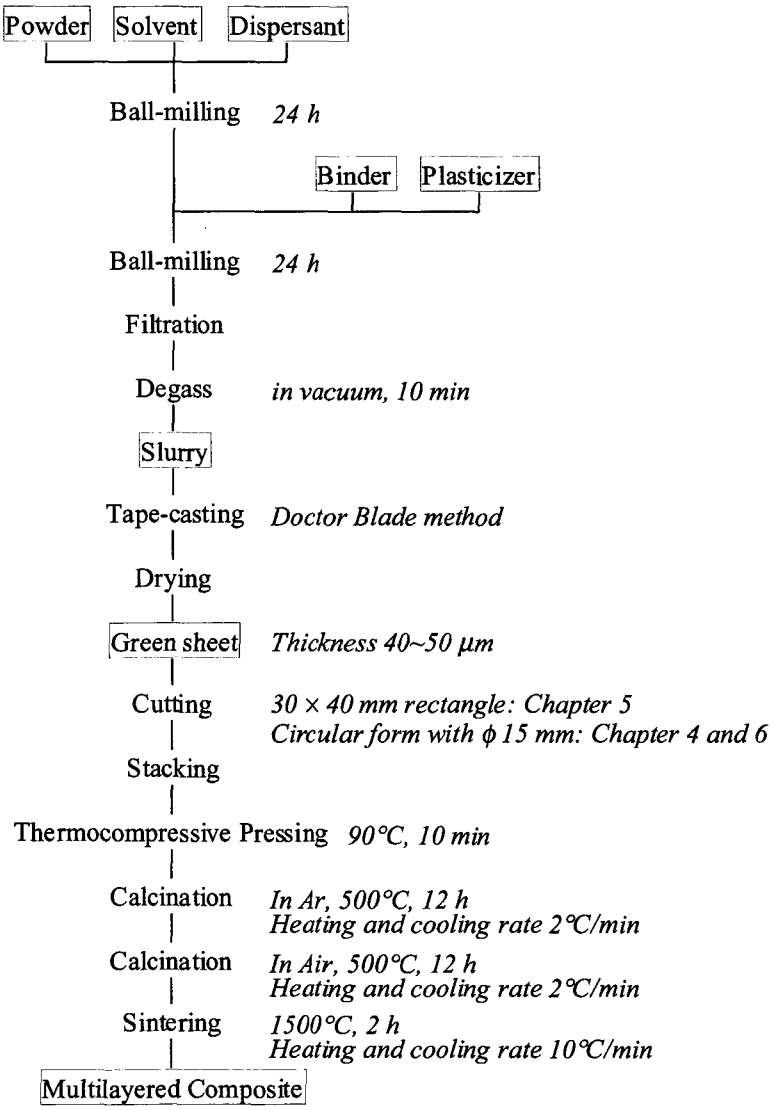

Fig. 3-1 Flow chart of fabrication processes for multilayered hybrid composites.

To prepare four kinds of greensheets of A, Z, AS, and ZS, slurries were prepared using these powders. Initially, each powder was ball-milled with oleic acid as a dispersant in a mixed solvent of methyl ethyl ketone (MEK) and 1-propanol for 24 h. Then, poly(vinyl-butyral) (PVB) and dibuthyl phthalate (DBP) were added to the mixture as a binder and plasticizer, respectively; it was subsequently ball-milled again for 24 h. In Table 3-1, the compositions of Al_2O_3-based and 3Y-TZP-based slurries are listed. After milling, these slurries were filtrated and degassed under vacuum for 10 min.

Table 3-1 Compositions of slurries

Component	Function	Composition of Slurry (vol%)	
		A or AS slurry	Z or ZS slurry
α-Al_2O_3 or 3Y-TZP +SiC(5 vol%)	Ceramic Powder	15.0	12.0
PVB	Binder	6.9	8.4
DBP	Plasticizer	5.7	9.3
Oleic acid	Dispersant	0.9	1.1
MEK	Solvent	55.6	53.8
1-PrOH	Solvent	15.9	15.4

Using these prepared slurries, tape-casting was performed by a doctor blade (DP-100, Tukawa Seiki Co., Ltd., Japan). The casting condition was a casting speed of 200 mm/min and a blade gap of 200 μm. After tape-casting, obtained greensheets were sufficiently dried under room temperature. Then, these greensheets (thickness was approximately 60 μm) were provided for fabrication of hybrid composites. Prior to the stacking of these greensheets, each greensheet was cut in a 30 × 40 mm rectangle (Chapter 5) or a circular form with a diameter of 15 mm (Chapters 4 and 6).

Multilayered composites with various layer thickness (Chapter 4) were fabricated by alternate stacking of both A and Z greensheets. The number of stacked greensheets was changed in the region from 1 to 8 sheets for each layer, as listed in Table 3-2. Hereafter, A*x*Z*y* indicates the fabricated multilayered composite, subscript *x* and *y* denote the number of A and Z greensheets, respectively.

Multilayered nanocomposites (Chapter 5) were obtained by various combinations of four kinds of greensheets. The combination and number of stacked greensheets are listed in Table

3-3. The A/Z multilayered composites, which consisted of A and Z layers, were fabricated by alternate stacking of both A and Z greensheets one by one. Other multilayered composites such as A/ZS, AS/Z and AS/ZS were also fabricated similarly to the A/Z composite.

Table 3-2 Number of stacked greensheet for AxZx and AxZy multilayered composite

Sample Name	Number of Greensheets for one layer (sheets)		Number of Layers of multilayered composite (layers)			Total of Greensheets (sheets)
	A	Z	A	Z	Total	
A1Z1	1	1	26	25	51	51
A2Z2	2	2	13	12	25	50
A4Z4	4	4	7	6	13	52
A8Z8	8	8	4	3	7	56
A1Z3	1	3	13	12	25	49
A1Z2	1	2	17	16	33	49
A2Z1	2	1	18	17	35	53
A3Z1	3	1	13	12	25	51

Table 3-3 Combination and number of stacked greensheet for multilayered nanocomposite

Sample Name	Number of Greensheets of one layer and layer combination (sheets)				Number of Layers of multilayered composite (layers)		
	A	AS	Z	ZS	A or AS	Z or ZS	Total
A/Z	1		1		26	25	51
A/ZS	1			1	26	25	51
AS/Z		1	1		26	25	51
AS/ZS		1		1	26	25	51

The 2-dimensional dispersed nanocomposites were obtained by stacking of Z and ZS greensheets, combination and number of each greensheet are listed in Table 3-4. Hereafter, the surface nanocomposite consists of nanocomposite surface layers with monolith inner layers, is denoted as N.Surf.(*n*), and the surface monolith consists of monolith surface layers with nanocomposite inner layers, is as M.Surf.(*n*). The variable *n* indicates the number of greensheets stacked to form one surface layer. In addition, a bulky monolithic 3Y-TZP obtained by stacking only Z greensheets, and a bulky traditional 3Y-TZP/SiC nanocomposite

that comprised only ZS greensheets are denoted as M.Bulk and N.Bulk, respectively.

To ensure rigid bonding between each greensheet of the stacked greensheets, thermocompressive pressing was carried out at 90°C for 10 min. After this pressing, the obtained green compacts had rigid bonding between each greensheet, and were like a bulky compact.

Table 3-4 Combination and number of stacked greensheet for 2-dimensional dispersed nanocomposite

Sample Name	Number of greensheet (sheets)			
	Surface	Inner	Surface	Total
M.Bulk				35
M.Surf.(5)	5	25	5	35
M.Surf.(7)	7	20	7	34
M.Surf.(10)	10	15	10	35
M.Surf.(12)	12	10	12	34
M.Surf.(14)	14	6	14	34
N.Bulk				35
N.Surf.(5)	5	25	5	35
N.Surf.(7)	7	20	7	34
N.Surf.(10)	10	15	10	35
N.Surf.(12)	12	10	12	34
N.Surf.(14)	14	6	14	34

The obtained green compacts were then calcinated to burn out all organic reagents. A calcination conditions were decided from results of a thermogravimetry - differential thermal analysis (TG-DTA: DTG-50, Shimadzu Co., Japan) of green composites. The weight change of green compact is shown in Fig. 3-2. Since a weight loss of the heat-treated composite was not observed above 500°C due to a complete burn-out of all organic

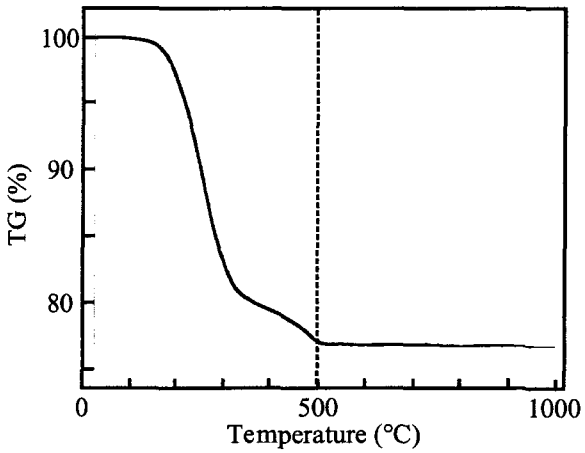

Fig. 3-2 TG analysis of obtained green compact.

reagents.

Then, the calcination was carried out at 500°C. Preliminary experiments revealed that fractures such as delamination and debonding occurred during the calcination under an air atmosphere, even though heating was carried out slowly. To prevent delamination and debonding of multilayered composites in this study, therefore, the calcination was carried out twice: in an Ar atmosphere for the first calcination and then in an air atmosphere. Soaking temperature for the twice calcinations was 500°C for 12 h. Heating and cooling rates were fixed to be 2°C/min to avoid a temperature gradient of the green compact. Also, a sample was kept for 2 h at every 100°C to achieve a uniform burn-out during heating for both the calcination. After the first calcination, all samples were blackened, a result of residual carbon from organic reagents. By the twice calcination, neither delamination nor debonding occurred in the calcinated sample; the color changed to white from black. These results indicate that burning out of the organic reagent as well as residual carbon was completed by the double heating.

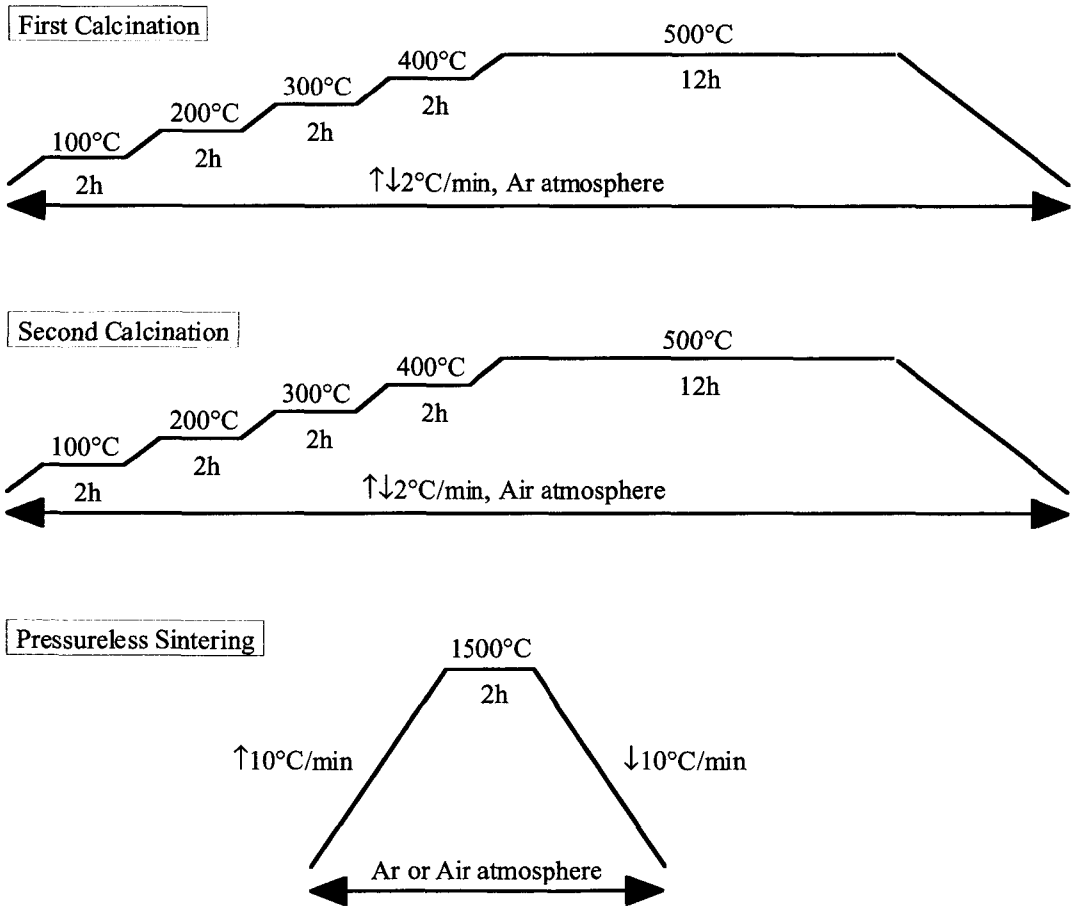

Fig. 3-3 Diagram of twice calcinations and pressureless sintering schedule.

Then, these calcinated composites were pressureless sintered at 1500°C for 2 h under an air atmosphere (Chapter 4) or an Ar atmosphere (Chapters 5 and 6) to prevent an SiC oxidation. Heating and cooling rates were 10°C/min. The diagram of the twice calcination and the sintering are shown in Fig. 3-3.

For several evaluations, the obtained composites were grinded and polished the cross section and top and bottom surfaces.

3-3. Evaluation of Hybrid Composites

3-3-1. Density

The density of obtained composites was measured by Archimedes principle using toluene solvent at room temperature. The bulk density was determined by

$$\rho = \rho_T \left(\frac{m_1}{m_1 - m_2} \right) \quad \text{(Eq. 3-1)}$$

$$\rho_T = 0.88412 - 0.00092248 \times t \quad \text{(Eq. 3-2)}$$

where ρ, ρ_T, m_1, m_2, and t mean bulk density (g/cm^3) of the specimen, density of toluene (g/cm^3), weight (g) of specimen in air and the solvent, and the temperature (C) of the toluene, respectively.

Theoretical density of the nanocomposite material, in which SiC nano-particle dispersed, was calculated by the follow as,

$$\rho_{AS} = \rho_{Al_2O_3} V_{Al_2O_3} + \rho_{SiC} V_{SiC} \quad \text{(Eq. 3-3)}$$

$$\rho_{ZS} = \rho_{3Y-TZP} V_{3Y-TZP} + \rho_{SiC} V_{SiC} \quad \text{(Eq. 3-4)}$$

where ρ_x and V_x indicate the theoretical density and volume fraction of material x. The theoretical densities of Al_2O_3, 3Y-TZP and SiC were regarded as 3.99, 6.08 and 3.21 (g/cm^3), respectively. The volume fraction of SiC dispersion was fixed to 5 vol%.

The theoretical density (ρ_{th}: g/cm^3) and relative density (ρ_r: g/cm^3) of the multilayered composites were calculated by

$$\rho_{th} = \rho_A \times \left(\frac{d_A}{d_A + d_Z} \right) + \rho_Z \times \left(\frac{d_Z}{d_A + d_Z} \right) \quad \text{(Eq. 3-5)}$$

$$\rho_r = \frac{\rho}{\rho_{th}} \times 100 \quad \text{(Eq. 3-6)}$$

where d indicates the average layer thickness of the each layer material of the multilayered composites, and subscript A and Z means Al_2O_3-based 3Y-TZP-based materials, respectively.

3-3-2. Identification of Crystalline Phase

Crystalline phases of obtained composites were identified by X-ray diffraction (XRD) analysis using a Rigaku Rotaflex diffractometer (RU-200B, Rigaku Co., Ltd., Japan) with a CuKα radiation (l = 0.15418 nm) operated at 50 kV and 150 mA. The identification of phases present in the composites was referred to Joint Commit of Powder Diffraction Standards (JCPDS) data.

3-3-3. Microstructural Observation

Microstructural observation of the fabricated composites was carried out by optical microscope, scanning electron microscope (SEM: S-5000, Hitachi Co., Ltd., Japan), and transmission electron microscope (TEM: H-8100, Hitachi Co., Ltd., Japan, 200 kV).

Estimation of the layer thickness, observation of visible cracks and crack propagation behavior were done by Optical microscope. Microstructure near the layer boundary and microcracks were observed by SEM. Bonding of layer material and SiC dispersion were observed by TEM.

To carry out these observations, the fabricated composites were grinded and polished their cross section.

3-3-4. Residual Stress Measurement

Residual stress was measured by XRD analysis using X-ray diffractometer with position sensitive proportional counter (PSPC) (PSPC-RSF, Rigaku Co., Ltd., Japan) [8-10]. For multilayered nanocomposites, macroscopic residual stress (i.e., average residual stress of the each layer) and microscopic residual stress (i.e., stress distribution within 3Y-TZP-based layer) were measured (see Chapter 5). The macroscopic residual stress was measured using collimator with ϕ 2 mm in diameter. The measurement area was on the cross section of the multilayered nanocomposites. The stress distribution within the 3Y-TZP-based layer was

measured by collimator with ϕ 150 μm in diameter. On the other hand, surface stress of the 2-dimensional dispersed nanocomposites was measured using collimator with ϕ 4 mm in diameter at the top surface of the composite. The schematic drawings of three kinds of the stress measurement are shown in Fig. 3-4. The details for each measurement will be mentioned in their Chapters.

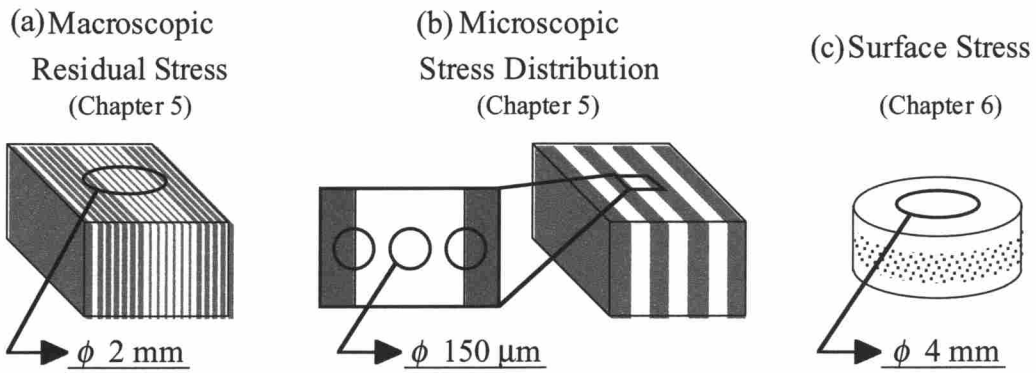

Fig. 3-4 Schematic drawings of stress measured area by XRD analysis. Macroscopic residual stress (a), microscopic residual stress (b) and surface stress (c) are measured in the circules.

3-3-5. Mechanical Properties

In this study, mechanical properties such as hardness, Indentation fracture (IF) toughness and crack propagation behavior were evaluated by Vickers indentation test using Vickers indenter (AVK-C2, Akashi Co., Ltd., Japan).

For multilayered nanocomposite (Chapter 5), crack propagation behavior was also evaluated by measuring the crack shape, which was induced on the cross section of the composites by Vickers indenter.

As the evaluation of mechanical properties of 2-dimensional dispersed nanocomposites (Chapter 6), Vickers hardness and Indentation fracture (IF) toughness were measured on their top surface in which surface stress measured. The details on the mechanical properties for each composite will be mentioned in their Chapters.

3-3-6. Thermal Properties

Thermal conductivity, specific heat and thermal diffusivity were measured by laser flash

method for 2-dimensional dispersed nanocomposite. The detail will be discussed in Chapter 6.

3-4. Summary

Multilayered composites, multilayered nanocomposites and 2-dimensional dispersed nanocomposites were successfully fabricated by various combinations of greensheets. Greensheets were obtained by doctor blade method; it was empirically found that the composition of the slurry was most important to prepare a greensheet with good handling. Although these composites were fabricated by try and error, fractures, which were caused during the process, could be reduced by optimization of the process such as calcination and sintering conditions.

Fabricated composites were evaluated the microstructure, the mechanical properties, thermal properties and so on. In order to evaluate the relationship between residual stress and mechanical properties or thermal properties, the residual stress of the composites was measured by XRD analysis in three ways: macroscopic residual stress (i.e., average stress value of each layer), microscopic residual stress (i.e., stress distribution within a layer) and surface stress.

References

[1] P. Sarkar, X. Haung, and P.S. Nicholson, *J. Am. Ceram. Soc.*, **75**, 2907 (1992).

[2] J. Requena, R. Moreno, and J.S. Moya, *J. Am. Ceram. Soc.*, **72**, 1511 (1989).

[3] E. Lucchini, and O. Sbaizero, *J. Eur. Ceram. Soc.*, **15**, 975 (1995).

[4] K.P. Plucknett, C.H. Caceres, C. Hughes, and D.S. Wilkinson, *J. Am. Ceram. Soc.*, **77**, 2145 (1994).

[5] R.E. Mistler, *Am. Ceram. Soc. Bull*, **69**, 1022 (1990).

[6] R.E. Mistler, *Am. Ceram. Soc. Bull*, **77**, 82 (1998).

[7] J.C. Williams; pp. 173-98 in Ceramic Fabrication Processes [Treaties on Material Science and Technology], vol. 9, Edited by F. F. Y. Wang. Academic Press, New York, 1976.

[8] B. D. Cullity, Measurement of Residual Stress, ; pp. 447-78 in *Elements of X-ray*

Diffraction, Edited by M. Cohen. Addison-Weslay Pub. Co., 1978.

[9] T. Goto, and S. Ohya, *J. Soc. Mat. Sci., Japan*, **47**, 1188 (1998).

[10] K. Tanaka, and Y. Akiniwa, *J. Soc. Mat. Sci., Japan*, **47**, 1301 (1998).

CHAPTER 4

Al_2O_3/3Y-TZP Multilayered Composites

4-1. Introduction

Al_2O_3/3Y-TZP multilayered composites have been widely studied, because the composites have many advantages as mentioned in Chapter 2 [1-9]. The improvement of the mechanical properties is caused by the directional residual stress within the composites. The magnitude of the residual stress can be also controlled by change of the thickness of each layer [10]. By fabricating Al_2O_3/3Y-TZP multilayered composites with various thickness of Al_2O_3 and 3Y-TZP layers, the optimization of the layer thickness of the composites was carried out in order to control the residual stress within the composites.

4-2. Experimental Procedure

The Al_2O_3/3Y-TZP multilayered composites with various layer thickness were fabricated by stacking of A and Z greensheets. The layer thickness was controlled by variations of number of greensheets. The number of stacked greensheets is listed in Table 3-2. Hereafter, A1Z1, A2Z2, A4Z4, and A8Z8 are collectively denoted as AxZx (i.e., multilayered composites with same thickness ratio of A and Z layers). On the other hand, AxZy, which has several thickness ratios, indicates the group of A1Z1, A2Z1, A3Z1, A1Z2, and A1Z3. Refer to Chapter 3 for the details of the fabrication method.

The microstructure of these obtained multilayered composites was observed by optical microscope on the cross section of each composite.

4-3. Microstructure

The appearance on the cross section of AxZx composites is shown in Fig. 4-1. In A1Z1, any defect was not observed on the cross section. In the other composites (i.e., A2Z2, A4Z4 and A8Z8), however, many channel cracks [11,12] were observed in Z layer on the cross sections. But, the defect such as debonding was not observed.

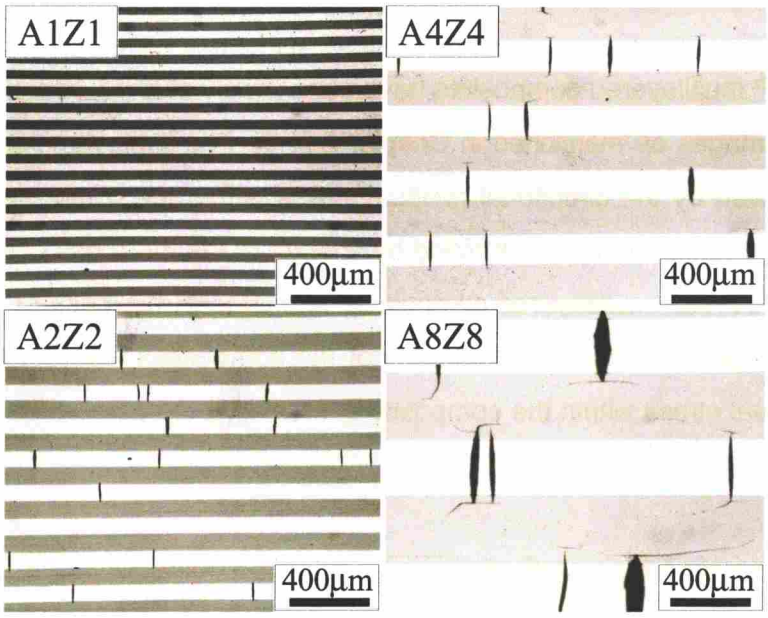

Fig. 4-1 Optical microscopic images of the cross sections for multilayered composites, AxZx, with difference layer thickness. White layers is 3Y-TZP and dark layers are Al_2O_3. In A2Z2, A4Z4 and A8Z8, channel cracks were observed in 3Y-TZP layers.

Figure 4-2 indicates the appearance of the cross section of AxZy composites. In A2Z1 and A3Z1, many channel cracks were observed in Z layer. On the contrary, A1Z2 has few channel cracks in the layer. For A1Z3, the sintered composite was not obtained, because serious debonding between A and Z layers was caused during the sintering process.

The thickness of A and Z layers of each multilayered composites is listed in Table 4-1. In addition, the thickness of A layer to Z layer (i.e., thickness ratio, A/Z) is also indicted in this Table. The thickness ratio (A/Z) of AxZx was approximately 1.1~1.2. AxZy has various thickness ratio, and the region was 0.5~4.6. Here, the thickness ratio of A1Z3 was estimated

from the thickness of single layer of the other multilayered composites. The thickness of each layer was used for the calculation of the residual stress in the following section.

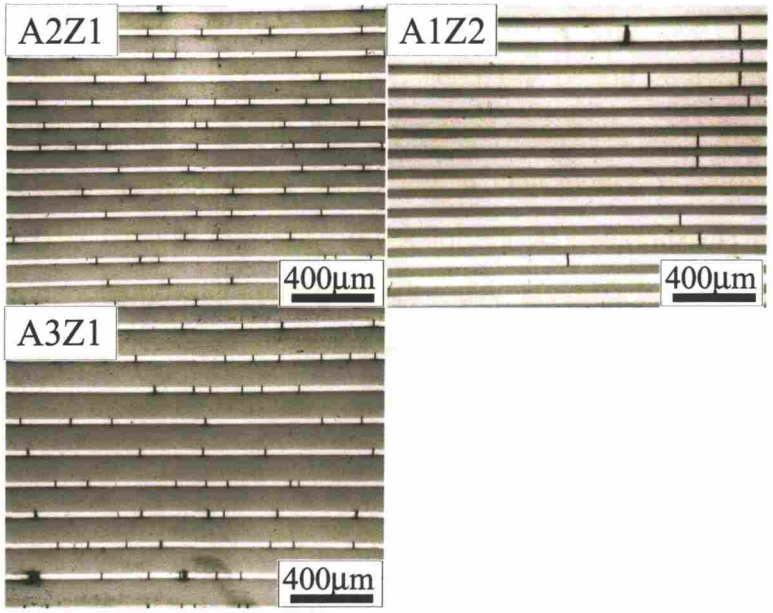

Fig. 4-2 Optical microscopic images of the cross sections for multilayered composites, AxZy, with various ratio of layer thickness. White and dark layers are corresponding to 3Y-TZP and Al_2O_3. In A2Z1, A3Z1 and A1Z2, channel cracks were observed in 3Y-TZP layers.

Table 4-1 Measured layer thickness and calculated residual stress for AxZx and AxZy multilayered composites

Composite	Thickness			Calculated Residual Stress			Fracture	
	A (μm)	Z (μm)	Ratio (A/Z)	A (MPa)	Z (MPa)	Difference (MPa)	Debonding	Channel Crack
A1Z1	43	40	1.1	-430	460	890	—	—
A2Z2	86	**77**	1.1	-420	470	880	—	**many**
A4Z4	171	**147**	1.2	-410	470	880	—	**many**
A8Z8	317	**271**	1.2	-400	470	880	—	**many**
A1Z3	41	**81**	0.5	-670	340	1000	debonding	?
A1Z2	42	**58**	0.7	-550	400	950	—	**few**
A2Z1	83	28	3.0	-200	*580*	780	—	*many*
A3Z1	123	27	4.6	-130	*610*	750	—	*many*

4-4. Calculation of Macroscopic Residual Stress

Macroscopic residual stress value of A and Z layers of the multilayered composites was calculated in order to explain the channel crack generation.

Residual stress within a multilayered composite was generated from the CTE mismatch between layer materials during the cooling process [10]. In A layers with lower CTE, compressive stress was produced in the parallel direction to the layer, whereas tensile stress was produced in Z layer with higher CTE in same direction. The magnitude of these residual stresses is expressed by the following equations (Eq. 4-1 and 4-2), depending on the thickness (d) of A and Z layers. Also, the magnitude is proportional to the CTE mismatch ($\Delta\alpha$: α_2 - α_1), between A and Z, and a temperature difference (ΔT : 1000°C), and influenced by Young s modulus (E), Poisson s ratio (v), and number of layers (n) [10].

$$\sigma_A^{para} = \left[\frac{n_Z E_A E_Z d_Z}{(1-v_A) n_Z E_Z d_Z + (1-v_Z) n_A E_A d_A} \right] \Delta\alpha \times \Delta T \qquad \text{(Eq. 4-1)}$$

$$\sigma_Z^{para} = -\left[\frac{n_A E_A E_Z d_A}{(1-v_A) n_Z E_Z d_Z + (1-v_Z) n_A E_A d_A} \right] \Delta\alpha \times \Delta T, \qquad \text{(Eq. 4-2)}$$

where subscripts A and Z correspond to the Al_2O_3 and 3Y-TZP layers and σ_A^{para} and σ_B^{para} denote residual stress of A and Z layers in the parallel direction. The characteristic values of CTE, Young's modulus and Poisson's ratio are summarized in Table 4-2. These physical properties were used for the calculation of the residual stress of each multilayered composite. The number of layers (n), which used in the Eq. 4-1 and 4-2, is listed in Table 3-2.

Table 4-2 Physical properties of Al_2O_3 and 3Y-TZP used in the calculation of residual stress of Al_2O_3/3Y-TZP multilayered composites.

		Al_2O_3	3Y-TZP
CTE, α	($10^{-6}K^{-1}$)	8.10	10.60
Young's modulus, E	(GPa)	400	200
Poisson's ratio, v	(-)	0.236	0.270

The calculated residual stress is listed in Table 4-1. For AxZx composites, the value of the macroscopic residual stress was almost same among the A1Z1, A2Z2, A4Z4, and A8Z8 due to the same thickness ratio. Therefore, the stress difference between A and Z layers was almost same value. On the other hand, the residual stress of AxZy with various thickness ratios was changed in the wide region. For example, A1Z3 had higher compressive stress and lower tensile stress in A and Z layers, respectively. Then, the stress difference indicated highest value as 1000 MPa among the composites. The lowest stress difference as 750 MPa was observed in A3Z1; this composite had lower compressive and higher tensile stress in the A and Z layers, respectively.

4-5. Mechanism of Channel Crack Formation

The styles of the fracture observed in the fabricated multilayered composites are listed in Table 4-1. Channel cracks were observed for all multilayered composites except for A1Z1 and A1Z3 (see Fig. 4-1 and 4-2). It was considered that the channel crack was caused by the tensile stress of Z layers.

4-5-1. Effect of Average Tensile Stress (A1Z1, A2Z1, and A3Z1)

Although A1Z1 composite has tensile stress as 460 MPa in the Z layer, the channel crack was not formed in the Z layers. On the other hand, because A2Z1 and A3Z1 have higher tensile stress compared with A1Z1, the channel crack was formed in Z layers of these composites. The mechanism of the channel crack formation is shown in Fig. 4-3. The calculated residual stress means an average value of true residual stress. In A2Z1, the average tensile stress of Z layers is higher than that of A1Z1. It is considered that the channel crack formation was caused by the increase of the average tensile stress of Z layer. In the composites which have thick A layers, it was considered that channel cracks were formed by the average tensile stress. The threshold value of the average tensile stress to form the channel crack was estimated as approximately 460~580 MPa.

A1 Z1 Al_2O_3 : 3Y-TZP = 1 : 1

Average tensile stress in Z layer : Middle

Lower maximum tensile stress near layer boudaries

→ No Channel Crack

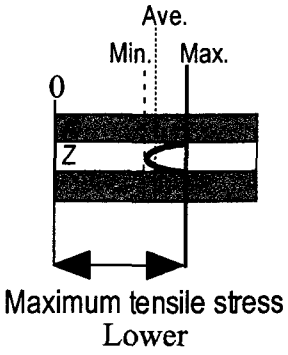

Maximum tensile stress Lower

A2 Z1 Al_2O_3 : 3Y-TZP = 2 : 1

Average tensile stress in Z layer : Higher

Lower maximum tensile stress near layer boudaries

→ Many Channel Crack

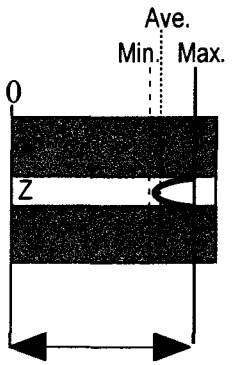

Maximum tensile stress Higher

Fig. 4-3 Mechanism of channel crack formation. Schematic drawing indicates the microscopic stress distribution within 3Y-TZP layers of A1Z1 and A2Z1. In A2Z1, channel cracks were formed due to the higher average tensile stress of Z layers.

4-5-2. Effect of Stress Distribution (A1Z1, A2Z2, A4Z4, and A8Z8)

In A2Z2, A4Z4 and A8Z8 (these composites have almost same average tensile stress with A1Z1: see Table 4-1), many channel cracks observed on the cross sections (see Fig.4-1). To explain this result, the discussion on microscopic stress distribution within Z layers is necessary. The mechanism of the channel crack formation in AxZx with x≥2 is shown in Fig. 4-4. AxZx with x≥1 (i.e., A1Z1, A2Z2, A4Z4, and A8Z8) have same average tensile stress in the Z layers (see Table 4-1). However, the distribution was significantly difficult between these composites. It is reported that the distribution of the residual stress of multilayered composites has a parabolic shape [13]. In addition, it is expected that layer boundary has highest value of the residual stress within the layer. When the shape of the distribution was same between the A1Z1 and the others, the stress distribution of the AxZx

with x≥2 is the shape as shown in Fig. 4-4 (in the case of x=2). The shape has much higher tensile stress near the layer boundaries compared with the A1Z1. Therefore, it is believed that this higher tensile stress near layer boundary causes the channel crack in Z layer. Considering the microscopic stress distribution, the thickness of Z layer seems as the most important factor on the mechanism for the channel crack. From the thickness of these composites, it is inferred that the threshold thickness of Z layer to form a channel crack was estimated as approximately 40~77 μm.

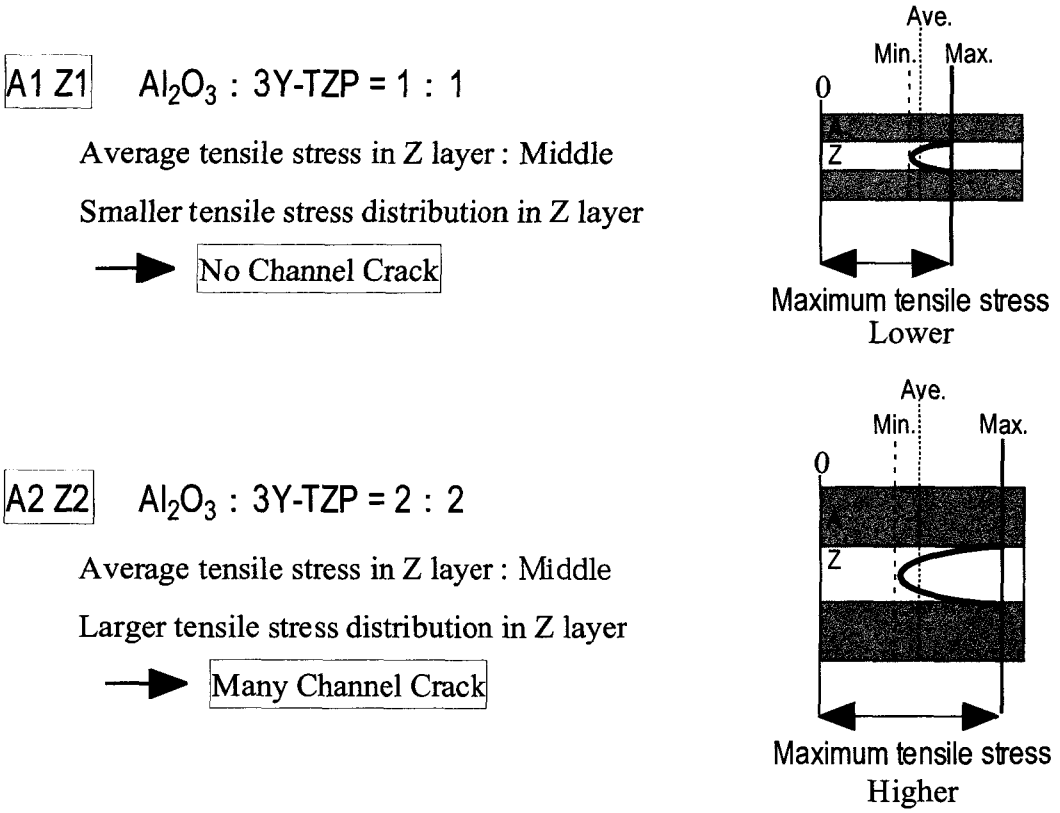

Fig. 4-4 Mechanism of channel crack formation. Schematic drawing indicates the microscopic stress distribution within 3Y-TZP layers of A1Z1 and A2Z2. In A2Z2, channel cracks were formed by concetration of tensile stress near the layer boundaries.

A1Z2 composite has lower average tensile stress as 400 MPa compared with the threshold tensile stress of channel crack formation. However, in this composite, few channel crack was observed in the Z layers (see Fig. 4-2). Considering the above discussion, the thickness of Z layer of A1Z2 (58 μm) was not so thicker than that of A2Z2 (77 μm), but it

was thicker than that of Z layer of A1Z1 (40 μm). Therefore, it was believed that the channel crack was caused by the microscopic stress distribution (i.e., the thickness of the Z layer).

4-5-3. Effect of Stress Difference (Debonding in A1Z3)

In A1Z3, the debonding between layers was caused during the sintering process. Therefore, the sound multilayered composite could not fabricated in this study. A1Z3 has the highest stress difference as 1000 MPa between A and Z layers. Thus, it is inferred that the stress difference caused the debonding of the composite. Because such debonding was not caused in A1Z2, which has 950 MPa as the stress difference, the threshold value of the stress difference to cause the debonding was estimated as approximately 950~1000 MPa.

4-6. Summary

In this chapter, the optimization of layer thickness was carried out by evaluation of Al_2O_3/3Y-TZP multilayered composites with various thickness of A and Z layers.

In A1Z1 composite, any defects such debonding and channel crack were not observed from the optical microscopic observation. However, in the other composites (i.e., AxZx with $x \geq 2$ and AxZy), channel cracks were observed in Z layers. In addition, A1Z3 could not be successfully fabricated due to the debonding between layers during the sintering process.

From the calculation of the macroscopic residual stress within each multilayered composites, the mechanism of generating these fracture was investigated. Consequently, it was revealed that the channel crack was formed by two reasons. One was the macroscopic residual stress (i.e., average tensile stress), and another was the microscopic stress distribution (i.e., the thickness of Z layer). Each threshold value of channel crack generation was estimated as 460~580 MPa and 40~77 μm, respectively. Furthermore, it was found that the stress difference between A and Z layers caused the debonding of the composites, when the stress difference exceeds 1000 MPa.

From these investigation, it was concluded that the control of residual stress was difficult only by changing the layer thickness of Al_2O_3/3Y-TZP multilayered composites.

References

[1] E. Lucchini, and O. Sbaizero, *J. Eur. Ceram. Soc.*, **15**, 975 (1995).

[2] P. Sarkar, X. Haung, and P.S. Nicholson, *J. Am. Ceram. Soc.*, **75**, 2907 (1992).

[3] J. Requena, R. Moreno, and J.S. Moya, *J. Am. Ceram. Soc.*, **72**, 2511 (1989).

[4] M. Jimenez-Melendo, F. Gutierrez-Mora, and A. Dominguez-Rodriguez, *Acta mater.*, **48**, 4715 (2000).

[5] D.R. Mumm, D.B. Marshall, A. Griffin, C.W. Griffin, and C.S. Turner, *J. Am. Ceram. Soc.*, **79**, 1416 (1996).

[6] D.B. Marshall, J.J. Ratto, and F.F. Lange, *J. Am. Ceram. Soc.*, **74**, 2979 (1991).

[7] M.P. Rao, and F.F. Lange, *J. Am. Ceram. Soc.*, **85**, 1222 (2002).

[8] M. Oechsner, C. Hillman, and F.F. Lange, *J. Am. Ceram. Soc.*, **79**, 1834 (1996).

[9] V. Sergo, D.M. Lipkin, G.D. Portu, and D.R. Clarke, *J. Am. Ceram. Soc.*, **80**, 1633 (1997).

[10] T. Chartier, D. Merle, and J.L. Besson, *J. Eur. Ceram. Soc.*, **15**, 101 (1995).

[11] P.Z. Cai, D.J. Green, and G.L. Messing, *J. Am. Ceram. Soc.*, **80**, 1929 (1997).

[12] C. Hillman, Z. Suo, and F.F. Lange, *J. Am. Ceram. Soc.*, **79**, 2127 (1996).

[13] H. Tomaszewski, J. Strzeszewski, and W. Gebicki, *J. Eur. Ceram. Soc.*, **19**, 255 (1999).

CHAPTER 5

Al_2O_3/3Y-TZP Multilayered Nanocomposites

5-1. Introduction

Al_2O_3/3Y-TZP multilayered nanocomposites, in which nano-sized SiC particles dispersed, were designed in Chapter 2 and fabricated in Chapter 3. For the multilayered nanocomposites, nano-sized SiC was dispersed in order to control the residual stress and to investigate the nanocomposite effect.

Microstructure of the obtained multilayered nanocomposites was observed by optical microscope, SEM and TEM. As an evaluation of the residual stress of the multilayered nanocomposites, macroscopic residual stress (i.e., average value of residual stress of the layers) and microscopic stress distribution (i.e., direction and magnitude of residual stress within one layer) were measured by XRD analysis. And the relationship between the residual stress and crack propagation behavior were investigated.

5-2. Experimental Procedure

The A/Z multilayered composites, which consisted of Al_2O_3 (A) and 3Y-TZP (Z) layers, were fabricated by alternate stacking of A and Z greensheets. Other multilayered composites such as A/ZS, AS/Z and AS/ZS were also fabricated similarly to the A/Z composite; refer to Chapter 3 for the details of the fabrication method. For the measurement of the microscopic stress distribution, multilayered composites with thick layers were fabricated. In order to measure the stress distribution within Z layer, A8Z8 (refer to Chapter 4 for the details) was used. A8ZS8 comprised of Al_2O_3 and SiC dispersed 3Y-TZP (ZS) layers was fabricated similarly to the A8Z8 composite using A and ZS greensheets. These composites were used for the measurement of the stress distribution within 3Y-TZP-based layer.

All evaluation was carried out on the cross section of the composites, after the cross

sections were grinded and polished.

5-3. Microstructure

5-3-1. Identification of Crystalline Phase

Crystalline phase of the fabricated multilayered nanocomposites was identified by XRD. The XRD patterns of the composites are shown in Fig. 5-1. All peaks were attributed to Al_2O_3 and 3Y-TZP. The peak derived from SiC dispersion was not observed due to the small content as 5 vol%.

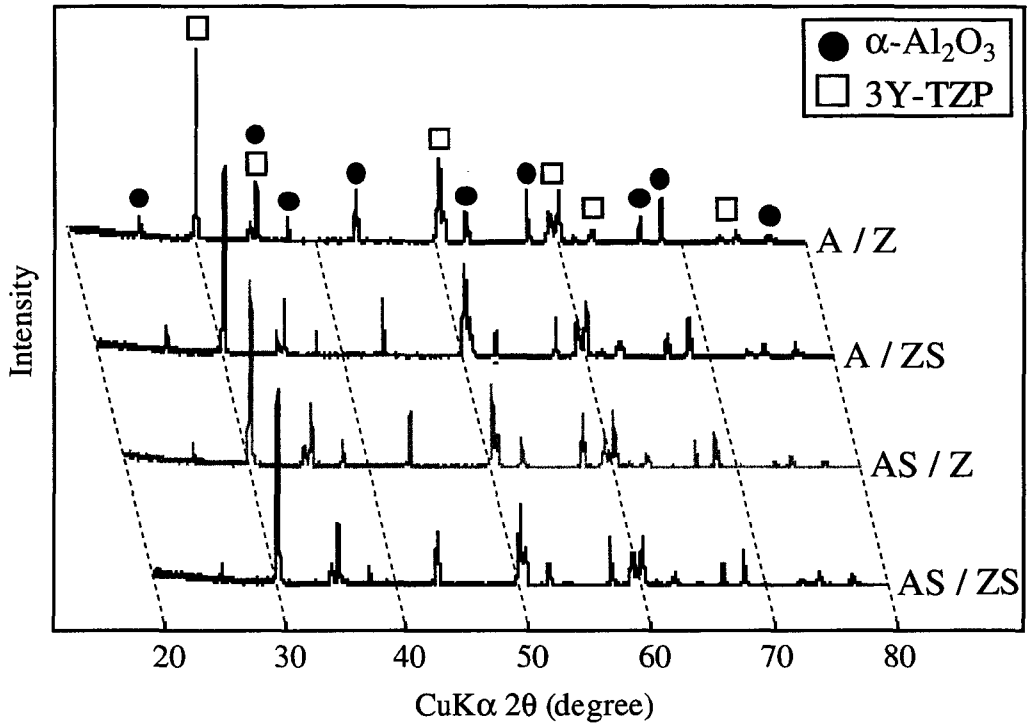

Fig. 5-1 X-ray diffraction patterns of multilayered nanocomposites.

5-3-2. Microstructural Observation

Existence of defects such as a channel cracks, micro cracks and debonding engenders residual stress relaxation. Therefore, it is necessary to confirm the absence of these defects

by microstructural observation of fabricated composites. Optical microscopic observation of the polished cross section for all multilayered composites (A/Z, A/ZS, AS/Z, and AS/ZS) did not give any evidences of such kind of defects at layer boundaries or inside respective layers, as shown in Fig. 5-2. A high magnification SEM image of the layer boundary in A/Z composite is shown in Fig. 5-3. Figure 5-4 indicates a high-resolution TEM image between Al_2O_3 and 3Y-TZP grains located at the layer boundary of A/Z multilayered composites. Each layer boundary between Al_2O_3 and 3Y-TZP layer is jointed rigidly; and the boundary fracture is not evident.

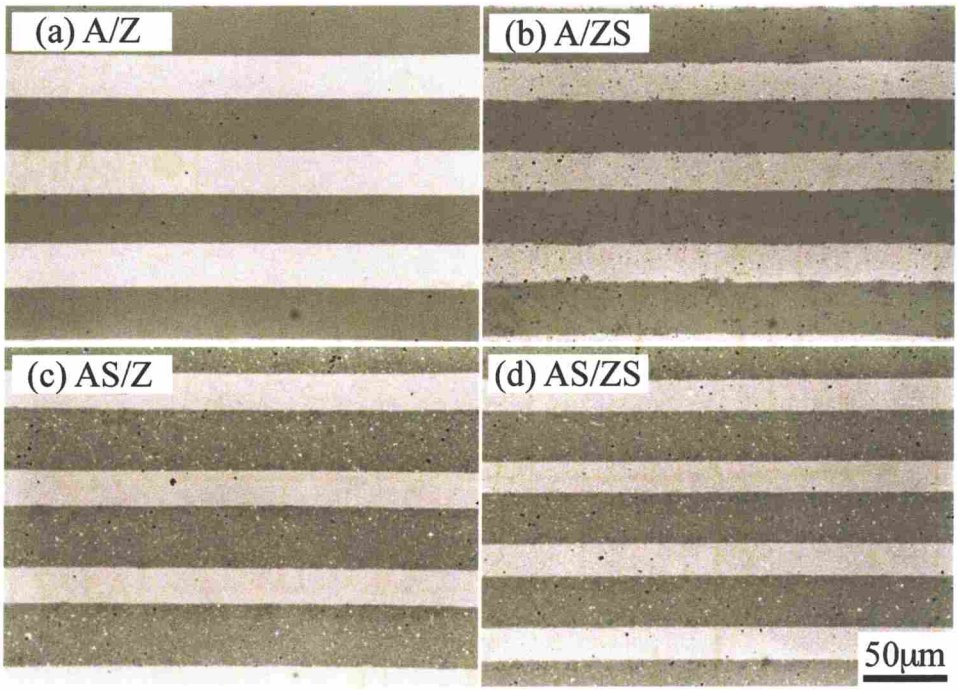

Fig. 5-2 Optical microscopic images of cross sections of (a) A/Z, (b) A/ZS, (c) AS/Z, and (d) AS/ZS multilayered composites. White and dark layers are corresponding to Al_2O_3-based and 3Y-TZP-based layers, respectively.

On the other hand, a chemical reaction to a glass phase at the interfaces gives a chance of relaxation of residual stress and because of the glass phase produces sliding of grain boundaries in a lower temperature. From Fig. 5-4, it was found that Al_2O_3 and 3Y-TZP grains are jointed directly without any obvious glass phase or reaction phase. Absence of a reaction phase is also confirmed by XRD analysis (see Fig. 5-1) for all multilayered composites.

Therefore, it was verified that relaxation of the residual stress caused by formation of defects and reaction phases did not occur in present composites.

TEM image of AS/ZS, in which nano-sized SiC was dispersed, is shown in Fig. 5-5. The diameter of the dispersed SiC particles was from tens to hundreds of nanometer.

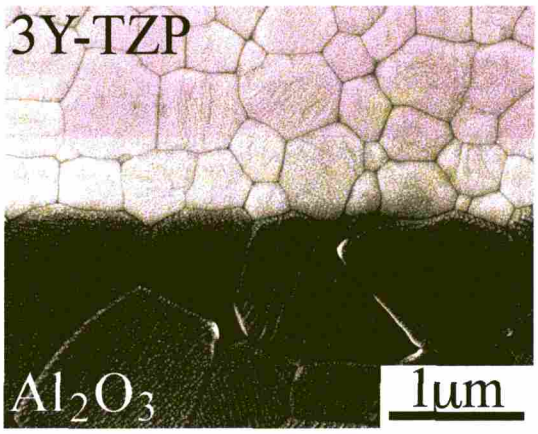

Fig. 5-3 SEM image of the layer boundary for the thermally etched A/Z multilayered composite; black and white layers indicate Al_2O_3 and 3Y-TZP layers, respectively.

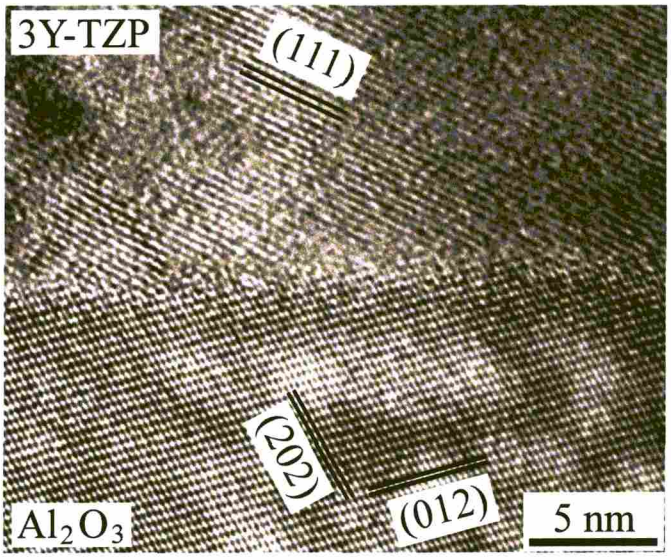

Fig. 5-4 HR-TEM image at the Al_2O_3-3Y-TZP interface near the layer boundary of A/Z multilayered composite.

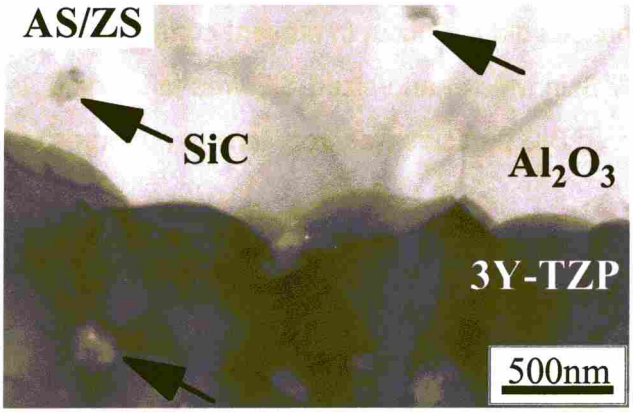

Fig. 5-5 TEM image of the layer boundary of AS/ZS multilayered nanocomposite, in which nano-sized SiC is dispersed in both layers.

5-3-3. Layer Thickness and Density

Layer thickness of each multilayered composite was measured by optical microscopic observation. Typical thickness of A and AS in sintered composites was 31 and 36 μm, respectively. It is considered that their different thickness is caused by both prevention of densification of Al_2O_3 by SiC dispersion (i.e., decrease of sinterability) and different thickness of each starting greensheets. On the other hand, typical thickness of Z and ZS layers was almost identical, 24 and 22 μm, respectively. This fact indicates that 3Y-TZP could be fully densified by pressureless sintering, even though SiC was dispersed. Thickness of the A or AS layer is thicker than that of Z or ZS layer because of different powder contents of each greensheets (i.e., solid loading in the slurry). Also, due to homogeneous thickness of greensheets, deviation in layer thickness of each composite was sufficiently small: 2~3 μm. Measured thickness was used for calculation of theoretical density and residual stress.

The A/Z multilayered composite indicates the highest relative density of ~99.5%; SiC dispersed composites (A/ZS, AS/Z and AS/ZS) indicated slightly lower density than that of the A/Z composite. Especially, the AS/ZS composite containing SiC within both Al_2O_3 and 3Y-TZP layers indicated the lowest relative density of 96.5%. However, we inferred that the residual-stress relaxation is negligible since density degradation is sufficiently low.

5-4. Macroscopic Residual Stress

5-4-1. Calculation of Macroscopic Residual Stress

To calculate macroscopic residual stress value, first, Young's moduli (E), Poisson's ratio (v), and CTE values (α) of layers such as AS and ZS in multilayered composites was estimated by the rule of mixture. In particle-dispersed composite materials, the CTE value ($\alpha_{comp.}$) of composite materials was estimated by Kerner's equation as [1]

$$\alpha_{comp.} = \alpha_m + x(\alpha_p - \alpha_m)\frac{K_m(3K_p + 4G_m)^2 + (K_p - K_m)(16G_m^2 + 12G_mK_p)}{(4G_m + 3K_p)[4xG_m(K_p - K_m) + 3K_mK_p + 4G_mK_m]}, \quad \text{(Eq. 5-1)}$$

where K and G correspond to bulk modulus and rigidity of materials and x is a volume fraction of dispersion (x = 0.05 for the present case). Subscripts m and p denote matrix and dispersion, respectively. Also, Young's modulus and Poisson's ratio of composite materials can be estimated from the relationship among Young's modulus, Poisson's ratio, bulk modulus, and rigidity, as follows [2]:

$$E = \frac{9KG}{3K + G} \quad \text{(Eq. 5-2)}$$

$$v = \frac{3K - 2G}{2(3K + G)}. \quad \text{(Eq. 5-3)}$$

Here, bulk modulus ($K_{comp.}$) and rigidity ($G_{comp.}$) of composite materials are estimated from the following equations [2].

$$K_{comp.} = K_m + x\left[\frac{1}{K_p - K_m} + \frac{3(1-x)}{3K_m + 4G_m}\right]^{-1} \quad \text{(Eq. 5-4)}$$

$$G_{comp.} = G_m + x\left[\frac{1}{G_p - G_m} + \frac{6(K_m + 2G_m)(1-x)}{5G_m(3K_m + 4G_m)}\right]^{-1} \quad \text{(Eq. 5-5)}$$

Table 5-1 summarizes these calculated values of the CTE, Young's modulus, Poisson's ratio, bulk modulus, and rigidity for monolithic and SiC-dispersed materials. Characteristic values (E, v, and α) of AS and ZS are changed since SiC has a lower CTE value, a lower

Poisson's ratio and a higher Young's modulus than those of A and Z. However, variation between a monolithic material and a composite material is small because the amount of SiC dispersion is as low as 5 vol%. On the other hand, the calculated CTE mismatch ($\Delta\alpha$) between each layer in SiC-dispersed multilayered composites is significantly different from an A/Z composite, even though the amount of SiC dispersion is small as 5 vol%, as is listed in Table 5-2. Therefore, we inferred that residual stress within multilayered composites can be controlled effectively by a small amount of SiC dispersion as well as a combination of layer materials.

Residual stress was generated within a multilayered composite according to the CTE mismatch between layer materials through the cooling process, as mentioned in the previous sections. In A layers with lower CTE, compressive stress was produced in the parallel direction to the layer, whereas tensile stress was produced in Z layer with higher CTE in same direction. The magnitude of these residual stresses is largely proportional to the CTE mismatch ($\Delta\alpha$) between A and Z, and a temperature difference (ΔT). It is also influenced by Young's modulus (E), Poisson's ratio (ν), number of layers (n), and thickness (d) according to the following formulas [3],

$$\sigma_A^{para} = \left[\frac{n_Z E_A E_Z d_Z}{(1-\nu_A) n_Z E_Z d_Z + (1-\nu_Z) n_A E_A d_A}\right] \Delta\alpha \times \Delta T \qquad \text{(Eq. 5-6)}$$

$$\sigma_Z^{para} = -\left[\frac{n_A E_A E_Z d_A}{(1-\nu_A) n_Z E_Z d_Z + (1-\nu_Z) n_A E_A d_A}\right] \Delta\alpha \times \Delta T, \qquad \text{(Eq. 5-7)}$$

where subscripts A and Z corresponds to the Al_2O_3 and 3Y-TZP layers. Furthermore σ_A^{para} and σ_Z^{para} denote residual stress of A and Z layers in the parallel direction. In this calculation, the number of layers (n_A and n_B) can be negligible since it is considered to be the same number ($n_A = n_B$); this is true because fabricated multilayered composites have sufficiently numerous layers. Temperature difference ΔT is regarded as the difference between room temperature and the temperature at which rigid chemical bonding and resultant well-bonded boundaries are formed. In other words, since residual stress corresponds to thermoelastic micromechanical stress, it must initially form below a certain temperature during the cooling process of sintering. This temperature is considered to be the temperature at which stress-relaxation by creep process during cooling is completed. That temperature, at which the creep mechanism can be nearly negligible, is regarded to be around 1000°C for typical

oxide ceramics. Therefore, ΔT of 1000°C (the difference between 1000°C and room temperature) was used in this study for residual stress calculation. The detailed discussion of the calculated stress values is presented in a later section (Table 5-4).

Table 5-1 Calculated characteristic values of monolithic materials, A and Z, and SiC-dispersed materials, AS and ZS

Property		Monolith			Composite	
		Al_2O_3	3Y-TZP	SiC	SiC dispersed Al_2O_3	SiC dispersed 3Y-TZP
Bulk modulus, K	(GPa)	(253)	(145)	(234)	(252)	(148)
Rigidity, G	(GPa)	(162)	(79)	(185)	(163)	(82)
CTE, α	($10^{-6}K^{-1}$)	8.10	10.60	4.45	(7.92)	(10.24)
Young's modulus, E	(GPa)	400	200	440	(402)	(208)
Poisson's ratio, ν	(-)	0.236	0.270	0.190	(0.234)	(0.267)

( ) ; calculated value

Table 5-2 Calculated CTE mismatch between the layer materials for various multilayered composites

Layer combination	A / Z	AS / Z	A / ZS	AS / ZS
CTE mismatch, $\Delta\alpha$ ($10^{-6}K^{-1}$)	2.50	2.68	2.14	2.32

5-4-2. Measurement of Macroscopic Residual Stress

Macroscopic residual stress was measured by XRD analysis using X-ray diffractometer with position sensitive proportional counter (PSPC) (PSPC-RSF, Rigaku Co., Ltd., Japan) on the polished cross section of multilayered nanocomposites[4-6]. Measurement was performed in two directions, parallel and perpendicular to the layer, to evaluate three-dimensional distribution of residual stress within multilayered composites [6]. The schematic drawing is illustrated in Fig. 5-6. The diameter of the measurement area (i.e., X-ray spot size) was a circle of approximately 2 mm. Diffraction angles (2θ) used in this measurement were 135.039° of (1 0 10) α-Al_2O_3 and 152.352° of (3 3 1) 3Y-TZP in Cr-Kα line [7,8].

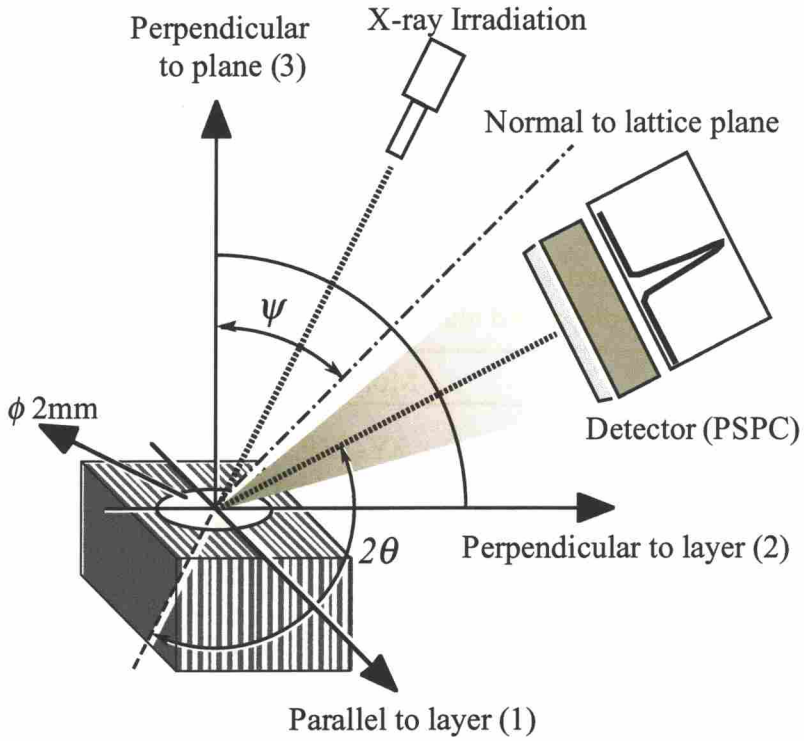

Fig. 5-6 Schematic drawing of the measurement of macroscopic residual stress by XRD analysis; the measurement was carried out in two directions of parallel (1) and perpendicular directions to the layer.

Residual stress is estimated by the $\sin^2\psi$ technique in this study. In this technique, residual stress ($\sigma_{X\text{-}ray}$) is given from both a stress constant (S) and a gradient of the 2θ-$\sin^2\psi$ plots (M), as [21]

$$\sigma = S \cdot M, \qquad \text{(Eq. 5-8)}$$

where the 2θ-$\sin^2\psi$ plots is obtained by plotting the 2θ angle of a target material on various X-ray irradiation angles (ψ, see Fig. 5-6). The stress constant (S) of each material was calculated using Young's modulus (E), Poisson's ratio (ν), and the diffraction angle without stain (i.e., the 2θ angle of the powder; $2\theta_0$) for each material by the following equation.

$$S = -\frac{E}{2(1+\nu)} \cdot \cot\theta_0 \cdot \frac{\pi}{180} \qquad \text{(Eq. 5-9)}$$

The gradient (*M*) of plots depends on a magnitude of residual stress; positive and negative values indicate compressive and tensile stress, respectively. Figure 5-7 show 2θ-$\sin^2\psi$ plots of the multilayered A/Z composite in two directions: parallel and perpendicular to the layers.

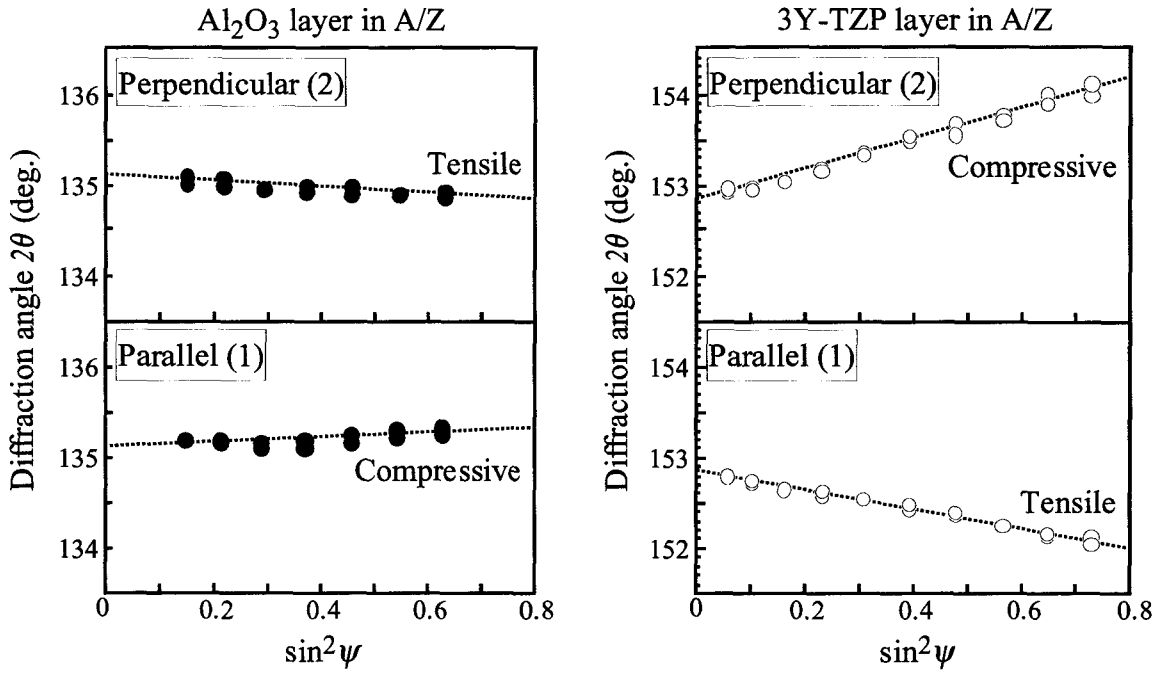

Fig. 5-7 The 2θ-$\sin^2\psi$ plots of Al_2O_3 and 3Y-TZP layers of A/Z; positive and negative gradients indicate compressive and tensile residual stress, respectively.

Because the gradient of the 2θ-$\sin^2\psi$ plots of the A layer is positive in the parallel direction and negative in the perpendicular direction, the compressive and tensile stress are inferred to exist in these directions, respectively. On the other hand, the tensile and compressive residual stress exists in parallel and perpendicular directions of the 3Y-TZP layer, respectively. The schematic drawing of the residual stress distribution is shown in Fig. 5-8.

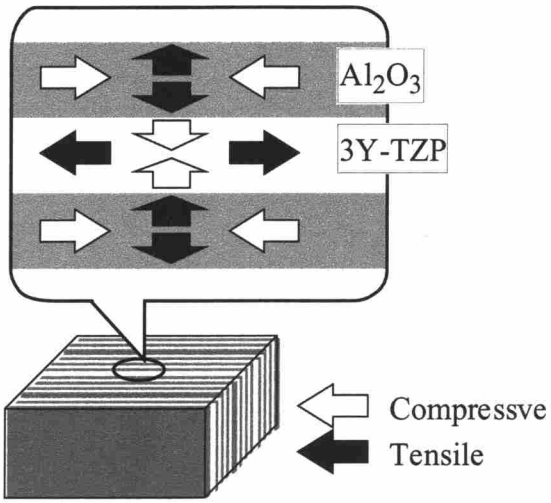

Fig. 5-8 Schematic drawing of the macroscopic residual stress distribution within multilayered composite; white arrow indicates a compressive stress, and black one indicates a tensile stress.

Generally, residual stress ($\sigma_{X\text{-}ray}$), which is directly obtained by the $\sin^2\psi$ technique, comprises the sum of both true residual stress ($\Delta\alpha$ induced thermal residual stress) and a machining stress. The latter is produced by machining such as a grinding. Measured residual stress ($\sigma_{X\text{-}ray}$) observed by the above-mentioned X-ray method can therefore be separated into true residual stress (σ) and machining stress (σ_{Mac}) using appropriate calculation [6]. Separated residual stress (σ) and machining stress (σ_{Mac}) for present composites are listed in Table 5-3. Because of machining such as a grinding produces a strain to surface grains, a change of d-spacing of grains introduced by this strain is different from the $\Delta\alpha$-associated residual stress. The measured surface was polished similar to look like a mirror face to reduce this machining stress. Therefore, the magnitude of machining stress is much lower than that of residual stress. The residual stress of the perpendicular direction to the measured plane (i.e., depth direction, σ_3 in Table 5-3) was closer to zero because of the stress release. This result conforms the fact that residual stress of the depth direction on the free surface is regarded to be zero [3].

Table 5-3 Three-dimensional stress distribution of raw stress ($\sigma_{X\text{-}ray}$), machining stress (σ_{Mac}) and macroscopic residual stress (σ) of A/Z multilayered composite.

Stress	Direction		Al_2O_3	3Y-TZP
Stress measured by X-ray	Parallel to layer (1)	$\sigma_{X\text{-}ray,1}$	- 286	409
	Perpendicular to layer (2)	$\sigma_{X\text{-}ray,2}$	357	- 511
	Perpendicular to plane (3)	$\sigma_{X\text{-}ray,3}$	- 12	58
Machining stress	Parallel to layer (1)	$\sigma_{Mac,1}$	20	
	Perpendicular to layer (2)	$\sigma_{Mac,2}$	- 25	
	Perpendicular to plane (3)	$\sigma_{Mac,3}$	19	
Residual stress	Parallel to layer (1)	σ_1	- 306	389
	Perpendicular to layer (2)	σ_2	383	- 486
	Perpendicular to plane (3)	σ_3	- 31	39

Subscript 1, 2 and 3 correspond to the stress directions as shown in Fig. 5-6. $\sigma_{X\text{-}ray}$ was directly observed from X-ray measurement. σ_{Mac} and σ were calculated according equations. [6]

Calculation indicates that AS/Z and A/ZS composites have the highest and lowest macroscopic residual stress, respectively. Therefore, precise measurement was carried out for AS/Z and A/ZS. For accurate measurement, X-ray stress measurement was performed three times; the result shows their average value. Residual stress (σ) of AS/Z and A/ZS composite can also be obtained by the procedures mentioned above; values are listed in Table 5-4 together with calculated residual stress of the parallel direction for A/Z, AS/Z and A/ZS composites.

All measured macroscopic residual stress values were slightly lower than calculated residual stress values. This difference may originate from measurement error and estimation of the parameter used in calculation. Especially, estimation of ΔT as 1000°C, which was used in the present calculation, seems to be approximate value of the substantial. However, differences between measured and calculated values in the A/Z composite are larger than for A/ZS and AS/Z composites. This fact implies that ΔT in the nanocomposite material is larger than the monolithic A/Z composite because the creep temperature in the nanocomposite is higher than the monolithic material.

Nevertheless, measured residual stress shows a similar tendency with calculated stress. Also, stress difference ($\Delta\sigma$), which corresponds to difference of residual stress between

compressive and tensile stress in each materials, increases with increased CTE mismatch. This fact indicates that observed macroscopic residual stress certainly depends on the CTE mismatch; calculations support this inference.

These results indicate that microstructure and layer design used in this experiment are advantageous for controlling residual stress in multilayered composites.

Table 5-4 Measured and calculated residual stress in the parallel direction for each layer of A/Z, AS/Z and A/ZS composites

Composite	CTE mismatch, $\Delta\alpha$ ($10^{-6}K^{-1}$)	Residual stress, σ (MPa)		Stress difference, $\Delta\sigma$ (MPa)
		A or AS	Z or ZS	
A / Z	2.50	-310 (-382)	410 (485)	720 (867)
A / ZS	2.14	-290 (-326)	384 (429)	674 (755)
AS / Z	2.68	-313 (-341)	510 (555)	823 (896)

( ) ; calculated value

Stress difference indicates the stress difference in each layer.
The stress value is an average of three times measurement.

5-5. Crack Propagation Behavior

5-5-1. Mechanism of Crack Deflection

Figure 5-9 indicates typical propagation behavior of a crack induced with an angle of 45° to the layer direction by the Vickers indentation test on a cross section of multilayered composite. The crack deflected near layer boundaries. It is concluded that this crack deflection resulted from directional residual stress produced by CTE mismatch between A and Z layers.

The mechanism of the crack deflection is schematically drawn in Fig. 5-10. When the crack is generated by indentation, stress (σ) extending the matrix is produced perpendicular to the crack propagation direction. Under existence of residual stress (σ_R) within layers, the crack is thus propagated by resultant stress ($\sigma + \sigma_R$). In the A layers, the direction of resultant stress is drawn perpendicular, and the crack propagation becomes parallel to the layers. Because an exactly opposed fact occurs in Z layers, the crack tends to propagate

perpendicular to the layers. Therefore, it could be inferred that cracks deflect to near layer boundaries between each layer. From this mechanism, it is considered that degree of the deflection depends on the residual stress. As the magnitude of residual stress increases, thus, an increasing of deflection angle at layer interface is expected.

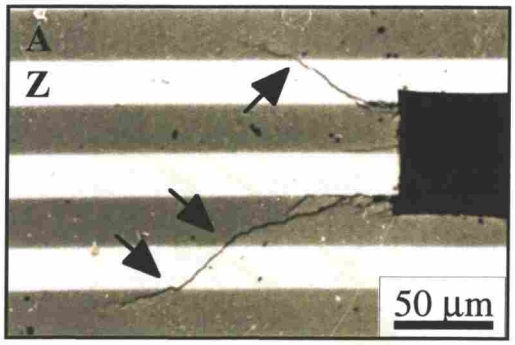

Fig. 5-9 The typical feature of the crack deflection induced by Vickers indentation test on the cross section of A/Z multilayered composite. The arrows indicate the crack deflections at the layer boudaries.

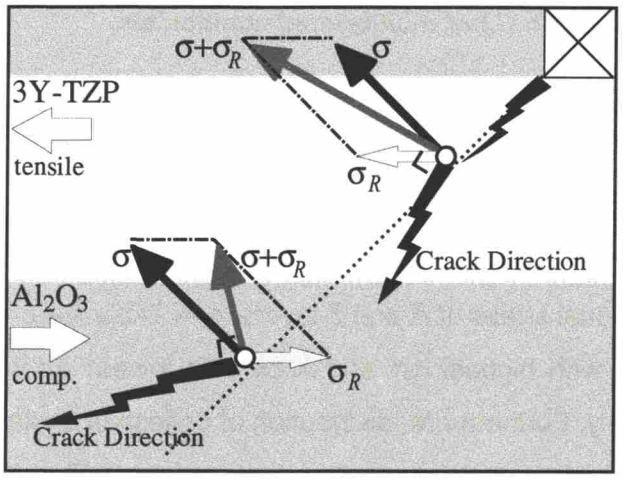

Fig. 5-10 The schematic illustration of stress directions and resultant crack deflection mechanism. σ and σ_R correspond to the stress extending a matrix and residual stress, respectively.

5-5-2. Crack Propagation Behavior

Crack propagation behavior was evaluated by analyzing the distribution of crack deflection, which was induced by Vickers indentation and formed as the illustrated geometry, which is shown in Fig. 5-11. In this study, effects of residual stress on crack deflection were investigated for A/Z, AS/Z and A/ZS composites, which have the middle, the highest and the lowest calculated residual stress, respectively.

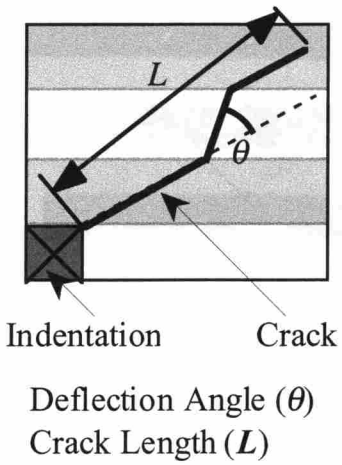

Fig. 5-11 Determination of crack deflection angle (θ) and crack length (L) of multilayered composites.

The crack feature and the distribution of the deflection angle of these composites are compared and shown in Fig. 5-12 with the stress difference ($\Delta\sigma$), which was calculated from the measured residual stress of A and Z layers (see Table 5-4). The average angles on deflection of A/Z, AS/Z with highest $\Delta\sigma$, and A/ZS with lowest $\Delta\sigma$ were approximately 24°, 26°, and 21°, respectively. Furthermore, distribution of deflection angle of the AS/Z composite is extended toward the higher angle range than those of the A/Z and A/ZS composites. The crack length of AS/Z was shortened, because the crack of AS/Z was propagated in zigzag shape due to the highest deflection angle. These results indicate that the increase of stress difference ($\Delta\sigma$) brings the increase of deflection angle at the layer boundaries. Consequently, the crack length was shortened by the increase of residual stress.

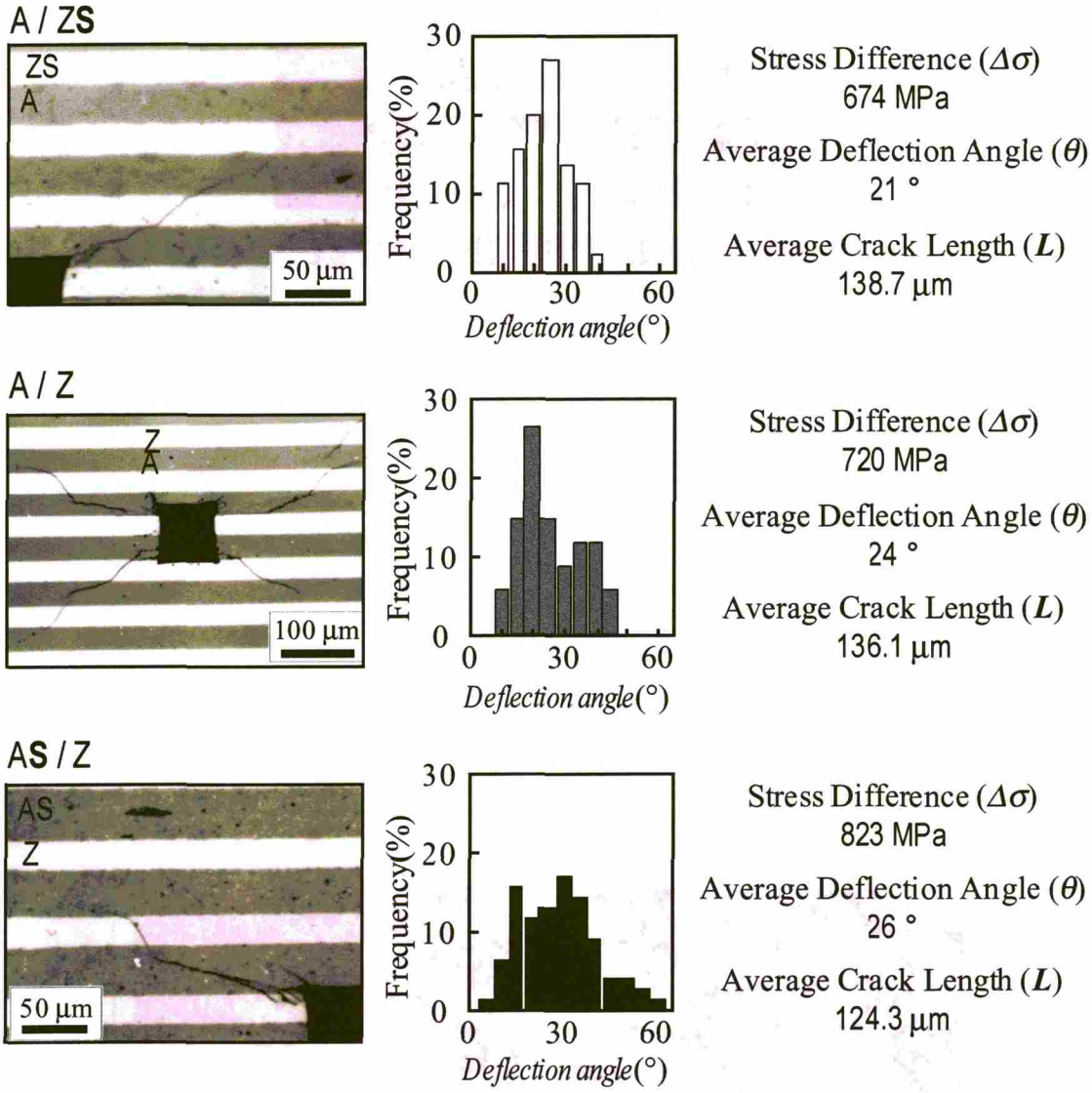

Fig. 5-12 Optical microscopic images of crack feature and corresponding distributions of deflection angle for A/ZS, A/Z and AS/Z multilayered composites. Dark and white layers indicate Al_2O_3-based and 3Y-TZP-based layers, respectively. Average values of deflection angle (θ) and crack length (L) are listed with stress difference ($\Delta\sigma$).

Figure 5-13 indicates the crack feature of AS/ZS, in which nano-sized SiC dispersed. In this composite, the crack propagation was strongly arrested by dispersed nano-sized SiC. The length of the crack was approximately 110 μm. This result implies that dispersed nano-sized particles are much effective to inhibit the crack propagation than the effect of residual stress (i.e., increase of crack deflection).

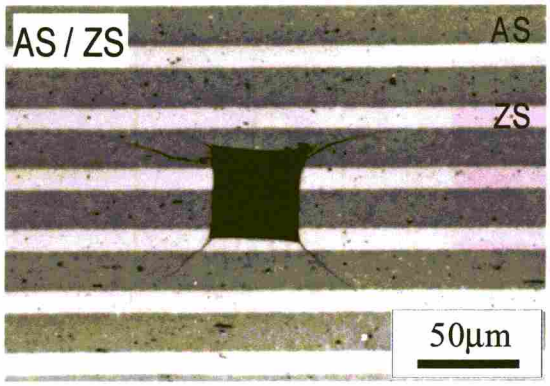

Fig. 5-13 Optical microscopic image of the crack feature of AS/ZS multilayered composite. Dark and white layers indicate Al_2O_3-based and 3Y-TZP-based layers.

5-5-3. Fracture Surface

Fracture surface of multilayered nanocomposite was observed by SEM. Figure 5-14 indicates the fracture surfaces of A, AS, Z, and ZS layers.

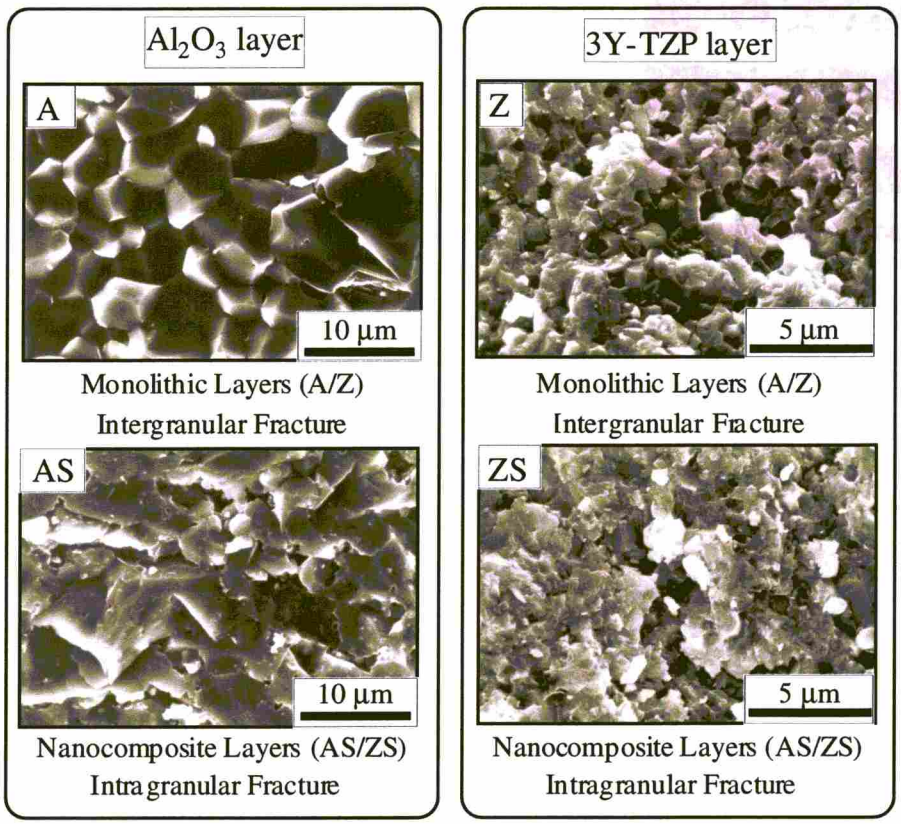

Fig. 5-14 SEM images of the fracture surface of monolithic layers (A and Z) and SiC-dispersed layers (AS and ZS).

In the monolithic layer (A and Z layers), the intergranular fracture was observed in both A and Z layers. This fact implies that the crack path propagates through the grain boundaries in monolithic layer. When the crack propagates the nanocomposite layer (AS and ZS layers), on the contrary, the crack was deflected by the dispersion, and then led to inside of grain, which has higher strength compared with grain boundary. Consequently, intragranular fracture was observed in the nanocomposite layers. This result verifies that crack propagation of the AS/ZS was strongly repressed by SiC dispersion.

5-6. Microscopic Stress Distribution

Macroscopic residual stress (i.e., directional residual stresses in multilayered composites) was mentioned in the previous part. However, actual stress distribution (i.e., microscopic distribution) within a layer is different from the macroscopic directional stress, strongly depending on a position. The magnitude is different between near a layer boundary and a center of layer [9].

As mentioned in section 5-4, SiC dispersion affects the macroscopic residual stress. Then, the effect of the SiC dispersion on the microscopic stress distribution was investigated by stress measurement for a small area within the layer. For such small area, it is difficult to obtain an accurate residual stress by XRD analysis, because the measurement area was not significantly large compared to ceramic grain size. Therefore, micro stress measurement was carried out for Z and ZS layers. These materials have much smaller grain size (approximately ~0.6 μm: 2h sintered at 1500°C) as compared with that of A (~1.2 μm: 2h sintered at 1500°C) and it is suitable to obtain an accurate measurement.

5-6-1. Evaluated Composites

Figure 5-15 indicates the appearance of the cross sections of A8Z8 and A8ZS8 multilayered nanocomposites. The thickness of Z and ZS layers were approximately 271 μm and 243 μm, respectively. It is considered that the thickness difference between these layers was caused mainly by the different shrinkage of 3Y-TZP layer due to SiC dispersion and partly by the deviation of the starting greensheets thickness.

In Z and ZS layers, channel cracks were observed across the layers. It is known that the channel crack is normally produced in the tensile layer [10,11]. According to the theoretical

consideration as was mentioned in the former section, Z or ZS layer was the tensile layer, resulted in the formation of channel crack in this study. Then, the stress measurement was carried out for the region where the channel crack and other defect did not exist (see Fig. 5-15).

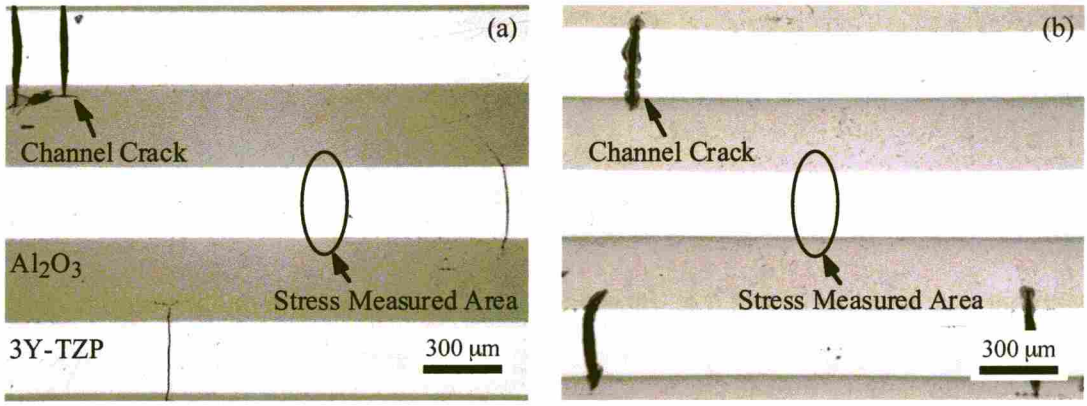

Fig. 5-15 The appearances of the cross section of (a) A8Z8 and (b) A8ZS8 multilayered nanocomposites observed by optical microscope. White and dark layers are 3Y-TZP-based and Al_2O_3 layers, respectively. Channel cracks are observed in Z and ZS layers.

5-6-2. Measurement of Microscopic Stress Distribution

Microscopic stress distribution of 3Y-TZP-based layer was measured by XRD analysis, because this method enabled to measure a stress of an arbitrary direction in a small area [5]. The diameter of the measurement area (i.e., X-ray spot size) was a circle of approximately 150 μm. The (3 3 1) reflection of 3Y-TZP was measured by using Cr-Kα radiation. The diffraction angle (2θ) was 152.352°. Stress values were estimated by the $\sin^2\psi$ technique for 3Y-TZP by using stress constant of 330 MPa/degree.

The microscopic stress distribution was measured for 3Y-TZP-based layers in middle part of the composites. Due to the thickness difference between Z (~271 μm) and ZS (~243 μm) layers, a normalized position (x: relative position within a layer) was used. The measurement was carried out for five spots (i.e., the center of the circles were 0, 0.25, 0.5, 0.75, and 1.0 in the normalized position) within the layer as shown in Fig. 5-16. Here, for the circle at the layer boundaries, the normalized position was regarded as a center of X-ray irradiated area (i.e., x = 0.1 and 0.9). Two directional residual stresses, parallel ($\sigma_{R//}$) and perpendicular ($\sigma_{R\perp}$) were measured in the each circle of the layers. The stress values for

each spots were obtained as an average value of 6 time measurements, and the values for two directions (i.e., parallel and perpendicular) were determined.

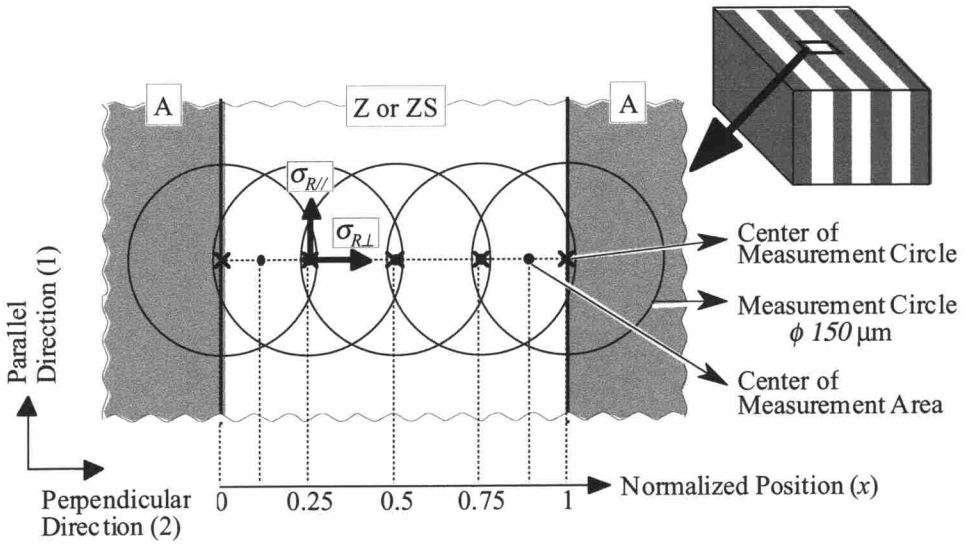

Fig. 5-16 The stress measured area and the normalized position (x) within Z and ZS layers on the multilayered composites. The circles a X-ray spot size of 150 μm in diameter. The arrows mean the measurement directions of parallel ($\sigma_{R//}$) and perpendicular ($\sigma_{R\perp}$) to thelayer.

5-6-3. Microscopic Stress Distribution

The observed stress distribution for two directional stress components (i.e., parallel and perpendicular directions to the layer) within Z and ZS layers is shown in Fig. 5-17.

In the parallel direction ($\sigma_{R//}$: see Fig. 5-17(a)), microscopic tensile stress was observed within the layer. The stress distribution of Z layer was parabolic shape, and has higher stress (i.e., stress concentration) near the layer boundaries and lower stress in the center of layer. The magnitude of the stress was approximately 220 to 260 MPa. By considering geometrical relation (see Fig. 5-16) between a spot size of X-ray irradiation (approximately 150 μm) and layer thickness (240 ~ 270 μm), the measured stress values, especially those of near the layer boundary, may be under-estimated because the value is obtained as an average among the irradiated area. Nevertheless, the stress distribution is considered to be certainly existed across in the Z layer, and it is deemed that layer boundary region might have higher stress level while the centers have lower value. On the other hand, an obvious

parabolic distribution could not be observed in the case of ZS layer, though the deviation was significantly large. And the stress level was slightly higher than that of the Z layer, approximately 300 MPa.

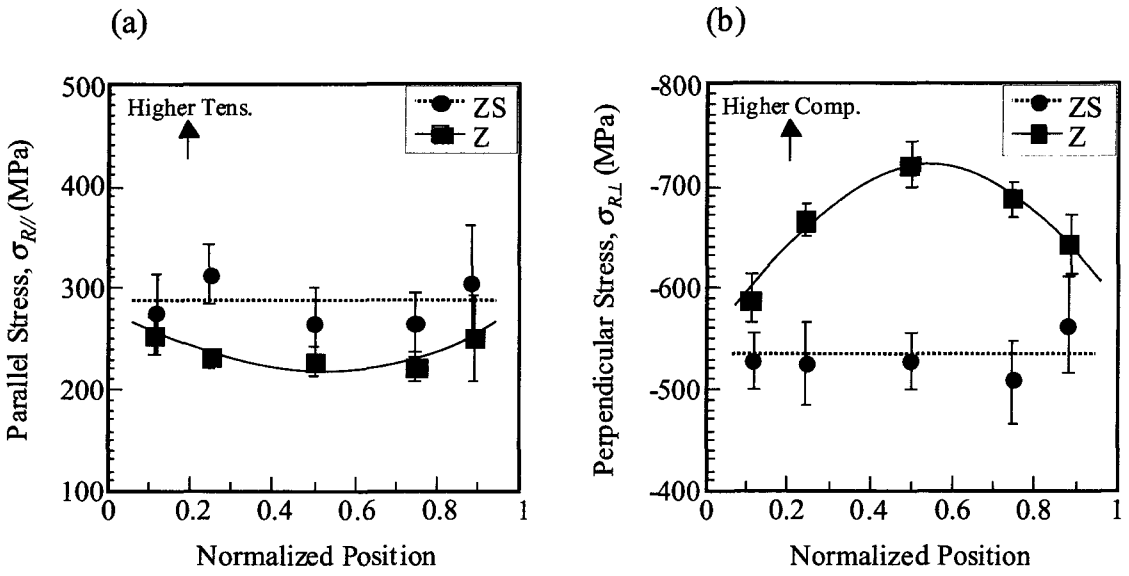

Fig. 5-17 Microscopic stress distribution within Z or ZS layers for (a) parallel ($\sigma_{R//}$) and (b) perpendicular ($\sigma_{R\perp}$) directions. The distribution of ZS layer are shifted to a tensile side rather than that of Z.

In the case of stress component perpendicular to the layers (i.e., $\sigma_{R\perp}$: see Fig. 5-17(b)), it was revealed that compressive residual stress existed within the Z and ZS layers. For Z layer, a parabolic distribution was clearly observed in the direction what was similar to the parallel direction. In the perpendicular direction, however, a maximum stress value of approximately 700 MPa was measured at the center of the layer, showing the stress concentration at the center region instead of the interface. On the other hand, the stress distribution across the ZS layer was almost independent of the position and the stress level was low of approximately -530 MPa as compared with that of the layer without SiC (Z layer).

Regardless the residual stress direction, it should be noted that two characteristic changes are taken place in micro residual stress development by SiC dispersion into 3Y-TZP layer, (1) flattening of the stress distribution, and (2) shift of the stress level (see Fig. 5-17).

By considering parallel direction to the layer, compressive and tensile stresses are

macroscopically generated in Al_2O_3 and 3Y-TZP layers, respectively. Practically, stress is asymptotically varied depending on the distance from layer boundary, and the highest tensile stress in 3Y-TZP layer is produced near the layer boundary. When SiC is dispersed into 3Y-TZP, macroscopic physical properties such as CTE and Young's modulus of ZS layer is varied according to the rule of mixture, and the tensile stress in ZS layer is resultantly decreased. The degradation of this tensile stress is more dominant near the layer boundary than that of layer center because of the asymptotical stress distribution, and hence the stress distribution within ZS layer might be flattened compared to that of in Z layer.

The other important characteristic of stress development, i.e. the above-mentioned stress level shift (2), is considered as follows. The stress level was overall increased for the parallel direction while it was decreased in the perpendicular direction as it was mentioned above. This fact meant that the stress level is systematically sifted to tensile side for both directions by nano-sized SiC dispersion into 3Y-TZP layer. It is known that macroscopic tensile stress was generated in a matrix phase when secondary particulate dispersion was incorporated into the matrix with low CTE value [12,13]. This might be the case for the present system; Dispersion of SiC into 3Y-TZP matrix would bring tensile stress to the matrix, because SiC has lower CTE than that of 3Y-TZP. By the theoretical calculation, the magnitude of tensile stress by this SiC dispersion could thus be estimated as approximately as 70 MPa [14] which might contribute to the systematic shift of stress level in the case of A/ZS system.

Furthermore, the absolute stress value of perpendicular direction (-700 MPa for Z, and -530 MPa for ZS) was higher than that of the parallel diction (220 MPa for Z, and 300 MPa for ZS). This fact implies that the perpendicular stress to the layers within a multilayered composite should be more effective to several mechanical and physical phenomenons as well as the stress distribution.

In multilayered composites, a crack propagation behavior is usually discussed in relation with residual stresses formed parallel to layers. When crack propagates aslant to the layers, crack deflection was usually observed at the layer boundaries. This deflection was exactly derived from the parallel stress within the layers. Compressive (i.e., A in the present case) and tensile (i.e., Z or ZS) stresses bend the crack propagation to the parallel and perpendicular directions, respectively. Therefore, the crack propagation behavior in each layer is different in each layer, and as a result, the crack is deflected at the layer boundaries.

In this investigation, however, it was realized that the absolute value of perpendicular stress in 3Y-TZP layers was higher than that in the case of parallel stress. This strongly

implies that the perpendicular stress contribute to the crack deflection behavior more than that of parallel direction. The perpendicular tensile stress (i.e., A) promotes the bending of the crack propagation to the layer direction. And, perpendicular compressive stress (i.e., Z or ZS) inhibits the bending to the layer direction. These crack deflection behaviors are as same as the contribution of parallel stress. It can be thus concluded that the crack deflection is governed by both parallel and perpendicular stress.

5-7. Summary

Multilayered nanocomposites were evaluated in relation to the microstructure, the macroscopic residual stress, the microscopic stress distribution, and the mechanical properties.

Microstructural observations indicated no reaction phases and defects such as delamination and debonding in A/Z, A/ZS, AS/Z, and AS/ZS. Therefore, it was concluded that residual stress relaxation by defects and reaction phases is negligible for the obtained composites.

Macroscopic residual stress was measured by XRD analysis on the cross section of multilayered nanocomposites. The stress measurement revealed that the residual stress within multilayered nanocomposites can be controlled by SiC dispersion and resultant control of physical properties such as elastic constant, CTE, et cetera.

The increase of the magnitude of residual stress brought the increase of deflection angle, and then the decrease of the crack length. This fact implies that control of the residual stress is important on the crack propagation behavior. In addition, it was revealed that SiC dispersion strongly repressed the crack propagation.

In monolithic layer (i.e., Z layer in the A8Z8), the microscopic stress distribution had parabolic shape (i.e., stress concentration) in parallel and perpendicular directions. On the other hand, in the nanocomposite layer (i.e., ZS layer in the A8ZS8), the stress distribution was different from the monolithic Z layer. The result indicates that the microscopic distribution can be controlled by the SiC dispersion.

References

[1] E. H. Kerner, *Proc. Phys. Soc.*, **B69**, 808 (1956).

[2] Z. Hashin, and S. Shtrikman, *J. Mech. Phys. Solids*, **11**, 127 (1963).

[3] T. Chartier, D. Merle, and J.L. Besson, *J. Eur. Ceram. Soc.*, **15**, 101 (1995).

[4] B.D. Cullity, in *Elements of X-ray Diffraction*, Edited by M. Cohen, Addison-Weslay Pub. Co., pp. 447-78, 1978.

[5] T. Goto, and S. Ohya, *J. Soc. Mat. Sci., Japan*, **47**, 1188 (1998).

[6] K. Tanaka, and Y. Akiniwa, *J. Soc. Mat. Sci., Japan*, **47**, 1301 (1998).

[7] K. Suzuki, and K. Tanaka, *J. Soc. Mat. Sci., Japan*, **37**, 586 (1988).

[8] K. Suzuki, and K. Kusaka, *J. Soc. Mat. Sci., Japan*, **48**, 308 (1999).

[9] H. Tomaszewski, J. Strzeszewski, and W. Gebicki, *J. Eur. Ceram. Soc.*, **19**, 255 (1999).

[10] P.Z. Cai, D.J. Green, and G.L. Messing, *J. Am. Ceram. Soc.*, **80**, 1929 (1997).

[11] C. Hillman, Z. Suo, and F.F. Lange, *J. Am. Ceram. Soc.*, **79**, 2127 (1996).

[12] T. Ohji, Y.K. Jeong, Y.H. Choa, and K. Niihara, *J. Am. Ceram. Soc.*, **81**, 1453 (1998).

[13] M. Taya, S. Hayashi, A.S. Kobayashi, and H.S. Yoon, *J. Am. Ceram. Soc.*, **73**, 1382 (1990)

[14] N. Bamba, Y.H. Choa, T. Sekino, and K. Niihara, *J. Eur. Ceram. Soc.*, in press.

CHAPTER 6

2-dimensional Dispersed Nanocomposites

6-1. Introduction

3Y-TZP-based 2-dimensional dispersed nanocomposites were designed in Chapter 2 in order to incorporate the directional residual stress into traditional nanocomposite materials, and fabricated in Chapter 3. The 3Y-TZP-based 2-dimensional dispersed nanocomposites are comprised by the stacking of monolithic 3Y-TZP (Z) layer and 3Y-TZP/SiC (ZS) nanocomposite layer. Therefore, in this composite, residual stress was generated from the multilayered structure as well as popular multilayered composites [1]. Then, the induced residual stress was measured by XRD analysis on the top surface of the composite [2-4]. According to the results of Chapter 5, it was revealed that residual stress within the multilayered composites affects crack propagation behavior. In this chapter, therefore, crack propagation behavior of the 2-dimensional dispersed nanocomposites was investigated by Vickers indentation test. In addition, the induced residual stress is thought to deform the crystalline of the matrix material. Then, the effect of the strain was investigated on the thermal properties by laser flash method.

6-2. Experimental Procedure

The 2-dimensional dispersed nanocomposites comprising of nanocomposite layer and monolithic layer were fabricated by stacking Z and ZS greensheets. The combination and number of each greensheet are listed in Table 3-4. Hereafter, the surface nanocomposite, consistsed of nanocomposite surface layers with monolith inner layers, is denoted as N.Surf.(*n*), and the surface monolith, consisted of monolith surface layers with nanocomposite inner layers, is as M.Surf.(*n*). The variable *n* indicates the number of greensheets stacked to form one surface layer. In addition, a bulky monolithic 3Y-TZP

obtained by stacking only Z greensheets, and a bulky traditional 3Y-TZP/SiC nanocomposite that comprised only ZS greensheets are denoted as M.Bulk and N.Bulk, respectively. Also hereafter, material with nanocomposite layer is collectivity denoted as N (i.e., N.Surf. and N.Bulk), and M (i.e., M.Surf. and M.Bulk) for material with monolith layer. Roughly, 34~35 greensheets are stacked to obtain composite materials with 1mm thickness. After thermocompressive pressing and twice calcinations, the calcinated composites were pressureless sintered at 1500°C for 2 h under an Ar atmosphere to prevent SiC oxidation. Refer to Chapter 3 for the details of the fabrication method.

Sintered multilayered composites were with a dimension of 12 mm in diameter and 1.2 mm in thickness. For the measurement of surface stress by X-ray diffraction (XRD), all materials were grinded and mirror polished to reduce the surface roughness. These machining process were carried out for each side (i.e., top and bottom surface) of the material. The machining depth was approximately 0.1 mm (~ three layer thickness). After the machining process, the thickness of the composites was 1 mm; the schematic drawing of the multilayered composite is illustrated in Fig. 6-1(a).

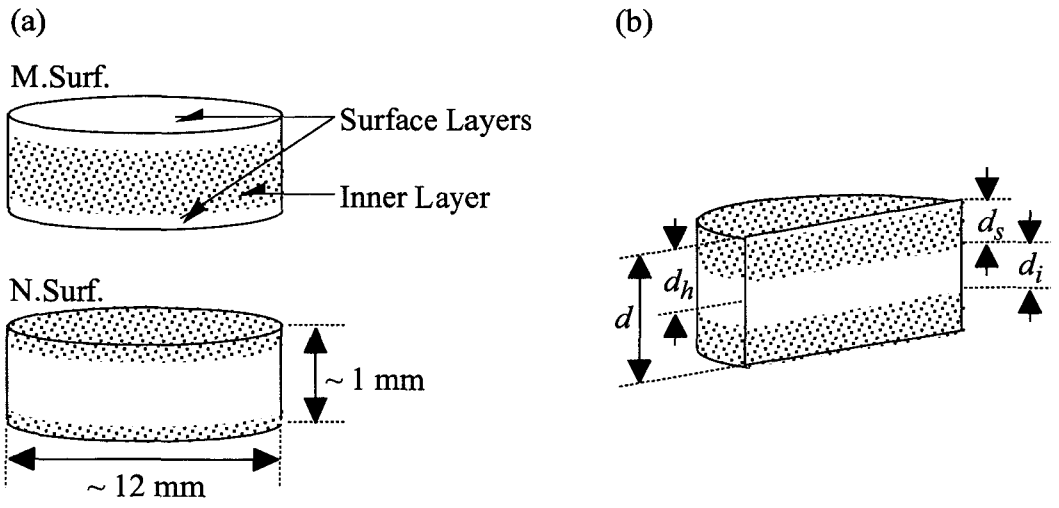

Fig. 6-1 (a) Schematic drawings of surface monolith (M.Surf.) and surface nanocomposite (N.Surf.), and (b) diagram of several thickness of 2-dimensional dispersed nanocomposite.

6-3. Microstructure

6-3-1. Microstructural Observation

Optical microscopic observation of a polished cross section for the fabricated 2-dimensional dispersed nanocomposites indicated the absence of defect such as debonding, channel crack and microcrack. A high contrast image of the cross section of M.Surf.(14) is shown in Fig. 6-2 as a typical appearance of 2-dimensional dispersed nanocomposite. Layer boundaries between monolith and nanocomposite layer were bonded rigidly and the defects at layer interfaces were not observed for a stacking condition of 5~25 greensheets.

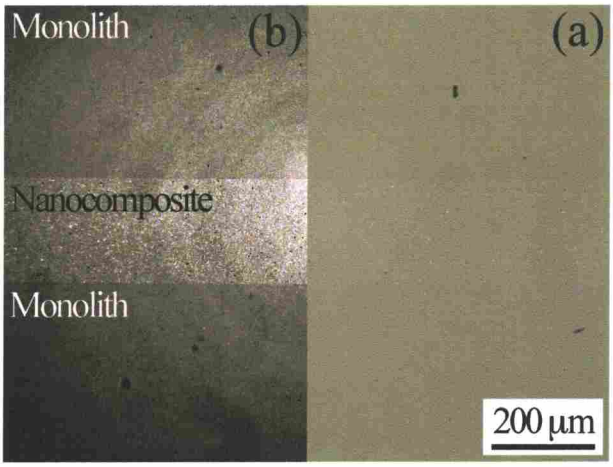

Fig. 6-2 Optical microscopic image of the cross section of M.Surf.(14); (a) original appearance and (b) high contrasted image. In the right image (a), nanocomposite layer was not observed clearly, bcause each layer is consisted of 3Y-TZP-based material. Black and gray layers indicate monolithic 3Y-TZP and 3Y-TZP/SiC nanocomposite layers in the left image (b), respectively.

Considering that defects generally relax residual stress within composites, it can be regarded that the stress relaxation was not caused in the fabricated materials including 2-dimensional dispersed nanocomposites. No relaxation of residual stress (i.e., rigid bonding at layer boundaries and inside of each layer, and no defect) implies that the fabrication method is suitable to realize the control of surface stress as a subject of this study.

6-3-2. Thickness Ratio

Total thickness and thickness of surface and inner layers were measured (see Fig. 6-1(b)) by optical microscopic observation, and are listed in Table 6-1. In this study, in order to estimate residual stress in the surface layer, thickness ratio (r_d) is defined as

$$r_d = d_s / d_h \quad \text{(Eq. 6-1)}$$

$$d_h = d/2 \quad \text{(Eq. 6-2)}$$

where d_s and d correspond to the thickness of surface layer and the total thickness (d = ~1 mm) of 2-dimensional dispersed nanocomposite, respectively. Small deviation in the thickness ratio was caused mainly by the machining process.

Table 6-1 Average thickness of surface and inner layers and calculated thickness ratio

Sample	Average Thickness (mm)			Thickness Ratio, r_d
	Total, d	Surface, d_s	Inner, d_i	
M.Bulk	1.017			(1.000)
N.Bulk	1.017			(1.000)
M.Surf.(5)	0.994	0.087	0.821	0.174
M.Surf.(7)	0.995	0.167	0.660	0.336
M.Surf.(10)	0.989	0.248	0.492	0.502
M.Surf.(12)	0.975	0.324	0.327	0.665
M.Surf.(14)	0.966	0.386	0.193	0.800
N.Surf.(5)	0.984	0.109	0.765	0.222
N.Surf.(7)	0.983	0.177	0.628	0.361
N.Surf.(10)	0.985	0.250	0.485	0.508
N.Surf.(12)	0.983	0.338	0.306	0.688
N.Surf.(14)	0.987	0.401	0.186	0.812

6-3-3. Density

Density of machined composites was measured by Archimedes principle. Theoretical density of bulky materials (N.Bulk and M.Bulk) was calculated from the theoretical densities of both 3Y-TZP (6.08 g/cm^3) and SiC (3.21 g/cm^3). For 2-dimensional dispersed nanocomposites (N.Surf. and M.Surf.), the theoretical density was estimated from their thickness ratio and theoretical density of Z and ZS, and used for the calculation of relative density. The

calculated theoretical density, the measured bulk density and the relative density of each composite material are listed in Table 6-2.

Even though SiC was dispersed into nanocomposite layer, the enough densification (i.e., above 98.8 % of relative density) was achieved for these materials. Good sinterability between 3Y-TZP & SiC with a small dispersion (5 vol%) brought the full densification. The 2-dimensional dispersed nanocomposites of both N.Surf. and M.Surf. indicates sufficient high relative density. This fact verifies that no defects exist in these 2-dimensional dispersed nanocomposites.

Table 6-2 Theoretical, bulk and relative density.

Sample	Theoretical Density (g/cm^3)	Bulk Density (g/cm^3)	Relative Density (%)
M.Bulk	6.08	6.06	99.7
N.Bulk	5.94	5.86	98.8
M.Surf.(5)	5.96	5.92	99.2
M.Surf.(7)	5.98	5.97	99.7
M.Surf.(10)	6.01	5.99	99.7
M.Surf.(12)	6.03	6.02	99.8
M.Surf.(14)	6.05	6.05	100.0
N.Surf.(5)	6.05	6.03	99.7
N.Surf.(7)	6.03	6.01	99.7
N.Surf.(10)	6.01	5.98	99.6
N.Surf.(12)	5.98	5.95	99.4
N.Surf.(14)	5.96	5.93	99.4

6-4. Surface Stress

6-4-1. Surface Stress Measurement

Surface stress of each composite material was measured by using XRD analysis [2-4]. In this study, the stress measurement was carried out by XRD equipment with a position-sensitive proportional counter (PSPC) (PSPC-RSF, Rigaku Co., Ltd., Japan) on a polished surface of the materials. The measurement area (i.e., X-ray spot size) was a circle of approximately 4 mm in diameter, as shown in Fig. 6-3. Diffraction angle (2θ) used in this

measurement was 152.352° of (3 3 1) 3Y-TZP in Cr-Kα line. In this study, surface stress was estimated by $\sin^2\psi$ technique. In this technique, surface stress ($\sigma_{mea.}$) is obtained from a stress constant (S) and a gradient (M) of the 2θ-$\sin^2\psi$ plots, using the following equation [2-4],

$$\sigma = S \cdot M, \qquad \text{(Eq. 6-3)}$$

where the 2θ-$\sin^2\psi$ plots are obtained by plotting the 2θ angle of a target material on various X-ray irradiation angles (ψ, see Fig. 6-3).

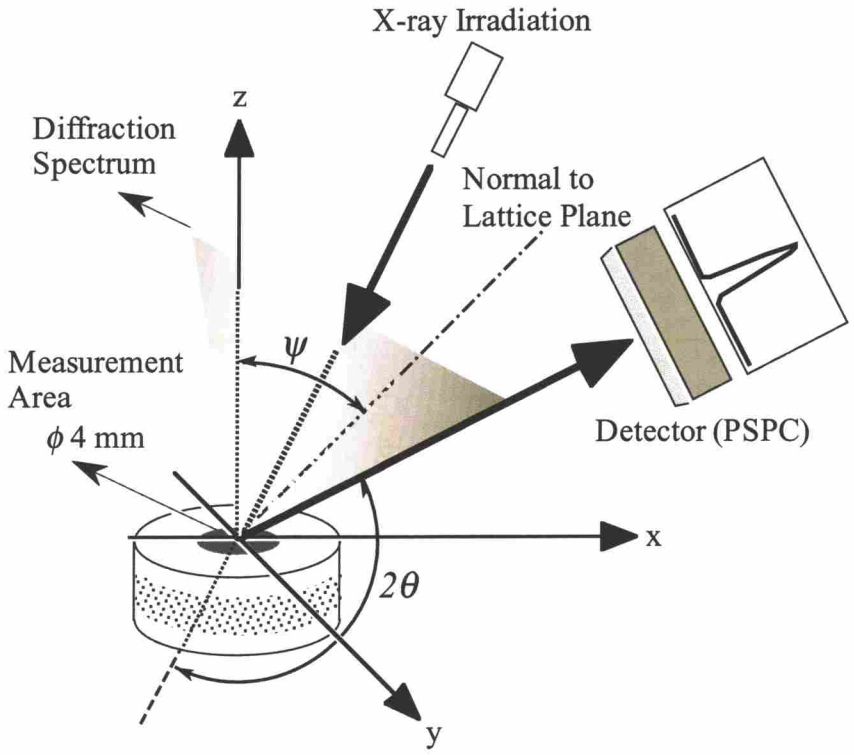

Table 6-3 Schematic drawing of residual stress measurement by XRD analysis; the measurement was carried out in the center on the top surface, and the area was a circle of 4 mm in diameter.

The stress constant (S) of a material was calculated using their Young's modulus (E), Poisson's ratio (ν), and the diffraction angle without stain (i.e., the 2θ angle of Z powder; in measurement $2\theta_0$ = 153.01°) by the following equation [2-4].

$$S = -\frac{E}{2(1+\nu)} \cdot \cot\left(\theta_0 \cdot \frac{\pi}{180}\right) \qquad \text{(Eq. 6-4)}$$

The gradient (*M*) of plots depends on the magnitude of surface stress; positive and negative values indicate compressive and tensile stress, respectively. The calculated stress constant (*S*) for Z was approximately 330 MPa/degree.

Figure 6-4(a) shows 2θ-$\sin^2\psi$ plots of Z on the surface of N.Surf.(5) with thin surface layer and N.Surf.(14) with thick surface layer. Similarly, for the M.Surf.(5) and M.Surf.(14) are shown in Fig. 6-4(b). Because the N.Surf.(5) has a positive gradient of the 2θ-$\sin^2\psi$ plots, the surface has significant compressive stress. On the other hand, it is inferred that M.Surf.(5) has significant tensile stress from the negative gradient. And, the surface stresses of N.Surf.(14) and M.Surf.(14) with thick surface layers are estimated as almost 0 MPa due to the small gradient. These facts indicate that the surface stress depends on the thickness of the surface layer; thin surface layer brings significant surface stress compared with the thick surface layer which has low surface stress.

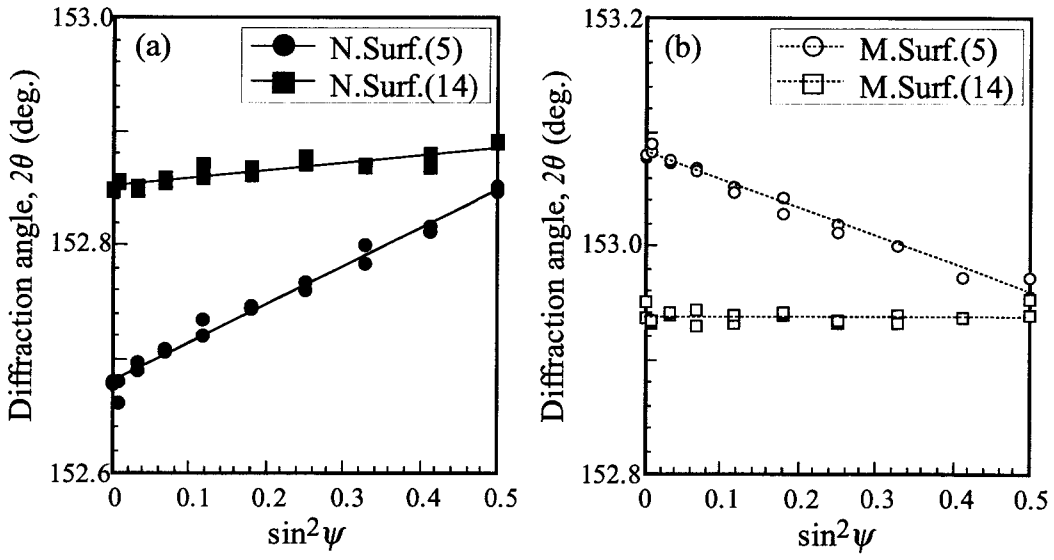

Fig. 6-4 The 2θ-$\sin^2\psi$ plots of (a) N.Surf. and (b) M.Surf. for 2-dimensional dispersed nanocomposite with thin surface layer (5) and thick surface layer (14), respectively. Positive and negative gradient (*M*) indicate compressive and tensile stress, respectively. And the higher stress brings an increase of the gradient (*M*).

Measured surface stress ($\sigma_{mea.}$) of each material is shown in Fig. 6-5 as a function of their thickness ratio (r_d). The magnitude of the surface stress is increased with the decrease of the thickness ratio. In addition, for bulky materials of N.Bulk and M.Bulk, the measured surface stresses were approximately 0 and -30 MPa, respectively. The magnitude of surface stresses for N could be controlled in the region from 0 to -130 MPa by variation of the thickness ratio. On the other hand, the magnitude was in the region from -30 to +100 MPa for M.

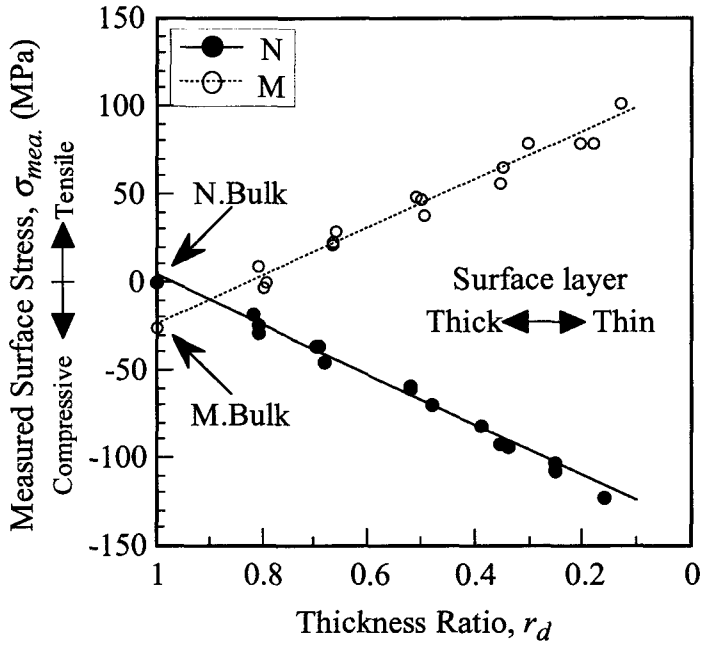

Fig. 6-5 Measured surface stress ($\sigma_{mea.}$) as a function of thickness ratio (r_d) for N and M. The 2-dimensional dispersed nanocomposite with thin surface layer has higher surface stress, and the change of the magnitude is linear.

6-4-2. Calculation of Residual Stress

(1) Residual Stress due to Multilayered Structure

In multilayered composites, residual stress is caused mainly by the CTE mismatch between layer materials through the cooling process. It is reported that the residual stress of each layer material can be calculated as a macroscopic average value within each layer [1].

The magnitude of the residual stress ($\sigma_{cal.(L)}$) of the surface layer along the layer direction can be calculated from the following formula [1],

$$\sigma_{cal.(L)} = \left[\frac{E_s E_i d_i}{(1-\nu_s)E_i d_i + 2(1-\nu_i)E_s d_s}\right]\Delta\alpha \times \Delta T$$
$$= \left[\frac{E_s E_i (1-r_d)}{(1-\nu_s)E_i(1-r_d) + (1-\nu_i)E_s r_d}\right]\Delta\alpha \times \Delta T \qquad \text{(Eq. 6-5)}$$

where subscript *s* and *i* denote surface and inner layers, and *E*, *v* and *d* correspond to Young's modulus, Poisson's ratio and layer thickness of each layer material, respectively. Temperature difference, ΔT is regarded as the difference between room temperature and the temperature at which creep of 3Y-TZP can be neglected absolutely. In this calculation, the ΔT is estimated as 1000°C [5]. $\Delta\alpha$ denotes the CTE mismatch between surface and inner layer materials as $\Delta\alpha = \alpha_s - \alpha_i$.

According to rule of mixture, characteristic values such as *E*, *v*, and α of particle dispersed composites (i.e., ZS nanocomposite layer in the present work) can be estimated [6,7]. The CTE value ($\alpha_{comp.}$) of composite material is estimated by the following Kerner's equation [6]

$$\alpha_{comp.} = \alpha_m + x(\alpha_p - \alpha_m)\frac{K_m(3K_p + 4G_m)^2 + (K_p - K_m)(16G_m^2 + 12G_m K_p)}{(4G_m + 3K_p)[4xG_m(K_p - K_m) + 3K_m K_p + 4G_m K_m]} \qquad \text{(Eq. 6-6)}$$

where *K* and *G* correspond to bulk modulus and rigidity of materials and *x* is a volume fraction of dispersion (*x* = 0.05 for the present case). Subscript *m* and *p* denote matrix and dispersed particle, respectively. Here, bulk modulus ($K_{comp.}$) and rigidity ($G_{comp.}$) of composite material are estimated from the following equations [7].

$$K_{comp.} = K_m + x\left[\frac{1}{K_p - K_m} + \frac{3(1-x)}{3K_m + 4G_m}\right]^{-1} \qquad \text{(Eq. 6-7)}$$

$$G_{comp.} = G_m + x\left[\frac{1}{G_p - G_m} + \frac{6(K_m + 2G_m)(1-x)}{5G_m(3K_m + 4G_m)}\right]^{-1} \qquad \text{(Eq. 6-8)}$$

Young's modulus ($E_{comp.}$) and Poisson's ratio ($\nu_{comp.}$) of composite material can be

estimated from the relationship among Young's modulus, Poisson's ratio, bulk modulus, and rigidity, as follows:

$$E_{comp.} = \frac{9K_{comp.}G_{comp.}}{3K_{comp.} + G_{comp.}} \quad \text{(Eq. 6-9)}$$

$$\nu_{comp.} = \frac{3K_{comp.} - 2G_{comp.}}{2\left(3K_{comp.} + G_{comp.}\right)}. \quad \text{(Eq. 6-10)}$$

Table 6-3 summarizes these estimated values of the CTE, Young's modulus, and Poisson's ratio for matrix (Z), dispersion (S), and nanocomposite (ZS).

Table 6-3 Characteristic values of Z, S and ZS.

Materials	CTE, α ($10^{-6}K^{-1}$)	Young's modulus, E (GPa)	Poisson's ratio, ν (-)
Z	10.60	200	0.270
S	4.45	440	0.190
ZS	(10.24)	(208)	(0.267)

( ) ; calculated value

The magnitude of residual stress ($\sigma_{cal.(L)}$) of the surface layer was calculated from both these estimated characteristic values and the thickness ratio (r_d: see Table 6-1) by Eq. 6-5. For bulky materials (i.e. N.Bulk and M.Bulk without multilayered geometric structure: r_d = 1), the theoretical residual stress of surface layer was obtained as 0 MPa, because this residual stress is produced by the multilayered geometric structure in this calculation. The calculated residual stress ($\sigma_{cal.(L)}$) is shown in Fig. 6-6 as a function of their thickness ratio (r_d). The $\sigma_{cal.(L)}$ of 2-dimensional dispersed nanocomposites was almost proportional to the r_d; compressive stress of 0 ~ -100 MPa for N, and tensile stress of 0 ~ +100 MPa for M.

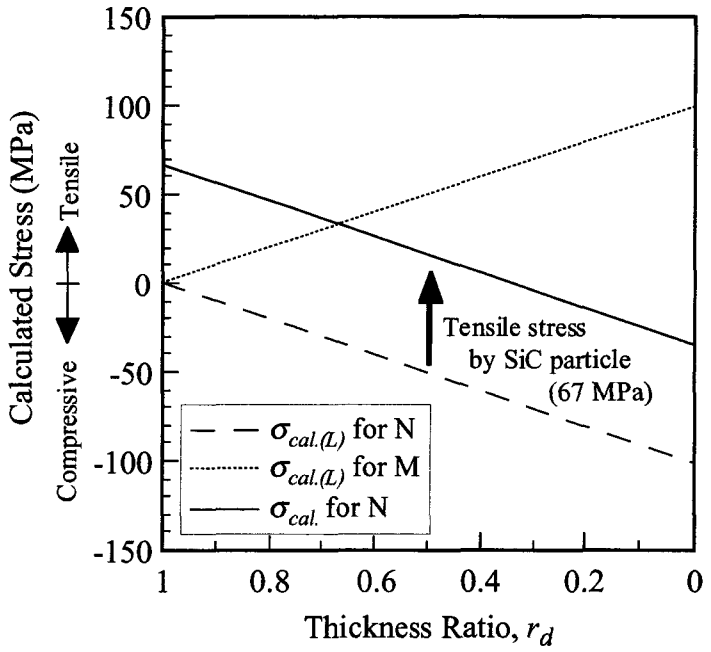

Fig. 6-6 Theoretically calculated residual stresses as a function of thickness ratio (r_d). Dash line and dotted line indicate the residual stress ($\sigma_{cal.(L)}$), which were estimated from layered geometry, for the surface layer for N and M, respectively. Solid line is total residual stress ($\sigma_{cal.}$: $\sigma_{cal.(L)}$ + $\sigma_{cal.(D),m}$) considering tensile stress induced by SiC particles for N.Surf.

(2) Residual Stress due to Particle Dispersion

In particle dispersed composite materials, which comprised matrix and dispersoid, residual stress also is produced by mismatch of their characteristic values as well as multilayered composites. ZS nanocomposite has tensile and compressive residual stress in the matrix (Z) with higher CTE and the dispersoid (S) with lower CTE. An average residual stress ($\sigma_{cal.(D)}$) induced by dispersion is calculated from the following equations [8].

$$\sigma_{cal.(D),m} = \frac{2x\beta E_m \cdot \Delta\alpha\Delta T}{(1-x)(\beta+2)(1+\nu_m)+3x\beta(1-\nu_m)} \quad \text{(Eq. 6-11)}$$

$$\sigma_{cal.(D),p} = \frac{-2(1-x)\beta E_m \cdot \Delta\alpha\Delta T}{(1-x)(\beta+2)(1+\nu_m)+3x\beta(1-\nu_m)} \quad \text{(Eq. 6-12)}$$

where $\sigma_{cal.(D),m}$ and $\sigma_{cal.(D),p}$ correspond to the average residual stress induced by dispersion for the matrix and the dispersoid, respectively. CTE mismatch ($\Delta\alpha$) was estimated from CTE values of Z and S (listed in Table 6-3), and temperature difference (ΔT) was same value with

that in Eq. 6-5 (i.e., ΔT = 1000°C). β is denoted as follows;

$$\beta = \frac{1+\nu_m}{1-2\nu_p} \cdot \frac{E_p}{E_m} \cdot \qquad \text{(Eq. 6-13)}$$

The average residual stresses ($\sigma_{cal.(D),m}$ and $\sigma_{cal.(D),p}$) in ZS nanocomposite (x = 0.05) were calculated from characteristic values listed in Table 6-3; 67 MPa for the matrix (Z) and -1275 MPa for the dispersoid (S) were obtained even though the SiC content was only 5 vol%. Therefore, it is inferred that the matrix (Z) of the ZS nanocomposite has significantly higher tensile residual stress.

(3) Total Residual Stress (Multilayer & Dispersion)

Because N.Surf. has both the layered structure and the dispersion in the surface layer, the residual stress of the surface layer should be calculated using both the effects above mentioned. Then, total residual stress ($\sigma_{cal.}$) for Z matrix of ZS layer was estimated from $\sigma_{cal.(L)}$ and $\sigma_{cal.(D),m}$, and is expressed in the follow,

$$\sigma_{cal.} = \sigma_{cal.(L)} + \sigma_{cal.(D),m} \qquad \text{(Eq. 6-14)}$$

The residual stress ($\sigma_{cal.}$) estimated by Eq. 6-14 for N.Surf. is shown in Fig. 6-6. The plots are shifted to the tensile side (upper side in the Fig. 6-6) due to the tensile stress induced by dispersion.

6-4-3. Stress Analysis

Measured surface stress ($\sigma_{mea.}$: in Fig. 6-5) showed similar tendency with theoretical calculated residual stress ($\sigma_{cal.}$: in Fig. 6-6), which was estimated from both multilayered geometric structure and dispersion. These stresses were increased with the decrease of the thickness ratio. However, these stresses disagreed in some parts such as the gradient of the plots and the value at the y-intercept. Then, an optimization of stress is carried out in the following.

(1) Machining Stress

The overall of measured surface stress ($\sigma_{mea.}$) was placed to the compressive side (i.e.,

downside in Fig. 6-5 and 6-6) rather than that of the calculated residual stress ($\sigma_{cal.}$). The difference at the y-intercept between the measured and calculated stress was approximately -30 and -70 MPa for M.Bulk and N.Bulk, respectively. Generally, machining process such as a grinding and a polishing brings compressive stress to the surface of materials [9,10]. It is thus appropriate that these differences were caused by machining stress. Suzuki [9] has reported that a compressive stress (-21 MPa) was observed on a lapped surface of 3Y-TZP. In this study, the similar compressive stress of approximately -30 MPa was observed on the surface of M. On the other hand, much higher compressive stress of approximately -70 MPa was on the polished surface of N. This compressive stress was also caused by the machining process, and it was considered that nano-sized SiC brought higher machining stress.

(2) Optimization of Measurement and Calculation

Microscopic distribution of residual stress within a layer is changed in the position; the magnitude is decreased with the increase of the distance from the layer boundary [11]. Therefore, it is evident that the magnitude of surface stress has the lowest value in the layer. This fact indicates that the magnitude of the surface stress is lower than that of the average residual stress within the layer. In other words, the magnitude of the measured surface stress ($\sigma_{mea.}$) is normally lower than that of the calculated residual stress ($\sigma_{cal.}$) of the surface layer. However, in the present work, the result was different with the expectation; the $\sigma_{mea.}$ indicated much higher value than the $\sigma_{cal.}$. To obtain the good agreement between measured and calculated stress, it is necessary to optimize two calculations; one is calculation on the theoretical residual stress (Eq. 6-5), and the other is on the measurement technique (Eq. 6-3).

For the stress measurement, in the present study, the stress constant (S) was calculated by Eq. 6-4, and regarded as approximately 330 MPa/degree. However, Suzuki [9] has reported that 294 MPa/degree as a stress constant of 3Y-TZP was obtained from their accurate measurement. Since the measured stress was obtained as a multiplication of the gradient (M) and the stress constant (S), the measured surface stresses ($\sigma_{mea.}$), which was calculated from the reported stress constant, indicated slightly lower value than that of 330 MPa/degree, and the gradient of the plot was also decreased.

Furthermore, in the calculation of residual stress of the surface layer (Eq. 6-5), it seems that $\Delta\alpha$ and ΔT are the most influential variables in the equation. In the calculation, $\Delta\alpha$ (i.e., the CTE mismatch between Z and ZS) was estimated as $0.36\times10^{-6}K^{-1}$ (see Table 6-3). From thermomechanical analysis (TMA: TMA-50, Shimadzu Co. Ltd., Japan) of $\Delta\alpha$ from room

temperature to 1000°C, the measured $\Delta\alpha$ was approximately $0.3\times10^{-6}K^{-1}$. However, the accurate difference between theoretical and measured $\Delta\alpha$ could not be estimated due to the poor significant figures of the TMA result. On the other hand, ΔT was regarded as 1000°C to calculate the theoretical residual stress ($\sigma_{cal.}$) in this study. When the ΔT is higher value than 1000°C, the theoretical residual stress is increased and the gradient of the plots in Fig. 6-6 is increased.

By these optimizations (i.e., the stress constant, ΔT and $\Delta\alpha$), it might be expected that the theoretically calculated residual stress well agrees with the measured surface stress.

6-5. Surface Reinforcement

6-5-1. Hardness

Mechanical properties on the surface of 2-dimensional dispersed nanocomposites were evaluated by Vickers indentation test.

Vickers hardness of 2-dimensional dispersed nanocomposites was measured by Vickers indenter (AVK-C2, Akashi Co., Ltd., Japan) on the top surface, where the surface stress was measured. The applied loads were 49, 98 and 196 N. The loads were applied for 15 seconds on the top surface of the composites at room temperature. Then, the diagonal length of residual pits *2a* are obtained from microscopic observation. The schematic drawing of the pit is illustrated in Fig. 6-7.

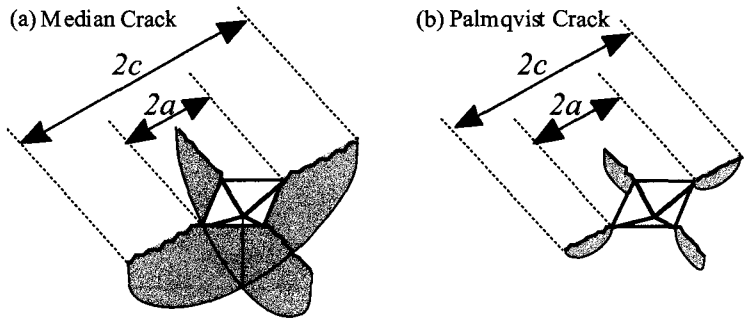

Fig. 6-7 Schematic drawing of the indentation and induced cracks in the case of (a) Median crack (c/a > 2.5) and (b) Palmqvist crak (c/a < 2.5).

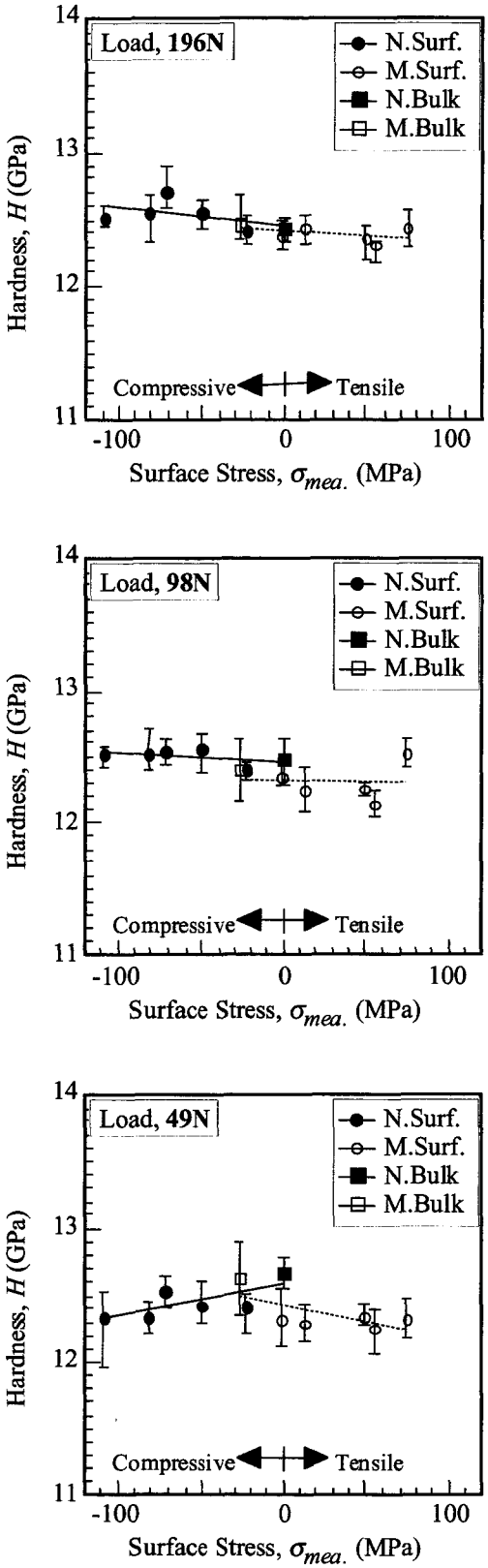

Fig. 6-8 Vickers hardness of 2-dimensional dispersed nanocomposites.

The Vickers hardness was calculated by following equation,

$$H_v = 1.8544 \times \frac{P}{(2a)^2} \quad \text{(Eq. 6-15)}$$

where P is the applied indentation load.

Measured Vickers hardness of the 2-dimensional dispersed nanocomposites is indicated in Fig. 6-8. Consequently, the Vickers hardness on the surface indicated almost same value as 12.5 GPa in the region from -100 MPa (compressive) to +80 MPa (tensile). When the indentation load was changed (49, 98 and 196 N), the Vickers hardness indicated same value. In this result, the effect of SiC dispersion was not observed, because the volume fraction was significantly low as 5 vol%.

6-5-2. IF Toughness

Fracture toughness was evaluated by Indentation Fracture (IF) method. In the IF method, fracture toughness was measured simultaneously with the hardness measurement by using Vickers hardness. After applying the indentation load for 15 seconds, the diagonal length of residual pits *2a* and the average length *c* of length of four cracks were observed (see Fig. 6-7). In this study, IF toughness was calculated by two kinds of equation known as Evans's equation (Eq. 6-16) [12,13] and Niihara's equation (Eq. 6-17) [14].

$$K_{IC(E)} = 0.026 \times \left(\frac{E}{H_v}\right)^{2/5} \left(\frac{P}{c^{3/2}}\right) \quad \text{(Eq. 6-16)}$$

$$K_{IC(N)} = 0.012 \times \left(\frac{E}{H_v}\right)^{2/5} \left(\frac{H_v P}{c-a}\right)^{1/2} \quad \text{(Eq. 6-17)}$$

where $K_{IC(E)}$ and $K_{IC(N)}$ indicate the IF toughness obtained from Evans's and Niihara's equations, respectively. E indicates Young's modulus of the Z or ZS, and 200 GPa was used in this calculation for both Z and ZS. Normally, Evans's equation is used for the indentation with median cracks, and Niihara's Equation is for the indentation with Palmqvist cracks. The schematic drawing of the shapes of the crack is shown in Fig. 6-7. It is known that the shape depends on the induced crack length. When c/a exceeds 2.3~2.5, the shape is considered as median crack. The shape is Palmqvist crack, when the c/a is less than 2.3~2.5.

Figure 6-9 indicates the crack length *c* as a function of the measured surface stress. The

crack length was increased as the applied load increased. Moreover, the length depended on the surface stress. Higher surface compressive stress decreased the crack length. The c/a was calculated for each sample from the crack length. Consequently, the calculated values of the c/a were distributed from approximately 2 to 3 (e.g., in 98 N, c/a = 1.99 and 2.97 for N.Surf.(5) and M.Surf.(5), respectively). Therefore, in this study, the IF toughness was estimated using both Evans's and Niihara's equations.

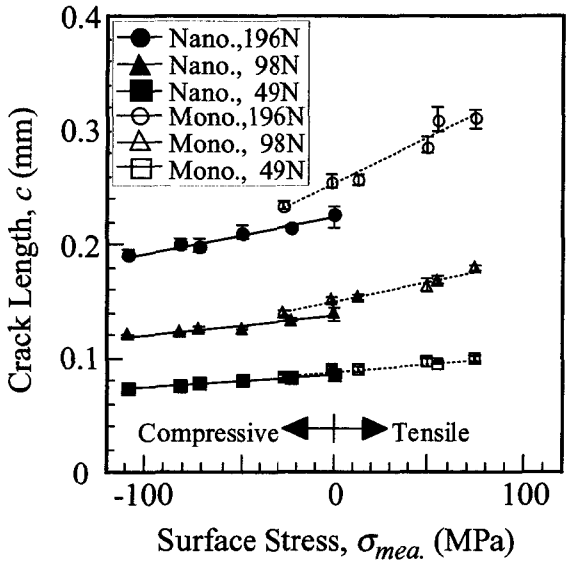

Fig. 6-9 Crack length *c* as a functionof the measured surface stress, $\sigma_{mea.}$

The IF toughness calculated from Evans's and Niihara's equations is indicated in Fig. 6-10 and 6-11, respectively. These plots indicate the calculated IF toughness K_{IC} as a function of the measured surface stress. In both plots, IF toughness strongly depend on the surface stress. However, the gradient obtained from Evans's equation was higher than that of Niihara's equation. Therefore, it is regarded that IF toughness obtained from Evans's equation is much sensitive to the surface stress. The effects of the SiC dispersoid and the applied load were observed in both plots. SiC dispersoid brings an increase to IF toughness. Especially, the SiC effect was apparent in higher applied load (196 N). In N.Surf., which has thin surface nanocomposites layers, the IF toughness ($K_{IC(E)}$ in 196 N, 5.8 MPa $m^{1/2}$) on the surface was increased by both surface compressive stress and nano-sized SiC dispersoid as compared with IF toughness ($K_{IC(E)}$ in 196 N, 4.4 MPa $m^{1/2}$) of monolithic Z bulk.

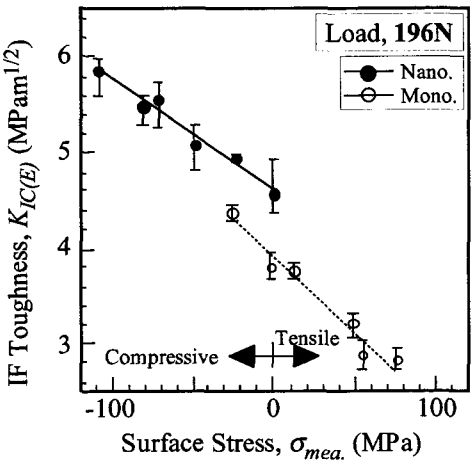

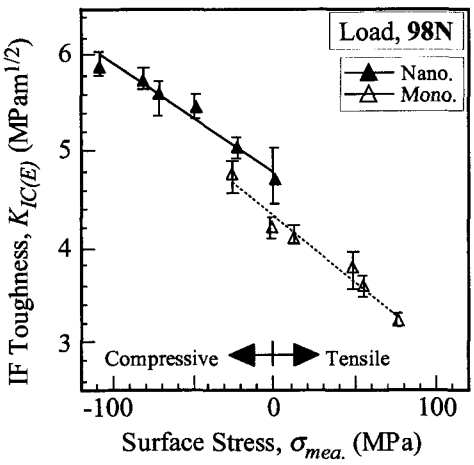

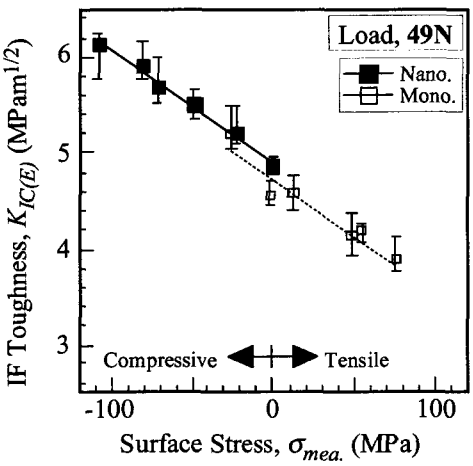

Fig. 6-10 IF toughness ($K_{IC(E)}$) calculated by Evans's equation as function of surface stress, $\sigma_{mea.}$.

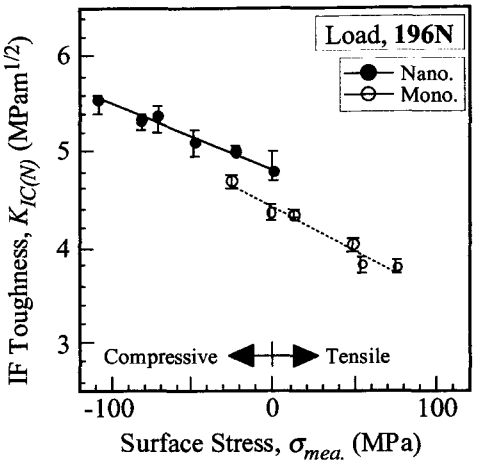

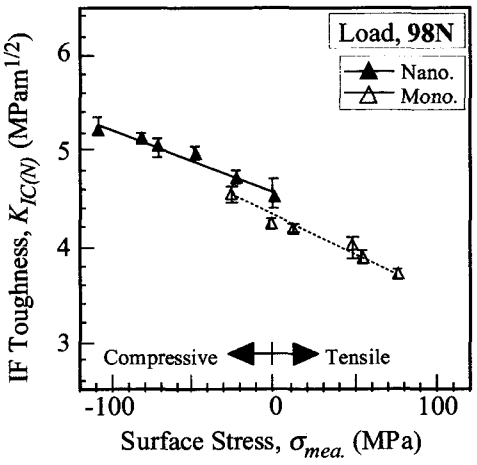

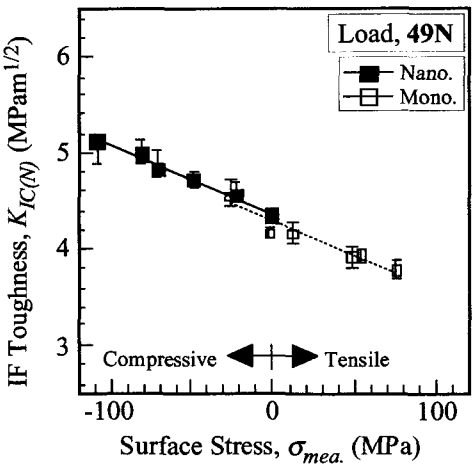

Fig. 6-11 IF toughness ($K_{IC(N)}$) calculated by Niihara's equation as function of surface stress, $\sigma_{mea.}$.

6-6. Thermal Properties

Thermal properties such as specific heat, thermal diffusivity and thermal conductivity were measured for N (i.e., N.Surf. and N.Bulk) and M.Bulk by laser flash method [15]. Thermal conductivity is obtained from the thermal diffusivity, specific heat and bulk density of the composites by

$$\kappa = \delta \times C \times \rho \qquad \text{(Eq. 6-18)}$$

where κ, δ, C, and ρ indicate thermal conductivity (W/Km), thermal diffusivity (mm^2/s), specific heat (J/gK), and the bulk density (g/cm^3), respectively.

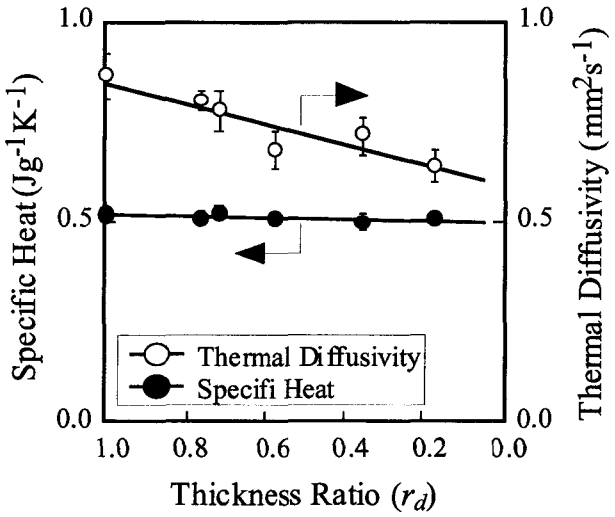

Fig. 6-12 Specific heat and thermal diffusivity of N.

In Fig. 6-12, the thermal diffusivity and the specific heat measured by laser flash method are shown as a function of the thickness ratio (r_d). In addition, the thermal conductivity calculated by Eq. 6-18 is shown in Fig. 6-13. The dotted line indicates a theoretical thermal conductivity obtained from rule of mixture for three-layered structure. The theoretical value was estimated by the following equation,

$$\kappa = d \times \left(\frac{2d_i}{\kappa_i} + \frac{d_s}{\kappa_s} \right)^{-1} = \frac{2\kappa_i \kappa_s}{4\kappa_s (1 - r_d) + \kappa_i r_d} \quad \text{(Eq. 6-19)}$$

where subscript *i* and *s* mean the inner and surface layer, and d, d_i, and d_s indicates the total thickness (in the present case, approximately 1 mm), thickness of inner layer, and thickness of surface layers (see Fig. 6-1(b)). In the equation, κ_i and κ_s indicate the thermal conductivity of bulky material (in the N.Surf., κ_i and κ_s indicate the thermal conductivity of Z and ZS, are approximately 2.6 and 2.4 $WK^{-1}m^{-1}$, respectively). Because SiC has much higher thermal conductivity (~46 $WK^{-1}m^{-1}$) as compared with 3Y-TZP (~3 $WK^{-1}m^{-1}$), the thermal conductivity of N.Bulk (2.6 $WK^{-1}m^{-1}$) showed higher value than that of M.Bulk (2.4 $WK^{-1}m^{-1}$). However, the thermal conductivity of N.Surf. with multilayered structure was much lower than the calculated value from rule of mixture (i.e., Eq. 6-19). The decrease was caused by the decrease of the thermal diffusivity, because the measured specific heat of each composite indicated almost same value, and the density of each composite was almost same value due to the small SiC content (see Table 6-2). Therefore, it was considered that the decrease of the thermal conductivity was caused by the decrease of the thermal diffusivity.

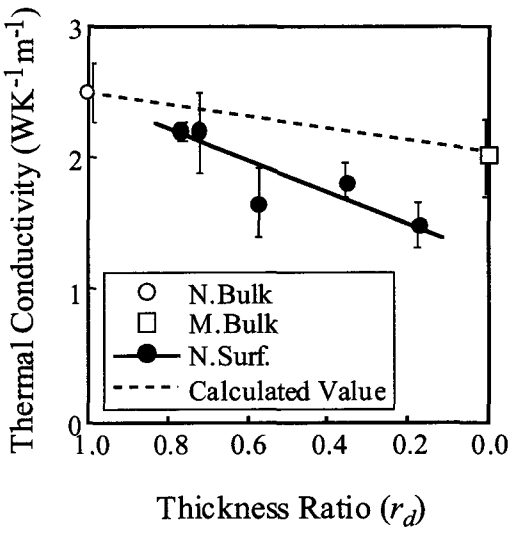

Fig. 6-13 Thermal conductivity of N.Surf., N.Bulk and M.Bulk. Dotted line indicates the theoretical thermal conductivity (calculated by Eq. 6-19) for multilayered structure.

Considering heat conduction, which is caused by diffusion of thermal vibration, crystal structure without strain (i.e., single crystal) has higher thermal conductivity. In 2-dimensional dispersed nanocomposites, directional residual stress was induced in the composites by the multilayered structure. Because the residual stress brings the strain of the crystal in the composites, it was believed that the thermal conductivity (i.e., thermal diffusivity) was inhibited by the strain. The mechanism is shown in Fig. 6-14. Therefore, 2-dimensional dispersed nanocomposites have lower thermal conductivity.

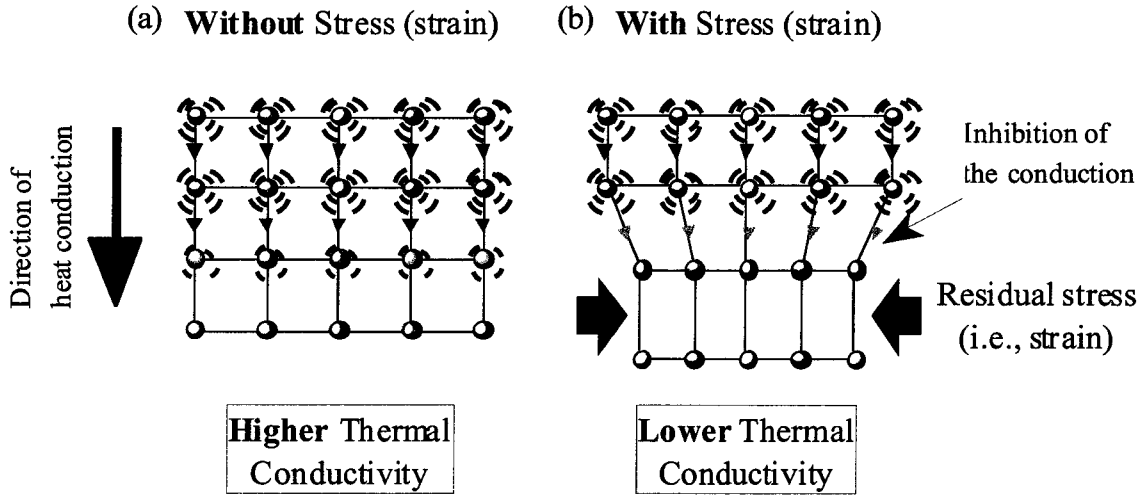

Fig. 6-14 Mechanism of inhibition of heat conduction by induced residual stress. (a) Crystal structure without stress has higher thermal conductivity. (b) Induced stress brings deformation of the crystal structure, and then heat conduction is decreased.

6-7. Summary

The 2-dimensional dispersed nanocomposites comprised of 3Y-TZP/SiC nanocomposite layer and 3Y-TZP monolithic layer were designed and fabricated by pressureless sintering in order to control the surface stress. Control of the layer thickness was achieved by stacking of greensheets prepared by doctor blade method in this study.

Microstructural observation and density of the fabricated materials revealed absence of defects such as debonding, channel crack and microcrack. Surface stress measured by XRD

analysis indicated similar tendency with theoretical residual stress, which was estimated from both multilayered geometric structure and dispersion, in surface layer. Surface nanocomposite, which was consisted of nanocomposite surface layer and monolithic inner layer, had compressive surface stress. On the other hand, tensile surface stress was observed in surface monolith (i.e., monolithic surface layers and nanocomposite inner layers). The magnitude of these surface stresses was increased with the increase of the thickness ratio. The magnitude of surface stress was 0 ~ -130 MPa for surface nanocomposite and -30 ~ 100 MPa for surface monolith, respectively.

In N.Surf. with thin surface nanocomposite layers, the indentation fracture (IF) toughness on the surface was significantly increased due to both surface compressive stress and nano-sized SiC dispersion.

Thermal properties of the 2-dimensional dispersed nanocomposites (i.e., N.Surf.) were measured by laser flash method. Consequently, the thermal conductivity of the composites with multilayered structure was significantly decreased as compared with the bulky materials (i.e., N.Bulk and M.Bulk). It was concluded that the decrease of the thermal conductivity was caused by the induced residual stress (i.e., strain of crystal) into the composites.

The design concept of 2-dimensional dispersed nanocomposite implies that local dispersed nanocomposite (e.g., N.Surf. and M.Surf. in this study) has an advantage for a realization of superior mechanical properties due to the synergetic effect combined both stress control and nano-sized dispersoid. In addition, it is expected that nano-sized dispersoid with quantum property provides local function to the composite, and a variation of dispersion controls the stress state within the composite. Especially, this concept is very much useful on ceramics coated materials, in which control of the stress state is required.

References

[1] T. Chartier, D. Merle, and J. L. Besson, *J. Eur. Ceram. Soc.*, **15**, 101 (1995).

[2] B. D. Cullity, Measurement of Residual Stress, ; pp. 447-78 in *Elements of X-ray Diffraction*, Edited by M. Cohen. Addison-Weslay Pub. Co., 1978.

[3] T. Goto, and S. Ohya, *J. Soc. Mat. Sci., Japan*, **47**, 1188 (1998).

[4] K. Tanaka, and Y. Akiniwa, *J. Soc. Mat. Sci., Japan*, **47**, 1301 (1998).

[5] N. Bamba, Y. H. Choa, T. Sekino, and K. Niihara, *J. Eur. Ceram. Soc.*, in press.

[6] E. H. Kerner, *Proc. Phys, Soc.*, **B69**, 808 (1956).

[7] Z. Hashin, and S. Shtrikman, *J. Mech. Phys. Solids*, **11**, 127 (1963).

[8] M. Taya, S. Hayashi, A. S. Kobayashi, and H. S. Yoon, *J. Am. Ceram. Soc.*, **73**, 1382 (1990).

[9] K. Suzuki, K. Tanaka, Y. Sakaida, and M. Kojima, *Trans. Jpn. Soc. Mech. Eng.*, Ser.A, **59**, 1353 (1993).

[10] D. Johnson-Walls, A. G. Evans, D. B. Marshall, and M. R. James, *J. Am. Ceram. Soc.*, **69**, 44 (1986).

[11] Nakahira and K. Niihara, in *Fracture Mechanics of Ceramics*, Vol. 9. Edited by R. C. Bradt *et al.* Plenum Press, pp. 165-78, New York, 1992.

[12] A.G. Evans, "Fracture Mechanics Applied to Brittle Materials", Edited by S.W. Freiman, ASTM STP 678, ASTM, Philadelphia (1979) p.112

[13] D.B. Marshall, and A.G. Evans, *J. Am. Ceram. Soc.*, **64**, C-182 (1981).

[14] K. Niihara, R. Morena, and D.P.H. Hasselman, *J. Mater. Sci. Lett.*, **1**, 13 (1982).

[15] JIS R 1611 : 1997

CHAPTER 7

Summary and Conclusions

In this research, hybrid composites, which combined multilayer and nano structure, were designed and fabricated to achieve the improvement of mechanical properties by directional residual stress and nano-sized dispersion. Multilayered nanocomposite was designed by introduction of concept of nanocomposite into traditional multilayered composite. On the other hand, 2-dimensional dispersed nanocomposite has novel structure, which is constructed by nanocomposite layer and monolithic layer. It was designed by introduction of multilayer structure into traditional nanocomposite. The mechanical properties of these hybrid composites were evaluated, and relationship between multilayer structure and nano structure was investigated.

In Chapter 2, the design concept of the two types of hybrid composites, in which multilayer and nano structure coexist, is proposed from the different strengthening mechanisms of multilayered composites and nanocomposites. One is the multilayered nanocomposites, in which nano-sized SiC particles are dispersed into Al_2O_3 and/or 3Y-TZP layer of Al_2O_3/3Y-TZP multilayered composite. It was expected that the macroscopic residual stress is controllable by SiC dispersion. The other hybrid composite is 2-dimensional dispersed nanocomposites, in which nano-sized SiC particles are dispersed in the surface or inside of 3Y-TZP matrix. By this 2-dimensional dispersion, the residual stresses can be introduced, and it must improve the mechanical properties of the composite.

In Chapter 3, Al_2O_3/3Y-TZP multilayered composite, multilayered nanocomposite and 2-dimensional dispersed nanocomposite were successfully fabricated by various combinations of greensheets prepared by doctor blade method. In addition, various evaluation methods such as mechanical properties, residual stress and thermal properties were described.

In Chapter 4, the optimization of layer thickness was carried out by evaluation of Al_2O_3/3Y-TZP multilayered composites with various thickness of Al_2O_3 and 3Y-TZP layers. In A1Z1 composite, any defects such debonding and channel crack was not observed from the optical microscopic observation. However, the other composites had channel cracks in 3Y-TZP layers, and debonding at layer boundaries. From the calculation of the macroscopic residual stress within each multilayered composite, the mechanism of defect formation was investigated and estimated the threshold values. Consequently, it was revealed that the channel crack was formed by two reasons. One was the macroscopic residual stress (i.e., average tensile stress) and the other was the microscopic stress distribution (i.e., the thickness of Z layer). Moreover, it was found that the stress difference between layers also caused the debonding.

In Chapter 5, nano-sized SiC dispersed Al_2O_3/3Y-TZP multilayered nanocomposites were evaluated in relation to the microstructure, the macroscopic residual stress, the microscopic stress distribution, and the mechanical properties. Microstructural observations indicated absence of a reaction phase and defects such as channel crack, delamination and debonding. Therefore, it was considered that residual stress relaxation by defects and reaction phase is negligible for obtained composites. Macroscopic residual stress was measured by XRD analysis on the cross sections. This measurement revealed that the macroscopic residual stress could be controlled by SiC dispersion. The increase of the magnitude of residual stress brought the increase of deflection angle and the decrease of the crack length. This fact implies that control of the residual stress is important on the crack propagation behavior. In addition, it was revealed that SiC dispersion strongly depressed crack propagation. In monolithic 3Y-TZP layer, the microscopic stress distribution had parabolic shape (i.e., stress concentration) in parallel and perpendicular directions. On the other hand, in the nanocomposite (i.e., SiC dispersed 3Y-TZP) layer, the stress distribution was different from monolithic layer. The result indicated that the microscopic distribution could be controlled by SiC dispersion.

In Chapter 6, 2-dimensional dispersed nanocomposites comprised of 3Y-TZP/SiC nanocomposite layer and 3Y-TZP monolithic layer were designed and fabricated in order to control the surface stress. Microstructural observation revealed absence of defects such as channel crack, debonding and microcrack. Surface stress measured by XRD analysis

indicated similar tendency with theoretical residual stress, which was estimated from both multilayered geometric structure and SiC dispersion, in surface layer. Surface nanocomposite, which was consisted of nanocomposite surface layer and monolithic inner layer, had compressive surface stress. On the other hand, tensile surface stress was observed in surface monolith (i.e., monolithic surface layers and nanocomposite inner layers). The magnitude of these surface stresses was increased with the increase of the thickness ratio. In the composite with high surface compressive stress, the indentation fracture (IF) toughness on the surface was significantly increased due to the surface compressive stress. In addition, nanocomposite surface layer brings the increase of IF toughness (i.e., nanocomposite effect). Thermal properties of the 2-dimensional dispersed nanocomposites were measured by laser flash method. Consequently, the thermal conductivity of the composites with multilayered structure was significantly decreased as compared with the bulky materials (i.e., traditional monolith and nanocomposite). It was concluded that the decrease of the thermal conductivity could be caused by the induced residual stress (i.e., strain of crystal) into the composites.

The designed hybrid composites, in which multilayered structure and nano structure coexist, indicated that the improvement of mechanical properties is achieved by both residual stress and nano-sized dispersion. This novel design concept of hybrid composites is believed to contribute to the improvement of mechanical properties for all ceramic materials. Furthermore, it is concluded that the introduction of directional residual stress gives a possibility to improve many properties, especially, of electronic ceramics as well as decrease of thermal conductivity. In addition, it is expected that nano-sized dispersoid with quantum property provides local function to the composite, and a variation of dispersion controls the stress state within the composite.

List of Publications

Papers

(1) T. Adachi, T. Sekino, T. Kusunose, T. Nakayama, A. Hikasa, Y.H. Choa, and K. Niihara
"Crack Propagation Behavior of Nano-sized SiC dispersed Multilayered Al_2O_3/3Y-TZP Hybrid Composites"
J. Ceram. Soc. Japan, (In press).

(2) T. Adachi, T. Sekino, T. Nakayama, and K. Niihara
"Measurement of Microscopic Stress Distribution of Multilayered Composite by X-ray Stress Analysis"
Materials Letters, (In press).

(3) T. Adachi, T. Sekino, Y. Hayashi, T. Nakayama, T. Kusunose, Y.H. Choa, and K. Niihara
"Residual Stress Control of Multilayered Al_2O_3/3Y-TZP Composites by Second Particulate"
J. American Ceram. Soc., (in contribution).

(4) T. Adachi, T. Sekino, Y. Yamamoto, T. Nakayama, and K. Niihara
"Design of 3Y-TZP/SiC Nanocomposite/3Y-TZP monolith Layered Composite,
Part I: Fabrication and Surface Stress Control"
(in preparation).

(5) T. Adachi, T. Sekino, Y.Yamamoto, T. Nakayama, and K. Niihara
"Design of 3Y-TZP/SiC Nanocomposite/3Y-TZP monolith Layered Composite,
Part II: Surface Reinforcement"
(in preparation).

Proceedings

(6) T. Adachi, Y.H. Choa, T. Sekino, and K. Niihara
"Crack Propagation Behaviorof Multilayered Al_2O_3/ZrO_2/SiC Hybrid Composites"
Proceedings of the 3rd Int. Nano Ceramic Forum (NCF3) and the 2nd Int. Symp. On Intermaterials (IMA'99), Jun. 9-12, 18-23(1999).

(7) T. Adachi, Y.H. Choa, T. Sekino, and K. Niihara
"Evaluation of Fracture Behavior of SiC Particle Reinforced Al_2O_3/3Y-TZP Multilayer Composites"
Proceedings of The 10th Iketani Conference on Materials Research toward The 21st Century, Jun. 26-30, 251-52(2000).

(8) T. Adachi, T. Sekino, and K. Niihara
"Residual Stress Controlling of Multilayered Composite by Second Phase Dispersion"
Proceedings of 6th Seminar on Core Univ. Prog. between Japan and Korea,- New Nanostructured and Nanocomposite Ceramics with Multiple Functionality, Jan. 13-15, 153-56(2002).

(9) T. Adachi, T. Sekino, and K. Niihara
"Mechanical Property Improvement by Residual Stress Controlling"
Proceedings of 3rd International Symposium on Eco-Materials Processing & Design, Jan. 27-29, 127-30(2002).

List of Supplementary Publications

Papers

(1) H. Kawaoka, T. Adachi, T. Sekino, Y.H. Choa, Lian Gao, and K. Niihara
"Effect of α/β phase ratio on microstructure and mechanical properties of silicon nitride ceramics"
J. Mater. Res., **16** [8], 2264-70(2001).

(2) T. Nakayama, M. Wada, T. Adachi, T. Sekino, K. Niihara, T. A. Yamamoto, and Y.H. Choa
"Formation and Magnetocaloric Effect of Superparamagnetic Nanocluster Composite"
Ceramic Transactions, **112** (*Proc. of the 7th Int. Conf. on Ceram. Processing Sci.*, May. 15-18(2000)), 761-66(2001).

(3) C.Y. Kim, T. Sekino, T. Adachi, Y. Yamamoto, and K. Niihara
"Microstructural observations of Cu_2O-added $BaTiO_3$ sintered under N_2 flow"
J. Ceram. Soc. Japan, **110** [7], 622-26(2002).

(4) E.H. Sun, Y.H. Choa, T. Sekino, T. Adachi, and K. Niihara
"Pressureless sintering and characterization of cordierite/ZrO_2 composites"
Materials Research Innovations, **6** [3], 105-11(2002).

(5) E. H. Sun, T. Kusunose, T. Sekino, T. Adachi, M. Wasa, and K. Niihara
"Preparation of Cordierite/ZrO_2 Nano-composite Powders by a Colloidal Coating Process"
J. Ceram. Soc. Japan, **110** [2], 92-97(2002).

(6) K. Niihara, T. Sekino, T. Kusunose, T. Nakayama, Y. Hayashi, T. Adachi, H. Kondo, and M. Wada
"21世紀の諸課題を克服するナノ及びナノコンポジット材料 (Nano and Nanocomposite Ceramic Materials for 21st Century)"
粉砕, **45号**, 47-58(2001).

(7) H. Kondo, T. Sekino, Y.H. Choa, T. Kusunose, T. Nakayama, M. Wada, T. Adachi, and K. Niihara
"Mechanical and Magnetic Properties of Nickel Dispersed Tetragonal Zirconia Nanocomposites"
Journal of Nanoscience and Nanotechnology, Vol.**2**, No.5, (2002). in press.

Proceeding

(8) T. Nakayama, T. Adachi, Y. Hayashi, Y. Yamamoto, T. Sekino, Y.H. Choa, T. Kusunose, T.A. Yamamoto, and K. Niihara
"Microstructure and Catalytic Properties of CeO_2/CuO Nanocluster Composites"
Proc. of 3rd International Symposium on Eco-Materials Processing & Design, Jan. 27-29, 30-33(2002).

Acknowledgments

The author would like to express his greatest appreciation and gratitude to Professor Koichi Niihara at The Institute of Scientific and Industrial Research (ISIR), Osaka University for his kind guidance, invaluable suggestions and encouragement in coordinating this investigation. The author would like to thank Professor Yasushi Kai and Professor Susumu Kuwabata at Department of Materials Chemistry for reviewing this thesis and their helpful advice.

Grateful thanks are given to Professor Tohru Sekino, Dr. Takafumi Kusunose, Dr. Tadachika Nakayama, Dr. Yamato Hayashi, Dr. Satoru Ueda, Dr. Atsuo Koreeda, Dr. Doh-Hyung Riu, Dr. Manuar Hussain, Dr. Masaaki Nagashima, Dr. Rajagopalan Ramaseshan, Dr. Wang Hao at Niihara Laboratory and Professor Yong-Ho Choa at The Graduate School of Industry and Business Administration, Hanyang University, Korea for their helpful discussion, guidance and encouragement throughout these works.

The author also thanks to Mr. Takanori Tanaka at Material Research Center of ISIR for his advice and help on the XRD analysis, Mr. Kimiaki Tanihata at Suganuma Laboratory for his advice and help on thermal analysis, Mr. Michiaki Kakuich, Mr. Masayoshi Onishi, Mr. Noriyuki Ogawa and Mr. Hiroaki Matsukawa at Manufacture Room of ISIR for their kind cooperation on manufacturing and repairing apparatuses, and Ms. Yasuko Furuta and Ms. Ikuko Hamaguchi at Library of ISIR for her help to collect a lot of reference papers.

The author gratefully acknowledge to Mr. Masahiko Tajika at Shiraishi Kogyo Kaisha, Ltd., for his attentive advice on the doctor blade method.

The author gratefully acknowledge to Dr. Hiroyuki Hayashi at Synergy Materials Research Center for his help on the thermal analysis and Mr. Hideki Hyuga at Fine Ceramics Research Association for his kindness on the wear test.

The author is grateful to Professor Nobuo Takusagawa and Professor Seiichi Taruta at Faculty of Engineering, Shinshu University for giving the opportunity to come Osaka University and their hearty encouragement.

Grateful acknowledgments are made to Mrs. Emiko Kitaura and Mrs. Rie Suehiro for their hearty encouragement and helpful assistance. The author thanks to the author's colleagues Mr. Yo Yamamoto and Mr. Hiroki Kondo and all other members of Niihara Laboratory for their kind discussion and encouragement.

Finally, author wishes to express the deep appreciation to the author's parents, brother and sister, Shirou Adachi, Matsumi Adachi, Takashi Adachi and Miyuki Adachi for their hearty encouragement and understandings.

December 2002

Tomohiko ADACHI